

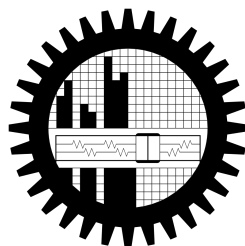
# **ELECTRONIC PROPERTIES AND TRANSISTOR APPLICATIONS OF MoS<sub>2</sub>/MX<sub>2</sub>/MoS<sub>2</sub> TRILAYER HETEROSTRUCTURES**

by

**Kanak Datta**

**Student Id: 1014062236 P**

A thesis submitted in partial fulfillment of the requirements for the degree of  
**Master of Science in Electrical and Electronic Engineering**



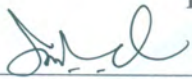
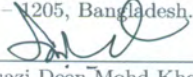


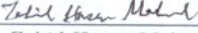
**Department of Electrical and Electronic Engineering  
BANGLADESH UNIVERSITY OF ENGINEERING AND  
TECHNOLOGY**

August, 2016

## Approval

The thesis titled “ELECTRONIC PROPERTIES AND TRANSISTOR APPLICATIONS OF  $\text{MoS}_2/\text{MX}_2/\text{MoS}_2$  TRILAYER HETEROSTRUCTURES” submitted by Kanak Datta, Student No: 1014062236 P, Session: October 2014, has been accepted as satisfactory in partial fulfillment of the requirements for the degree of Master of Science in Electrical and Electronic Engineering on August 20, 2016.


### Board of Examiners

-   
Dr. Quazi Deen Mohd Khosru  
Professor  
Department of Electrical and Electronic Engineering  
Bangladesh University of Engineering and Technology  
Dhaka - 1205, Bangladesh. Chairman  
(Supervisor)
-   
Dr. Quazi Deen Mohd Khosru  
Professor and Head  
Department of Electrical and Electronic Engineering  
Bangladesh University of Engineering and Technology  
Dhaka - 1205, Bangladesh. Member  
(Ex-officio)
-   
Dr. Mohammad Jahangir Alam  
Professor  
Department of Electrical and Electronic Engineering  
Bangladesh University of Engineering and Technology  
Dhaka - 1205, Bangladesh. Member
-   
Dr. Samia Subrina  
Associate Professor  
Department of Electrical and Electronic Engineering  
Bangladesh University of Engineering and Technology  
Dhaka - 1205, Bangladesh. Member
-   
Dr. Zahid Hasan Mahmood  
Professor  
Department of Electrical and Electronic Engineering  
University of Dhaka  
Dhaka - 1000, Bangladesh. Member  
(External)

# Declaration of Authorship

It is hereby declared that this thesis or any part of it has not been submitted elsewhere for the award of any degree or diploma.

Signature of the Candidate:



---

(Kanak Datta)

*“There should be no boundaries to human endeavor.  
We are all different. However bad life may seem, there is always  
something you can do, and succeed at.  
While there’s life, there is hope.”*

- Stephen William Hawking

## *Acknowledgements*

At first, I would like to thank the Department of Electrical and Electronic Engineering, Bangladesh University of Engineering and Technology for providing me with the opportunity and facilities to carry out the simulation work.

I would like to express my sincere gratitude to my supervisor Dr. Quazi Deen Mohd Khosru, Professor, and Head, Department of Electrical and Electronic Engineering, Bangladesh University of Engineering and Technology (BUET), for his continuous support throughout the course of my MSc study and research. I feel immensely grateful to him for his motivation, enthusiasm, persistence, patience, generosity and above all, belief in my abilities which made this work possible.

Besides my supervisor, I would also like to express my gratitude to the members of the board of examiners: Prof. Mohammad Jahangir Alam, Prof. Samia Subrina, and Prof. Zahid Hasan Mahmood for taking the time to evaluate my work and provide insightful suggestions and inspiration for future development.

My sincere thanks also goes to Saeed-Uz-Zaman Khan, Lecturer, Department of Electrical and Electronic Engineering (EEE), Bangladesh University of Engineering and Technology (BUET), for his suggestion and discussion regarding TMDC materials.

Last but not the least, I would like to thank my family, my friends and colleagues for their sincere support, inspiration and help in every possible way throughout the long journey of my life as an academic researcher.

# *Abstract*

In recent years, a lot of scientific research effort has been put forth for the investigation of Transition Metal Dichalcogenides (TMDC) and other Two Dimensional (2D) materials like Graphene, Boron Nitride. Theoretical investigation on the physical aspects of these materials has revealed a whole new range of exciting applications due to wide tunability in electronic and optoelectronic properties. Transition Metal Dichalcogenides (TMDC) and their bi-layer/tri-layer heterostructures have become the focus of intense research and investigation in recent time due to their promising electronic and optoelectronic applications. In this work, we have presented a first principle simulation study on the electronic properties of  $\text{MoS}_2/\text{MX}_2/\text{MoS}_2$  ( $\text{M}=\text{Mo}$  or  $\text{W}$ ;  $\text{X}=\text{S}$  or  $\text{Se}$ ) trilayer heterostructure. We have investigated the effect of stacking configuration, bi-axial compressive and tensile strain on the electronic properties of the trilayer heterostructures. In our study, it is found that, under relaxed condition all the trilayer heterostructures at different stacking configurations show semiconducting nature. The nature of the bandgap, however, depends on the inserted TMDC monolayer between the top and bottom  $\text{MoS}_2$  layers and their stacking configurations. Like bilayer heterostructures, trilayer structures also show semiconducting to metal transition under the application of tensile strain. With increased tensile strain, the conduction band minima shifts to K point in the Brillouin zone which leads to a lowering of electron effective mass at conduction band minima. The study on the projected density of states reveal that, the conduction band minima is mostly contributed by the  $\text{MoS}_2$  layers and states at the valance band maxima are contributed by the middle TMDC monolayer. In our study, the highest bandgap was found for  $\text{MoS}_2/\text{WS}_2/\text{MoS}_2$  trilayer while the lowest bandgap was found for the  $\text{MoS}_2/\text{WSe}_2/\text{MoS}_2$  trilayer. Besides exploring the electronic properties, we have explored device level performance of trilayer TMDC heterostructure ( $\text{MoS}_2/\text{MX}_2/\text{MoS}_2$ ;  $\text{M}=\text{Mo}$  or,  $\text{W}$  and  $\text{X}=\text{S}$  or,  $\text{Se}$ ) MOSFETs in the quantum ballistic regime. Our simulation shows that device ‘on’ current can be improved by inserting a  $\text{WS}_2$  monolayer between two  $\text{MoS}_2$  monolayers. Application of biaxial tensile strain reveals a reduction in drain current which can be attributed to the lowering of carrier effective mass with increased tensile strain. Due to low bandgap  $\text{MoS}_2/\text{WSe}_2/\text{MoS}_2$  trilayer heterostructure MOSFETs were found to be showing high off-state leakage and thereby high sub-threshold swing. In addition, it is found that gate underlap geometry improves electrostatic device performance by improving sub-threshold swing. However, increase in channel resistance reduces drain current.

# Contents

<b>Approval</b>	<b>i</b>
<b>Declaration of Authorship</b>	<b>ii</b>
<b>Acknowledgements</b>	<b>iv</b>
<b>Abstract</b>	<b>v</b>
<b>List of Figures</b>	<b>viii</b>
<b>List of Tables</b>	<b>x</b>
<b>Abbreviations</b>	<b>xi</b>
<b>Physical Constants</b>	<b>xii</b>
<b>1 Introduction</b>	<b>1</b>
1.1 Current State and Challenges in CMOS Technology . . . . .	1
1.2 Why TMDC . . . . .	6
1.3 Thesis Objectives . . . . .	10
1.4 Organization of the Thesis . . . . .	10
<b>2 Exploration of MoS<sub>2</sub>: It's Physics and Devices</b>	<b>12</b>
2.1 MoS <sub>2</sub> : Crystal Structure . . . . .	12
2.2 Electronic Properties of MoS <sub>2</sub> . . . . .	13
2.3 Tunable Electronic Properties of MoS <sub>2</sub> . . . . .	15
2.4 MoS <sub>2</sub> : Multilayer Structures . . . . .	17
2.5 MoS <sub>2</sub> : Monolayer and Multilayer Devices . . . . .	19
2.6 The MX <sub>2</sub> Monolayer . . . . .	22
<b>3 Simulation Methods</b>	<b>24</b>
3.1 Density Functional Theory: A Brief Overview . . . . .	24
3.1.1 What We Seek . . . . .	24
3.1.2 The Born-Oppenheimer Approximation . . . . .	25
3.1.3 The Hohenberg-Khon Theorem . . . . .	26

3.1.4	The Kohn-Sham Equations . . . . .	27
3.1.5	Exchange and Correlation Functional . . . . .	29
3.1.6	Local Density Approximation . . . . .	30
3.1.7	Generalized Gradient Approximation . . . . .	30
3.1.8	The Pseudopotential Approximation . . . . .	31
3.2	Computational Details of Electronic Structure Calculation . . . . .	32
3.2.1	MoS <sub>2</sub> /MX <sub>2</sub> /MoS <sub>2</sub> Trilayer System Under Study . . . . .	32
3.2.2	Simulation Process Using Quantum Espresso . . . . .	33
3.3	Ballistic Simulation of Double Gate MOSFET . . . . .	34
3.3.1	Device Description . . . . .	34
3.3.2	Transport Simulation Using Fast Uncoupled Mode Space Approach . . . . .	34
<b>4</b>	<b>Results and Discussion</b>	<b>38</b>
4.1	Lattice Structure of Trilayer MoS <sub>2</sub> Heterostructure . . . . .	38
4.2	Electronic Properties of the Trilayer . . . . .	40
4.2.1	Bandstructure and Density of States of the Relaxed Trilayer Heterostructure . . . . .	40
4.2.2	Electronic Properties of Strained Trilayer Heterostructure . . . . .	45
4.2.3	Effect of Strain on Projected Density of States . . . . .	50
4.2.4	Effect of Bi-axial Strain on Effective Mass and Bandgap . . . . .	53
4.3	MOSFET Application of Trilayer TMDC Heterostructures . . . . .	58
4.3.1	Ballistic Simulation of MoS <sub>2</sub> /MoSe <sub>2</sub> /MoS <sub>2</sub> MOSFET . . . . .	59
4.3.2	Ballistic Simulation of the Double Gate Device with Different TMDC Trilayers as Channel Material . . . . .	61
4.3.3	Ballistic Simulation of Strained Trilayer TMDC Double Gate MOSFET . . . . .	67
4.3.4	Ballistic Simulation of the Double Gate MOSFET Using Gate Underlap Geometry . . . . .	68
<b>5</b>	<b>Conclusion</b>	<b>72</b>
5.1	Summary . . . . .	72
5.2	Suggestion for Future Work . . . . .	73
	<b>Bibliography</b>	<b>74</b>



# List of Figures

1.1	Trends in the number of transistors per chip . . . . .	3
1.2	Intel's innovation enabled technology pipeline . . . . .	3
1.3	Process flow diagram infographic of INTEL . . . . .	4
1.4	Planar and non-planar MOSFETs . . . . .	4
1.5	Switching delay vs energy . . . . .	5
1.6	Computational throughput vs power density for some of the beyond-CMOS device technologies . . . . .	6
1.7	Unit cell of MoS <sub>2</sub> . . . . .	7
1.8	Bandstructure of MoS <sub>2</sub> . . . . .	8
1.9	MoS <sub>2</sub> transistor application . . . . .	9
2.1	MoS <sub>2</sub> phases and stacking configurations . . . . .	12
2.2	Bandstructure of MoS <sub>2</sub> : bulk and monolayer . . . . .	14
2.3	Variation of conduction and valance band energies in MoS <sub>2</sub> . . . . .	14
2.4	Conduction and valance band topology in MoS <sub>2</sub> . . . . .	15
2.5	Bandgap variation of MoS <sub>2</sub> under strain . . . . .	18
2.6	Bandstructure of MoS <sub>2</sub> under electric field . . . . .	18
2.7	Bandstructure of MoS <sub>2</sub> bilayer heterostructures . . . . .	19
2.8	Bandgap of bilayer TMDC heterostructures under strain and electric field . . . . .	20
2.9	Bandstructure of monolayer MoSe <sub>2</sub> , WS <sub>2</sub> and WSe <sub>2</sub> . . . . .	23
3.1	Electron effective mass of TMDC trilayers at K point . . . . .	33
3.2	10 nm double gate MOSFET used in this work . . . . .	35
4.1	Bandstructure of relaxed MoS <sub>2</sub> /MoSe <sub>2</sub> /MoS <sub>2</sub> . . . . .	42
4.2	Bandstructure of relaxed MoS <sub>2</sub> /WS <sub>2</sub> /MoS <sub>2</sub> . . . . .	43
4.3	Bandstructure of relaxed MoS <sub>2</sub> /WSe <sub>2</sub> /MoS <sub>2</sub> . . . . .	44
4.4	Bandstructure and PDOS of relaxed MoS <sub>2</sub> /MoSe <sub>2</sub> /MoS <sub>2</sub> at AAA stacking . . . . .	45
4.5	Bandstructure and PDOS of relaxed MoS <sub>2</sub> /MoSe <sub>2</sub> /MoS <sub>2</sub> at ABA stacking . . . . .	46
4.6	Bandstructure and PDOS of relaxed MoS <sub>2</sub> /MoSe <sub>2</sub> /MoS <sub>2</sub> at ACA stacking . . . . .	46
4.7	Bandstructure and PDOS of relaxed MoS <sub>2</sub> /WS <sub>2</sub> /MoS <sub>2</sub> at AAA stacking . . . . .	46
4.8	Bandstructure and PDOS of relaxed MoS <sub>2</sub> /WS <sub>2</sub> /MoS <sub>2</sub> at ABA stacking . . . . .	47
4.9	Bandstructure and PDOS of relaxed MoS <sub>2</sub> /WS <sub>2</sub> /MoS <sub>2</sub> at ACA stacking . . . . .	47
4.10	Bandstructure and PDOS of relaxed MoS <sub>2</sub> /WSe <sub>2</sub> /MoS <sub>2</sub> at AAA stacking . . . . .	47
4.11	Bandstructure and PDOS of relaxed MoS <sub>2</sub> /WSe <sub>2</sub> /MoS <sub>2</sub> at ABA stacking . . . . .	48
4.12	Bandstructure and PDOS of relaxed MoS <sub>2</sub> /WSe <sub>2</sub> /MoS <sub>2</sub> at ACA stacking . . . . .	48
4.13	Bandstructure of MoS <sub>2</sub> /MoSe <sub>2</sub> /MoS <sub>2</sub> under strain at AAA stacking . . . . .	50
4.14	Bandstructure of MoS <sub>2</sub> /MoSe <sub>2</sub> /MoS <sub>2</sub> under strain at ABA stacking . . . . .	50

4.15	Bandstructure of MoS <sub>2</sub> /MoSe <sub>2</sub> /MoS <sub>2</sub> under strain at ACA stacking . . . .	51
4.16	Bandstructure of MoS <sub>2</sub> /WS <sub>2</sub> /MoS <sub>2</sub> under strain at AAA stacking . . . .	51
4.17	Bandstructure of MoS <sub>2</sub> /WS <sub>2</sub> /MoS <sub>2</sub> under strain at ABA stacking . . . .	52
4.18	Bandstructure of MoS <sub>2</sub> /WS <sub>2</sub> /MoS <sub>2</sub> under strain at ACA stacking . . . .	52
4.19	Bandstructure of MoS <sub>2</sub> /WSe <sub>2</sub> /MoS <sub>2</sub> under strain at AAA stacking . . . .	53
4.20	Bandstructure of MoS <sub>2</sub> /WSe <sub>2</sub> /MoS <sub>2</sub> under strain at ABA stacking . . . .	53
4.21	Bandstructure of MoS <sub>2</sub> /WSe <sub>2</sub> /MoS <sub>2</sub> under strain at ACA stacking . . . .	54
4.22	Bandstructure and PDOS of MoS <sub>2</sub> /MoSe <sub>2</sub> /MoS <sub>2</sub> at AAA stacking under compressive strain . . . . .	54
4.23	Bandstructure and PDOS of MoS <sub>2</sub> /MoSe <sub>2</sub> /MoS <sub>2</sub> at AAA stacking under tensile strain . . . . .	55
4.24	Bandstructure and PDOS of MoS <sub>2</sub> /WS <sub>2</sub> /MoS <sub>2</sub> at AAA stacking under compressive strain . . . . .	55
4.25	Bandstructure and PDOS of MoS <sub>2</sub> /WS <sub>2</sub> /MoS <sub>2</sub> at AAA stacking under tensile strain . . . . .	56
4.26	Bandstructure and PDOS of MoS <sub>2</sub> /WSe <sub>2</sub> /MoS <sub>2</sub> at AAA stacking under compressive strain . . . . .	56
4.27	Bandstructure and PDOS of MoS <sub>2</sub> /WSe <sub>2</sub> /MoS <sub>2</sub> at AAA stacking under tensile strain . . . . .	57
4.28	Bandgap of TMDC trilayers . . . . .	57
4.29	Electron effective mass of TMDC trilayers at K point . . . . .	58
4.30	Electron effective mass of TMDC trilayers at $\Delta$ point . . . . .	58
4.31	Subband energy under gate and drain voltage . . . . .	60
4.32	Energy resolved current density and LDOS . . . . .	62
4.33	Transmission co-efficient and drain current . . . . .	63
4.34	Ballistic Id-Vg characteristics . . . . .	64
4.35	Subband energy and 2D carrier density in the channel for different trilayers	65
4.36	Gate capacitance and Id-Vg comparison of the trilayers . . . . .	66
4.37	Subband energy under bi-axial strain . . . . .	68
4.38	Effect of bi-axial strain on MOSFET performance of different trilayers . .	69
4.39	Id-Vg characteristics of different trilayer MOSFETs at different underlap lengths . . . . .	70
4.40	'On' current and SS variation of different trilayer MOSFETs at different underlap lengths . . . . .	71

# List of Tables

2.1	MoS <sub>2</sub> Unit Cell Parameters . . . . .	13
4.1	Optimized Lattice Parameters-MoS <sub>2</sub> /MoSe <sub>2</sub> /MoS <sub>2</sub> . . . . .	39
4.2	Optimized Lattice Parameters-MoS <sub>2</sub> /WS <sub>2</sub> /MoS <sub>2</sub> . . . . .	39
4.3	Optimized Lattice Parameters-MoS <sub>2</sub> /WSe <sub>2</sub> /MoS <sub>2</sub> . . . . .	40
4.4	Energy Separation Between Symmetry Points in the Brillouin Zone . . . . .	41
4.5	Extracted Values of Effective Mass at Conduction Band Minima, Bandgap, Dielectric Constant from First Principle Simulation . . . . .	59
4.6	Comparison of SS and DIBL for MOSFETs Using Different Trilayer TMDC as Channel Materials . . . . .	64

# Abbreviations

<b>2D</b>	<b>Two Dimensional</b>
<b>3D</b>	<b>Three Dimensional</b>
<b>eV</b>	<b>electron Volt</b>
<b>vdW</b>	<b>van der Waals</b>
<b>CMOS</b>	<b>Complementary Metal Oxide Semiconductor</b>
<b>CVD</b>	<b>Chemical Vapor Deposition</b>
<b>DFT</b>	<b>Density Functional Theory</b>
<b>DIBL</b>	<b>Drain Induced Barrier Lowering</b>
<b>FET</b>	<b>Field Effect Transistor</b>
<b>FUMS</b>	<b>Fast Uncoupled Mode Space</b>
<b>GGA</b>	<b>Generalized Gradient Approximation</b>
<b>HRTEM</b>	<b>High Resolution Transmission Electron Microscopy</b>
<b>ITRS</b>	<b>International Technology Roadmap for Semiconductors</b>
<b>LDA</b>	<b>Local Density Approximation</b>
<b>LDOS</b>	<b>Local Density Of States</b>
<b>NEGF</b>	<b>Non Equilibrium Green's Function</b>
<b>PDOS</b>	<b>Projected Density Of States</b>
<b>SCE</b>	<b>Short Channel Effect</b>
<b>SOI</b>	<b>Silicon On Insulator</b>
<b>SRAM</b>	<b>Static Random Access Memory</b>
<b>SS</b>	<b>Sub-threshold Swing</b>
<b>TFET</b>	<b>Tunneling Field Effect Transistor</b>
<b>TMDC</b>	<b>Transition Metal Dichalcogenides</b>
<b>UTB</b>	<b>Ultra Thin Body</b>
<b>VASP</b>	<b>Vienna Ab-initio Simulation Package</b>

# Physical Constants

Speed of Light	$c$	$=$	$2.997\,924\,58 \times 10^8 \text{ ms}^{-2}$	(exact)
Elementary charge	$q$	$=$	$1.60217662 \times 10^{19}$	coulomb
Electron mass	$m_0$	$=$	$9.10938356 \times 10^{-31}$	kg
Permittivity of free space	$\varepsilon_0$	$=$	$8.85418782 \times 10^{-12}$	$\text{Fm}^{-1}$
Planck constant	$h$	$=$	$6.62606876 \times 10^{-34}$	J s
Boltzmann constant	$k$	$=$	$1.3806503 \times 10^{-23}$	$\text{JK}^{-1}$
Angstrom	$\text{\AA}$	$=$	$1.0 \times 10^{-10}$	m

*To My Beloved Teachers*

# Chapter 1

## Introduction

### 1.1 Current State and Challenges in CMOS Technology

Moore's Law, originally an attempt to project the future trend of integrated circuit development back in 1965, has successfully powered the revolution of the semiconductor industry for nearly 4 decades. The law basically describes a trend of exponential improvement that has led to the innovation of super-fast sophisticated computers with exceptionally enhanced capabilities, high-speed internet, smart devices, high tech gadgets, smart sensors that crowd our everyday life. In an attempt to project the future of integrated circuits, Gordon Moore, who was then the research director of Fairchild Semiconductor in San Jose, California, estimated that the number of transistors, the 'on'/'off' switches that are the main components of processors, and other components in an integrated circuit would double every year [1]. A more realistic revision followed 10 years later in 1975 when the doubling time interval was estimated to be about two years or so [2]. This projection shaped the growth of semiconductor industry for nearly four decades. In order to keep in touch with the promise of improvement that Gordon Moore prophesied, it was required to scale down transistor dimension so that more and more of these devices could be packaged on the same chip which, in turn, required major astounding leaps in photolithography process technology and fabrication facilities.

After three decades, this growing trend hit its first stumbling block along the road. The main reason was heat generated in transistors. As feature size shrunk below 90 nm, the chips began to get hotter which was in contrary to the trend that had been observed before. The scaling of feature size basically means scaling the physical dimension of the transistors. A basic transistor incorporates four terminals- gate, drain, source and body. The gate terminal exerts electrostatic force over the channel and controls the electron transport between source and drain. With ever shrinking transistor size, it was becoming

increasingly difficult to maintain same electrostatic control of the gate terminal over the channel. As a result, the transistors could not be properly switched ‘off’ and current would leak through portions of the channel where the gate control became weaker and through the underlying substrate. This ‘off’ state leakage was a matter of real concern when it came to the heating issue in large scale integrated circuits. Another source of leakage was the tunneling of electrons from the channel through insulating dielectric material that separated channel from the metal gate. Shrinking feature size meant shrinking thickness of this dielectric material as well which was down to 1.2 nm i.e. only five atomic layers thick when 90 nm process technology was introduced [3]. In a bid to encounter this issue, high-K dielectrics were introduced along with metal gate electrodes which allowed scaling of gate dielectric to continue for a few more future technology nodes [4]. Going further down the road, to boost the electrostatic effect of the gate and reduce leakage, two transistor technologies were introduced- UTB SOI, also known as fully depleted SOI and non-planar or 3D device structures like FinFETs [5]. UTB SOI technology basically means building a thin silicon channel on an insulating oxide layer, generally SiO<sub>2</sub> and thereby replacing the bulk silicon. On the other hand, 3D architectures like FinFETs require creating non-planar fin like channels which would be surrounded by the gate on three sides. Of these two technologies, the 3D architecture was commercially implemented in 22 nm node. Auth et al. [6] demonstrated a 22 nm non-planar CMOS transistors using strained Si which was followed by the demonstration of 14 nm non-planar technology in [7]. As projected by ITRS [8], by 2020, the transistor gate length would approach sub-10 nm regime which could severely degrade their performance as Short Channel Effects (SCEs) would become more and more prominent and device operations will be largely governed by quantum uncertainties [9]. With the diameter of a silicon atom being 0.26 nm, shrinking down channel length in sub-10 nm regime means, there would be roughly 40 atoms in the channel.

In order to address the issues related to heating occurred in the chips, modifications were also brought in processor architectures. It was observed that increment in the number of processing units and consequent reduction in clock speed could lead to more efficient performance of the overall system and lower heat output compared to a single processing unit [10]. Therefore, although the maximum speed of the processors was clipped to encounter heating issues, a newer trend in the design of internal circuits- implementing multicore architecture allowed the industry to keep in touch with the performance curve of Moore’s Law.

For the past two decades, major challenges and sophisticated technologies in semiconductor industry were projected by International Technology Roadmap for Semiconductors (ITRS). These projections were done keeping a strong focus on the path set by Moore’s law. However, with the amazing development in integrated electronics over time and



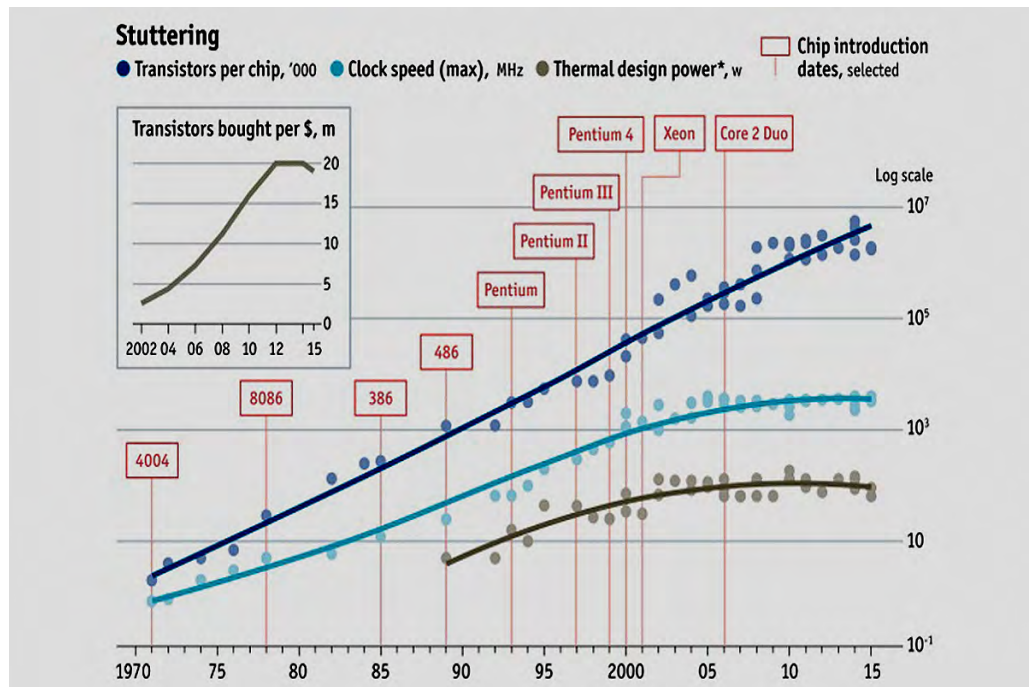


Figure 1.1: Trends in the number of transistors per chip along with the clock speed in MHz for past few decades. The clock speed started to level off just after 2004. However, the number of transistors per chip kept on increasing. At the same time, processor design was modified to keep pace with Moore’s law. The inset figure shows the number of transistors bought per \$ since 2002 which shows a decreasing trend in recent time [11]

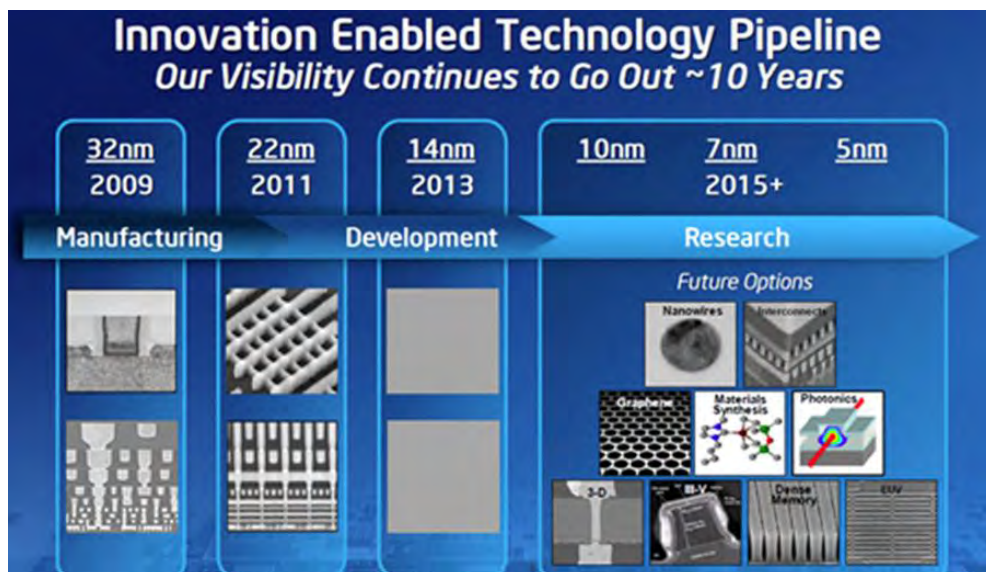


Figure 1.2: Intel’s innovation enabled technology pipeline [12]

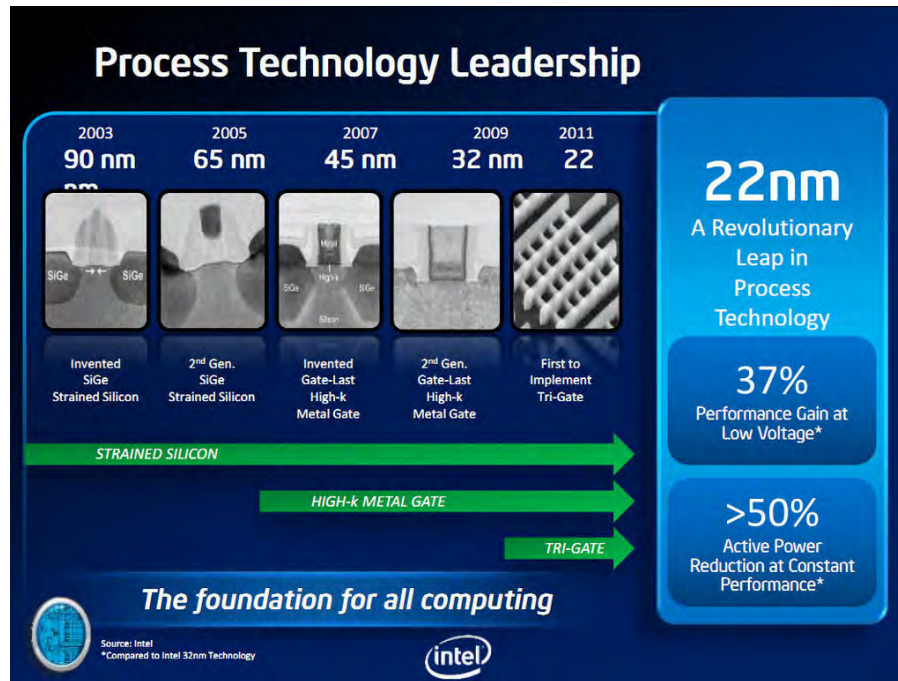


Figure 1.3: Process flow diagram infographic of last few technology nodes starting from 90 nm. High-k dielectric and metal gate were first implemented in 2007 at 45 nm. 22 nm non-planar FinFET was introduced in 2011. More recent progress includes the introduction of 14 nm FinFETs in 2014 (not shown in this figure) [12]

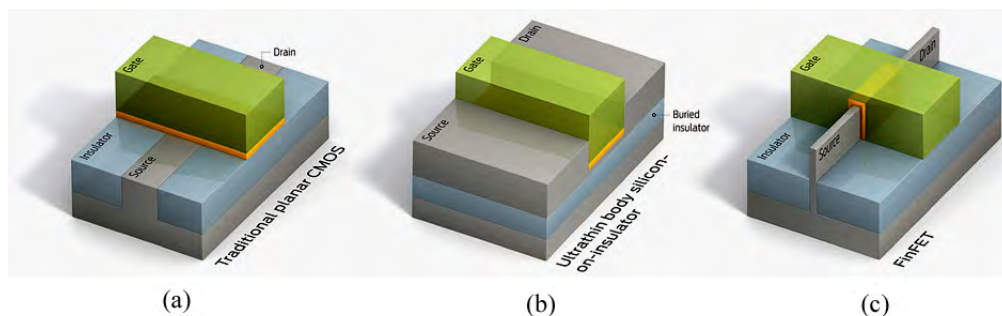


Figure 1.4: (a) Conventional bulk planar CMOS device; (b) Ultrathin body silicon-on-insulator (UTBSOI) device; (c) 3D transistor architecture like FinFET [13]

exciting applications consistently shaping the requirements of these modern technological marvels, soon it was realized that only strong focus on Moore's law would not be enough to capture the whole projection of the semiconductor industry in years to come. This realization led to the reformation of the roadmap which was declared as ITRS 2.0 [15]. The newly formed roadmap was designed to consist of seven building blocks. One of these building blocks was to seek newer device technologies that would fulfill the requirement of next generation digital logic circuits. These beyond-CMOS device technologies would incorporate newer device physics and operating principle to meet the requirement of next generation microprocessors. These beyond-CMOS transistor technologies include Spintronic devices (SpinFET), Negative Capacitance FETs (NCFET),

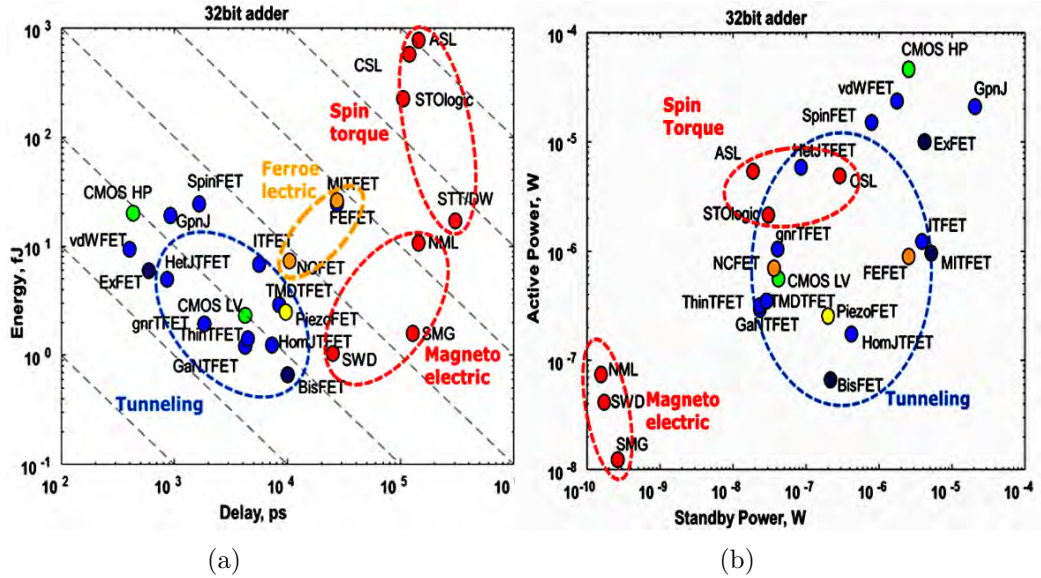


Figure 1.5: (a) Switching delay vs energy required to switch states of some beyond-CMOS devices for 32-bit adder circuit. (b) Standby power dissipation vs power dissipation in active states for 32-bit adder circuit. The figures are taken from [14]

FETs made of van der Waal materials (vdwFET), Tunneling Field Effect Transistors (TFET) etc [14][16]. Extensive studies on benchmarking of these device technologies in circuit level applications reveal interesting results [17]. Fig. 1.5 shows the benchmarking results of some of the beyond-CMOS technologies for a combinational circuit like a 32-bit adder. As seen from fig. 1.5a, FETs operating on the spintronic principle would require higher delay time compared to high-performance CMOS (CMOS HP) technology that lies on the left portion of the figure. Tunneling devices could provide lower delay and therefore faster-switching operations and lower energy dissipation for switching state compared to ferroelectric FETs (FEFETs) and spintronic devices. However, the delay is higher than high-performance CMOS technology. Van der Waal FETs (vdWFET) could provide similar speed characteristics as high-performance CMOS, however, they are not the least energy consuming devices either. Fig. 1.5b shows the active vs standby power dissipation of the same beyond-CMOS technologies for 32-bit adder which reveals that tunneling devices can provide standby power somewhat in between spintronic and high-performance CMOS devices. They can also provide the least active power dissipation of the three technologies. Fig. 1.6 shows the power density vs computational throughput from the same technologies. In this study, the power density was capped at 10 W/cm<sup>2</sup> which basically demonstrates the computational throughput of the technologies in a power constrained scenario. Computational throughput is a measure of useful work performed by a circuit and is measured in terms of the number of integer operations performed per second per unit area [14]. Under constrained power environment, CMOS HP cannot achieve maximal throughput. Device technologies like van der Waal FETs (vdwFET) and Hetero-junction TFET (HJTfET) can provide maximal throughput in



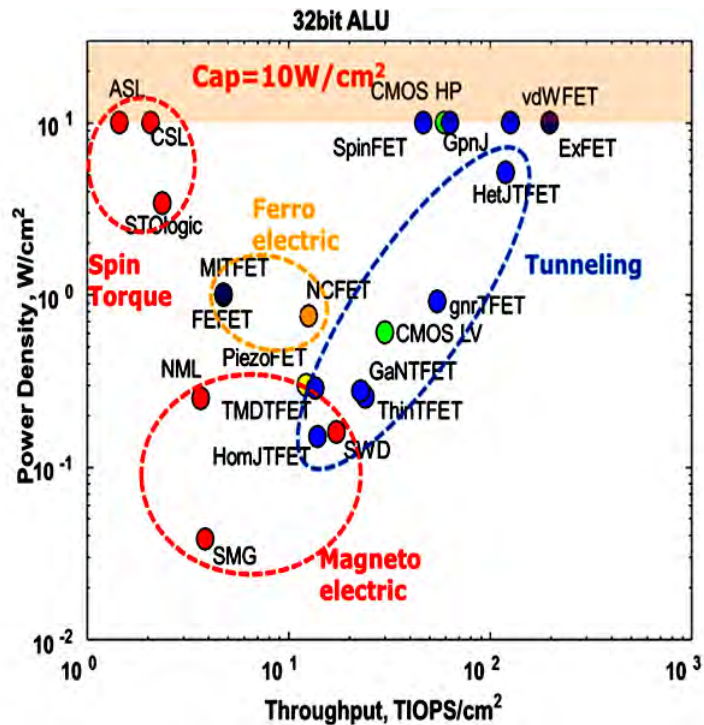


Figure 1.6: Computational throughput vs power density for some of the beyond-CMOS device technologies [17]

a power constrained environment. TFETs could also lower power density than CMOS HP. Spintronic devices are projected to provide high power density and low throughput.

## 1.2 Why TMDC

Till now silicon has been the workhorse of the semiconductor industry. Although pristine silicon has been used as a channel material in MOSFET for quite a while, strained silicon for enhanced device performance was introduced in 90 nm technology node [3]. However, as transistor dimensions are scaled down to keep in touch with Moore's Law, power density increases. In order to keep the power density at a constrained limit while increasing transistor density, the supply voltage must be scaled down [18] which would compromise switching speed. A possible way around of this problem is to introduce new channel material in MOSFET technology where charge carriers travel at a much higher velocity than in silicon. This would allow a reduction in voltage without a loss of performance. III-V compound semiconductors, their ternary, quaternary alloys are considered as channel materials in transistors due to their high carrier mobility and injection velocity [18] [19]. Apart from III-V compound semiconductors, a new class of materials- 2D materials has recently attracted a lot of interest due to their exciting electronic and

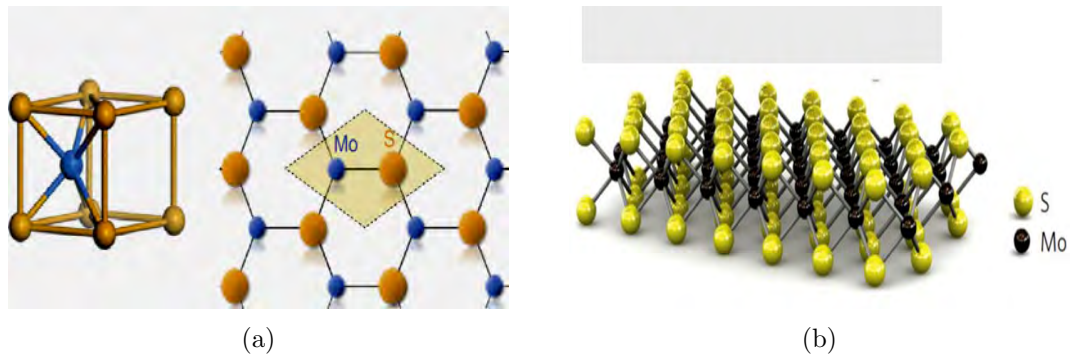


Figure 1.7: (a) Unit cell on monolayer MoS<sub>2</sub>. Mo atom is covalently bonded to six S atoms. A top view of the lattice is also shown [29]. (b) The structure of monolayer MoS<sub>2</sub> [30].

optoelectronic properties. Perhaps the most exciting aspect of 2D materials investigation is the stability of their monolayer or few layer structures and potential in integrated electronics. Although Graphene was the first mechanically exfoliated 2D material [20], pristine Graphene does not have a bandgap which makes it incompatible with transistor application. Artificial mechanisms can be used to open bandgap in Graphene. These mechanisms include creating structures like Graphene nanoribbons [21] [19] [20] [22], applying external strain [23] [24] and external electric field [25][26][27]. On the other hand, beyond-Graphene 2D materials like Transition Metal Dichalcogenides (TMDCs) show tunable intrinsic bandgap properties. The bandgap of these materials not only depend on their constituent atoms but also on the number of layers which make these materials highly tunable and widely applicable for electronic devices [28]. Besides, the stability of monolayers of these materials further makes them highly convenient for UTB devices.

Among the existing TMDC materials, Mo and W based TMDCs are semiconductors with band gaps ranging from the visible to the near-infrared [31]. Predictions based on first principle simulation of TMDC materials state that chalcogenides of Ti, Sn, and Zr are also semiconducting in nature. However, there is little or no evidence of the existence of these materials in monolayer form or performance in electronic applications [32] [33] [34]. Thus, Mo and W chalcogenides have been the most heavily investigated and extensively studied among the post-Graphene two-dimensional materials [31].

From a structural point of view, layered TMDCs are similar to Graphite with monolayer thickness of 0.6nm-0.7nm and weak van der Waals force between different layers. The chemical formula of these materials can be given as MX<sub>2</sub> (M= Transition Metal atom; X= Chalcogen atom). For a monolayer TMDC, hexagonally ordered Transition metal atoms are sandwiched between two hexagonally ordered layers of Chalcogen atoms [31]. Fig. 1.7 shows unit cell configuration of MoS<sub>2</sub> and its monolayer structure. First

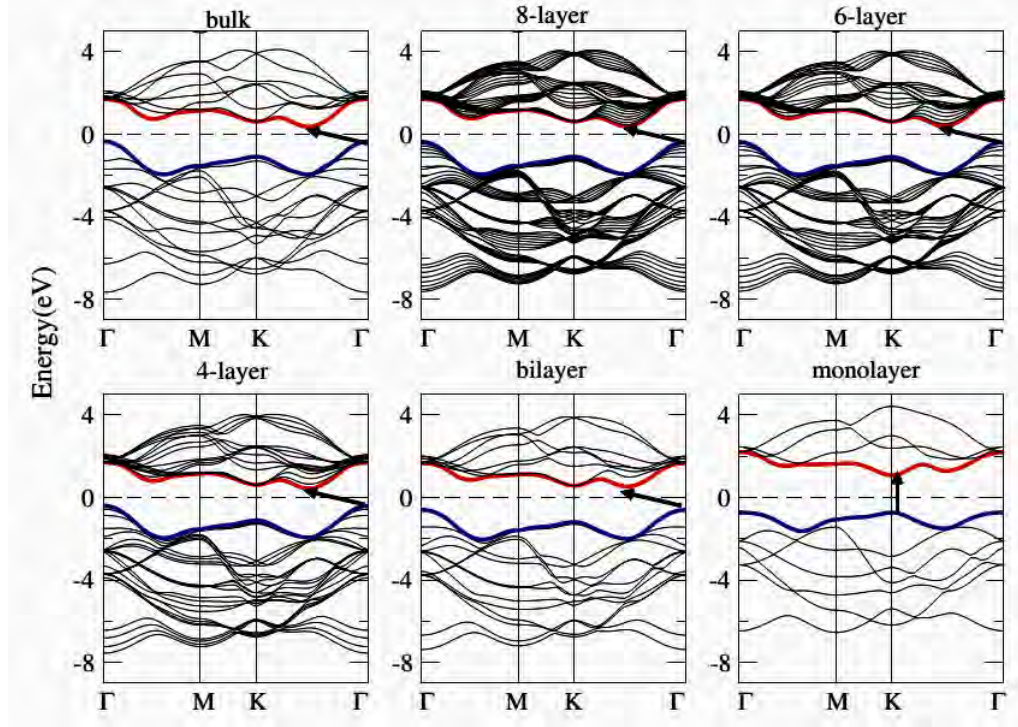


Figure 1.8: Bandstructure of multilayer MoS<sub>2</sub>. The bottom of the conduction band and the top of the valance band are highlighted in red and blue respectively(in bold lines). The transition from indirect to direct bandgap is observed as the number of layers is decreased. A monotonic increasing trend in bandgap is also observed with decreasing number of layers. Figures are taken from [40].

principle simulation of semiconducting TMDC materials reveals interesting electronic properties. Semiconducting nature of these materials is strongly affected by the number of layers, external strain, and electric field. As we approach monolayer thickness, the bandgap of these materials shows indirect to direct transition. At the same time, bandgap also shows a monotonic increasing tendency with the decreasing number of layers [35]. Fig. 1.8 shows the bandgap of MoS<sub>2</sub> as we decrease the number of layers from bulk to monolayer. The bandgap shows transition from 1.2 eV(bulk) to 1.9 eV(monolayer) [35]. At the same time, indirect to direct bandgap transition is also observed. Application of external strain is another approach of tuning electronic properties of these materials. In the semiconducting state, strain induction also causes indirect to direct transition in bandgap [35]. TMDCs based on Mo and W show semiconductor to metal transition under the application of in-plane tensile strain [36] [37]. The application of electric field shows a different trend when compared to Graphene. Although perpendicular electric field opens up bandgap in Graphene, application of electric field causes decrease in bandgap in monolayer TMDC materials and causes semiconducting to metallic transition as reported in the literature [38] [39].

The presence of intrinsic bandgap makes monolayer or few layer TMDC materials ideally

suitable for applications in UTB electronic devices. For applications in digital electronics, MOSFETs must have a high ‘on’/‘off’ current ratio. The high bandgap of monolayer TMDC materials can help achieve this high ‘on’/‘off’ ratio which is not possible with gapless Graphene. The first demonstration of monolayer TMDC material in MOSFET took place in 2011 when Radisavljevic et al. reported single layer MoS<sub>2</sub> transistor with high-k HfO<sub>2</sub> as gate dielectric [41]. Room temperature mobility of 200 cm<sup>2</sup>/V/s and ‘on’/‘off’ ratio in the region of 10<sup>8</sup> were reported which clearly demonstrated the potential of these materials in ultra-low power electronics. The high carrier mobility of monolayer MoS<sub>2</sub> was attributed to the high-k material used as the gate dielectric [41]. Carrier transport in layered TMDC MOSFETs is also affected by layer thickness, as suggested by experimental investigation and theoretical modeling. Electrons in monolayer MOSFETs are weakly screened from the substrate imperfections and interfacial effects due to ultra-thickness of monolayers. This makes carrier mobility in monolayer TMDC devices highly sensitive to the nature of interfaces on both sides of the channel. Increase in carrier mobility is observed with increase in layer thickness [42] [43]. However, with increasing layer thickness i.e. increasing the number of layers in the device, mobility does not show a monotonically increasing trend. This occurs due to the buildup of finite interlayer resistance which tends to decrease carrier mobility at higher layer thickness [44]. Therefore, the reported thickness of MoS<sub>2</sub> layer which corresponds to maximum optimum mobility ranges between 6 nm to 12 nm [44].

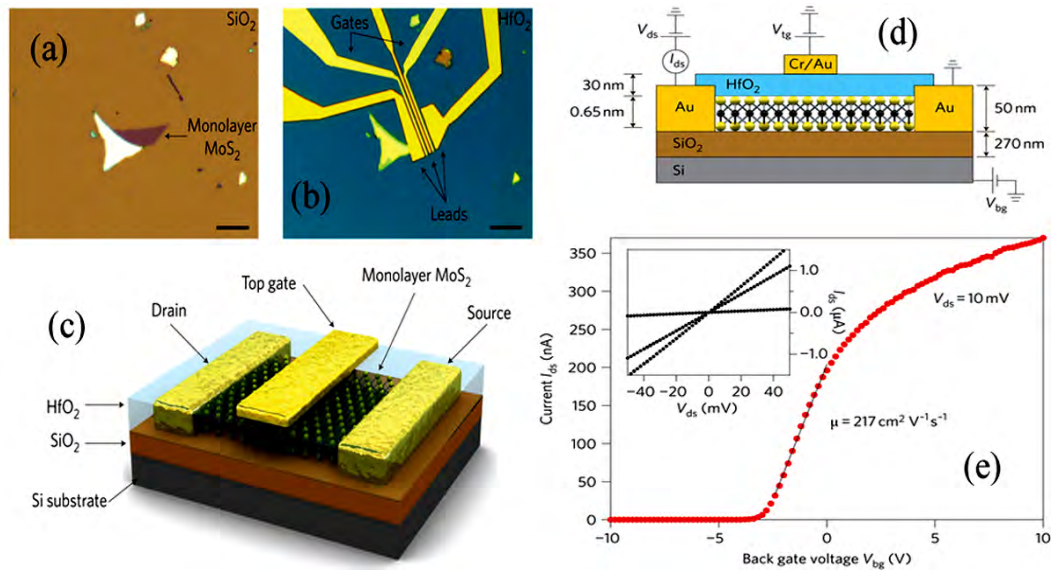


Figure 1.9: (a) Optical image of a single layer of MoS<sub>2</sub> (thickness, 6.5 Å); (b) Optical image of a device based on the flake shown in (A); (c) Three-dimensional schematic view of MoS<sub>2</sub> transistor; (d) Cross-sectional view of the monolayer MoS<sub>2</sub> FET structure; (e) Transfer characteristics at room temperature with 10 mV applied drain bias voltage, V<sub>ds</sub>. The inset figure shows output characteristics of the device with back gate bias voltage, V<sub>bg</sub> of 0, 1 and 5 V. The images are taken from [41]



In order to understand the full potential of layered TMDC materials in electronic applications, the physics of contact formation of these materials with different materials is also studied in great detail [45] [46] [47]. Investigations reveal that non-rectifying ohmic contacts are formed when low work-function metals (Sc or Ti) are used which is required for high carrier injection and low contact resistance. Ti has been experimentally implemented in both MoS<sub>2</sub> and WSe<sub>2</sub> FETs with good contact characteristics [44] [47]. High work function materials like Au also show linear output characteristics i.e. ohmic nature when used in MoS<sub>2</sub> MOSFETs due to the formation of low resistance tunneling contact thanks to exceptionally narrow tunneling distance provided by ultra-thin monolayer MoS<sub>2</sub> [31].

### 1.3 Thesis Objectives

The objectives of this work can be given as follows:

- To investigate the electronic properties of MoS<sub>2</sub> /MX<sub>2</sub> /MoS<sub>2</sub> trilayer heterostructures at different stacking configurations by implementing first principle simulation method using density functional theory and to study the effect of in-plane bi-axial strain on the electronic properties and bandstructure of the trilayer heterostructures.
- To develop a 2-D numerical quantum ballistic transport simulator using Non-Equilibrium Green's Function (NEGF) formalism with parameters extracted from electronic property investigation and study the potential of the studied trilayer heterostructures as channel materials for extremely scaled FETs for future technology nodes.

### 1.4 Organization of the Thesis

The entire thesis can be organized briefly in the following manner:

- The first chapter discusses the current state and challenges in CMOS technologies briefly, introduces beyond- CMOS technologies that are explored as potential candidates for next generation processors. The chapter also introduces TMDC materials briefly, discusses potential as channel materials in transistor application.
- The second chapter contains an exploration of MoS<sub>2</sub>- its electronic structure, physics and electronic devices. The chapter will also discuss the current state



---

of bilayer and trilayer TMDC heterostructures based on MoS<sub>2</sub> and their device applications.

- The third chapter discusses the theoretical background behind material level simulation of TMDC materials using Density Functional Theory. The chapter also discusses the simulation procedure and computational methods used to explore trilayer TMDC heterostructure MOSFETs using simplified Fast Uncoupled Mode Space Approach.
- The fourth chapter will present results extracted from material and device level simulation of trilayer MoS<sub>2</sub> heterostructure. The first section of this chapter will discuss results obtained from numerical simulations of electronic properties of trilayer MoS<sub>2</sub> heterostructures. The second section would present results obtained from quantum ballistic simulation of 10 nm double gate MOSFET using material parameters obtained from the first section.
- The fifth chapter will draw a conclusion on the results obtained from this work and suggest scopes for future development.

## Chapter 2

# Exploration of MoS<sub>2</sub>: It's Physics and Devices

### 2.1 MoS<sub>2</sub>: Crystal Structure

The intrinsic limitations of Graphene have led to a great deal of research efforts in materials that are both two dimensional in nature and can be used for exciting electronic and optoelectronic applications. Transition Metal Dichalcogenides or TMDCs belong to this class of beyond-Graphene 2D materials while MoS<sub>2</sub> has been the most widely studied TMDC both theoretically and experimentally.

Monolayer MoS<sub>2</sub> can have two phases: trigonal prismatic or octahedral. The trigonal prismatic phase, where the S atoms are vertically aligned, can be described by a hexagonal geometry and is referred to as 2H (1H is monolayer). In the octahedral phase,

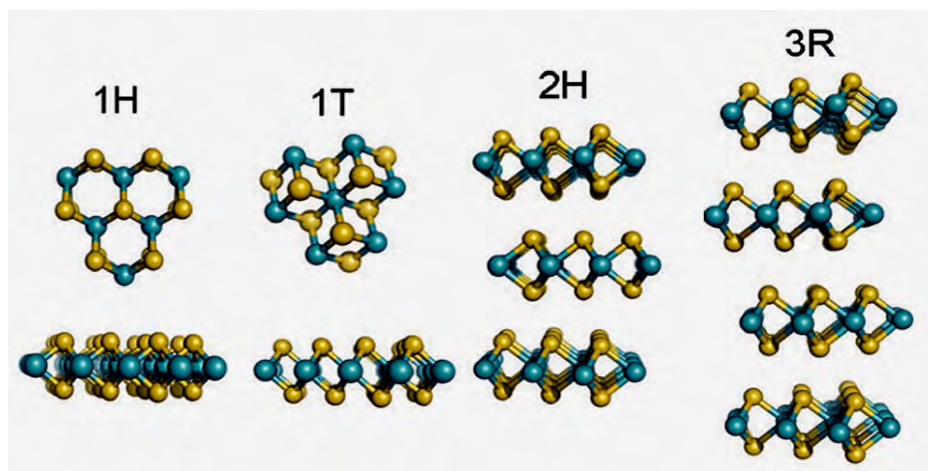


Figure 2.1: Different phases and stacking configurations of MoS<sub>2</sub>. Transition metal atoms are shown in blue color. Chalcogen atoms are shown in yellow color.

also known as 1T phase, one layer of S atoms is shifted compared to the other in the monolayer. Besides these phases, different stacking ways of 1H MoS<sub>2</sub> monolayers give rise to two other phases. They are known as 2H and 3R phase. These phases are all shown in fig. 2.1 [48]. Bulk MoS<sub>2</sub> is formed by a large number of monolayers stacked on top of each other bonded by weak van der Waal interaction. Monolayer TMDCs form honeycomb lattice structures just like Graphene. Here, Transition metal atoms are positioned in a hexagonal pattern and are sandwiched between two layers of Chalcogen atoms. In the monolayer, one Mo atom is connected to six S atoms by strong covalent bonds. The presence of strong interaction between atoms within the monolayer and weak interaction between layers allow the exfoliation of monolayer ultra-thin MoS<sub>2</sub> crystals. The structural data on MoS<sub>2</sub> monolayers are available in the recent literature. First principle simulation using generalized gradient approximation (GGA) with Perdew-Burke-Ernzerhof (PBE) exchange-correlation functional reveals the following structural parameters for monolayer MoS<sub>2</sub> unit cell as reported in 2.1

**Table 2.1: Structural Parameters of MoS<sub>2</sub> Monolayer**

Property	Value
Lattice Constant	3.23 Å
Bond Length (Mo-S)	2.45 Å
Distance (S-S)	3.18 Å
Bond Angle (S-Mo-S)	80.88 degrees

## 2.2 Electronic Properties of MoS<sub>2</sub>

First principle simulation reveals bulk MoS<sub>2</sub> to be an indirect bandgap material with the valance band maxima occurring at  $\Gamma$  point and conduction band minima occurring at Q (between  $\Gamma$  point and K point) point in the Brillouin zone. The bandstructure of bulk MoS<sub>2</sub> is shown in fig. 2.2a. However, the electronic bandstructure shows high sensitivity to layer thickness and shows a monotonically increasing bandgap tendency with bulk to monolayer transition. The indirect bandgap of bulk MoS<sub>2</sub> is about 1.3 eV [49]. The valance band maxima at  $\Gamma$  point is diffused and consists of Mo d-type orbitals and S p-type orbitals. On the other hand, conduction band minima at K point is localized and consists of Mo d-type orbitals [50]. As the number of layers decreases from bulk to monolayer, the valance band energy at  $\Gamma$  point gradually decreases and conduction band energy at Q point increases. As a result, the magnitude of indirect bandgap increases and the bandgap nature changes from indirect to direct nature. The direct bandgap at K point remains fairly unchanged with decreasing number of layers. This observation of indirect to direct transition with layer thickness is also suggested by Cheng et al. [51]. This study suggests that the transition from indirect to direct bandgap nature

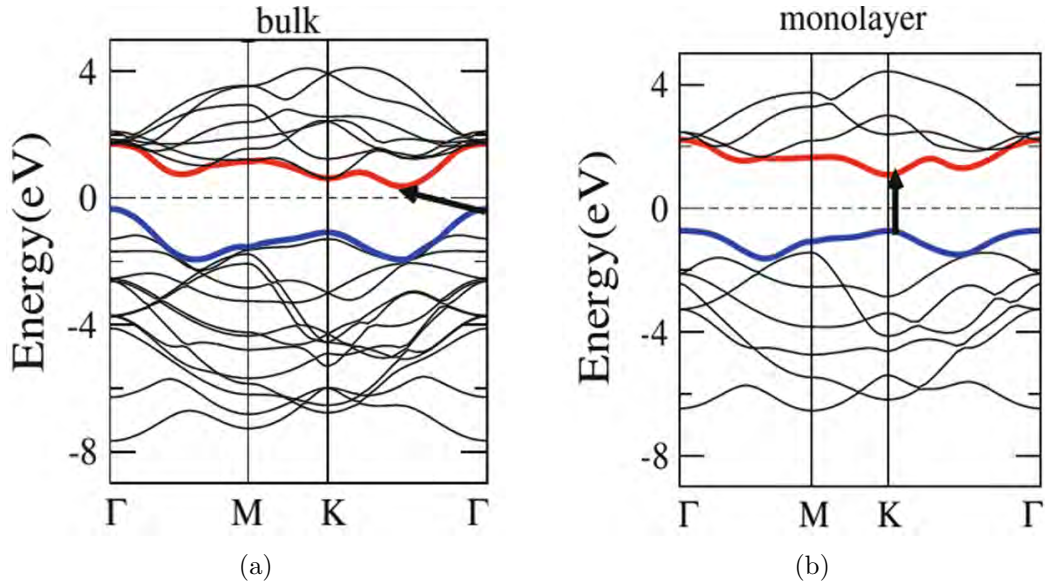


Figure 2.2: (a) Bandstructure of (a) bulk MoS<sub>2</sub> and (b) monolayer MoS<sub>2</sub> obtained from first principle simulation [36]. As can be seen, bulk MoS<sub>2</sub> shows indirect bandgap nature while monolayer MoS<sub>2</sub> is a direct bandgap material.

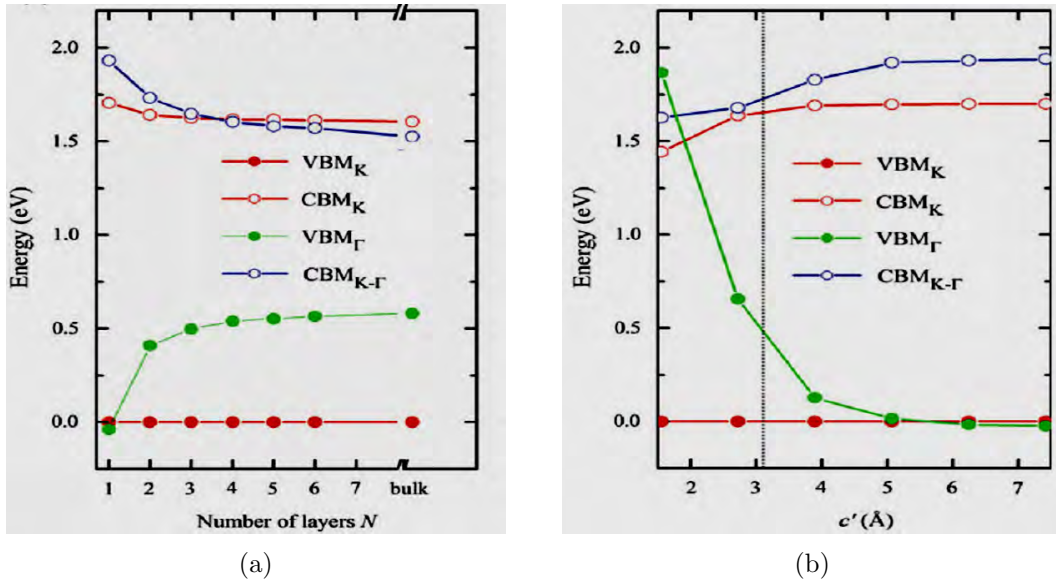


Figure 2.3: (a) Variation of conduction and valence band energies in MoS<sub>2</sub> at different symmetry point in the first Brillouin zone of MoS<sub>2</sub> as a function of the number of layers. (b) Effect of interlayer coupling on the conduction and valence band energies as the interlayer distance is varied. The images are taken from [51].

may be triggered by interlayer coupling that becomes significant as layers are brought together. Fig. 2.3b shows the effect of interlayer coupling on the electronic states of MoS<sub>2</sub> [51]. As seen from the figure, as layers are brought closer, strong interlayer interaction leads the increment in the energy of the valence band maxima at  $\Gamma$  point. The valence band at K point remains fairly unchanged. The conduction band minima at K point shows a slight decrease in energy as layers are brought closer.

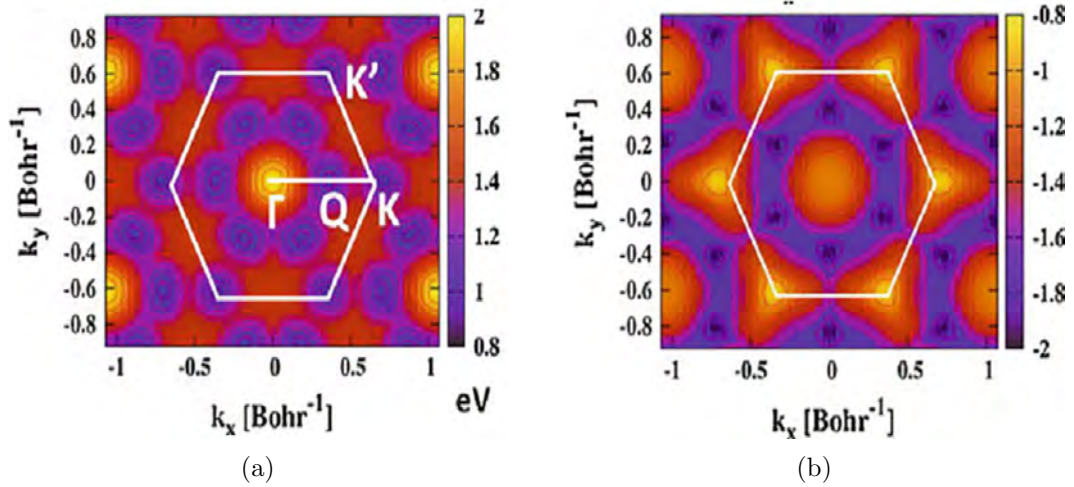


Figure 2.4: Topology of monolayer MoS<sub>2</sub> (a) Conduction and (b) Valance band over the first Brillouin zone [52]. As can be seen from the figure, the effective masses at K point shows isotropic nature for both conduction and valance band.

Kadantsev et al. [52] showed the topology of conduction band and valance band in the first Brillouin zone of MoS<sub>2</sub> monolayers from first principle study. This study also reveals that, for MoS<sub>2</sub> monolayers, the maximum position in the valance band appears at K point and  $\Gamma$  point with the global maxima appearing at K point for the monolayer. On the other hand, the conduction band appears to have a global minimum point in energy and this global minimum occurs at K point. The topological nature of conduction and valance band of MoS<sub>2</sub> monolayer are shown in fig. 2.4. The effective masses at various symmetry points in the Brillouin zone have also been studied. For monolayer MoS<sub>2</sub>, as can be seen from fig. 2.4, the effective masses at K point in the Brillouin zone are isotropic. This isotropic nature is applicable for both electrons and holes. For monolayer MoS<sub>2</sub>, the effective mass varies within the range of 0.35 to 0.55 as reported in the literature [49]. Hole effective mass, on the other hand, varies within 0.43 to 0.64 [49].

### 2.3 Tunable Electronic Properties of MoS<sub>2</sub>

Just like 2D Graphane, electronic properties of MoS<sub>2</sub> are also responsive to externally applied effects like strain, external electric field etc. However, the changes in electronic properties to these external effects are somewhat different from the trend observed in Graphene. External strain has been investigated as a way to engineer electronic properties of pristine Graphene [53]. Bandgap as high as 0.486 eV has been reported from

first principle calculations in literature for externally applied strain of 12.2 % [54]. Application of vertical electric field opens up bandgap in pristine Graphene [25]. Electric field tunable bandgap of up to 200 meV has been reported in the recent literature [55].

The effect of in-plane strain on the lattice structure and electronic properties of MoS<sub>2</sub> has been studied in detail using atomistic simulation. Kumar et al. [56] reported the results of in-plane strain application on the lattice structure of monolayer MoS<sub>2</sub>. In-plane tensile strain elongates Mo-S bond length, shortens S-S distance in the unit cell. On the other hand, application of compressive strain shortens Mo-S bond length and elongates S-S distance. Strain causes a change in bond angles as well. Compressive(tensile) strain increases(decreases) S-Mo-S bond angles [56].

Strain introduction causes interesting changes in the bandstructure of MoS<sub>2</sub>. Using first principle DFT-based methods, Johari et al. [57] demonstrated the effect of uniaxial and biaxial in-plane tensile strain on several monolayer semiconducting TMDC materials. Their finding on MoS<sub>2</sub> monolayer under in-plane strain application is shown in fig. 2.5. Application of tensile strain and shear strain was observed in their study. Tensile strain lowers bandgap of monolayer MoS<sub>2</sub>, as can be seen from fig. 2.5a. Tensile strain also changes the position of conduction band minima and valance band maxima positions in the Brillouin zone. The bandstructure shows similar effect under the influence of shear strain. The figure also reveals that at about 10% tensile strain application monolayer MoS<sub>2</sub> changes from semiconducting the metallic nature. Similar results were also observed by Yun et al. [35] who investigated the effect of both tensile and compressive strains by tuning the lattice constant. According to this study, application of compressive strain increases bandgap of monolayer MoS<sub>2</sub> which is accompanied by a direct to indirect transition. These observations are shown in fig. 2.5b.

Electronic properties of MoS<sub>2</sub> can be further manipulated by externally applied electric field. Ramasubramaniam et al. [38] studied the effect perpendicular electric field on the electronic bandstructure of bilayer MoS<sub>2</sub> and reported that, although bilayer MoS<sub>2</sub> bandstructure is similar to bulk MoS<sub>2</sub> i.e. indirect in nature, with applied electric field, it's bandgap decreases and shows direct nature. With increasing perpendicular electric field, conduction band minima and valance band maxima both shift to K point in the Brillouin zone. At about 3 V/nm electric field value, MoS<sub>2</sub> bilayers become metallic i.e. the bandgap drops to 0 eV. Effects of vertical electric field on bilayer MoS<sub>2</sub> bandstructure is shown in 2.6.



## 2.4 MoS<sub>2</sub>: Multilayer Structures

Besides monolayer TMDC materials, bilayer and trilayer heterostructures of TMDC materials have attracted interest from the research community. Stacking monolayers of different TMDC materials on top of each other provides a new window in modulating electronic properties of these materials [58]. Exciting structural, electronic, optoelectronic and optical properties of TMDC bilayer TMDC heterostructures have been investigated using first principle atomistic calculations [59] [60] [61] [62].

Komsa et al. [63] performed first principle calculation on some MoS<sub>2</sub> based bilayer TMDC heterostructures using Vienna Ab-initio Simulation Package (VASP) [64]. They used plane wave basis set with 500 eV cut-off energy and Perdew-BurkeErnzerhof (PBE) exchange-correlation functional [65]. Their study found electronic states of the heterostructures to be highly localized at the constituent monolayers i.e. individual monolayers contributing for conduction and valance band states. At K point in the Brillouin zone, conduction band and valance band states were found to be localized at MoS<sub>2</sub> and WS<sub>2</sub> monolayers respectively. Their study found MoS<sub>2</sub>/WS<sub>2</sub> bilayer heterostructure to be indirect bandgap and MoS<sub>2</sub>/WSe<sub>2</sub> and MoS<sub>2</sub>/MoTe<sub>2</sub> bilayer structures to be direct bandgap materials.

Effect of stacking configuration on the electronic properties of the bilayer structures is also investigated. Terrones et al. [66] studied properties of semiconducting TMDC bilayer heterostructures using two different stacking configurations-AA and AB as shown in fig 2.7a. Their study also revealed MoS<sub>2</sub>/WS<sub>2</sub> bilayer heterostructures to be indirect bandgap ( $\Gamma$ -Q) materials under relaxed condition in both AA and AB stacking configuration of the bilayer. On the other hand, MoS<sub>2</sub>/WSe<sub>2</sub> bilayer was found to be direct bandgap (K-K) material. These findings are shown in fig. 2.7b.

Later on, like monolayer, effects of mechanical strain and external electric field on these bilayer heterostructures were also investigated. Lu et al. [39] demonstrated external in-plane strain and vertical electric field as effective tools in tuning electronic properties of TMDC bilayer heterostructure. According to their investigation, bilayer TMDCs also show a monotonic decreasing tendency in bandgap and direct-indirect bandgap transition with applied tensile strain and gradually transform from semiconducting to metallic state with tensile strain application. The amount of strain required for semiconducting to metallic or direct to indirect transition depends on the constituent monolayers. Uniaxial tensile strain also lowers bandgap. However, the observed trend is different from the biaxial strain. The application of vertical electric field also shows similar effects like monolayer TMDCs. These bilayers also show direct-indirect transition and a decrease in bandgap under the influence of perpendicular electric field.

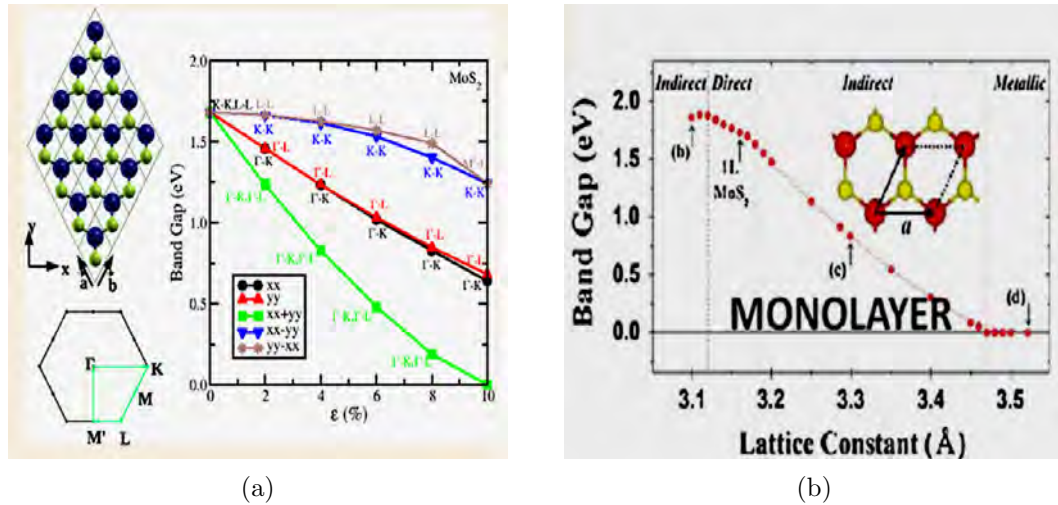


Figure 2.5: (a) Change in the bandgap of monolayer MoS<sub>2</sub> under strain application [57]. The nature of the bandgap is also presented in the figure. The results are shown for tensile strain application only. (b) The bandgap of monolayer MoS<sub>2</sub> under in-plane strain application ranging from compressive to tensile regime [35]

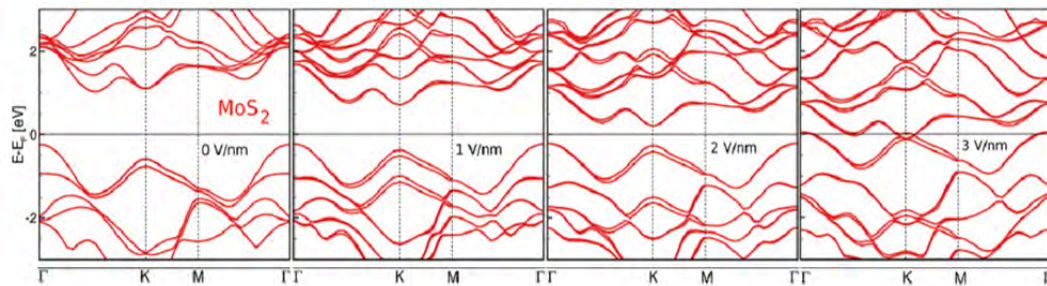


Figure 2.6: Bandstructure of bilayer MoS<sub>2</sub> under the influence of an external electric field [38]. With increasing electric field in bilayer MoS<sub>2</sub> the bandgap makes transition from indirect to direct nature. The bandgap also reduces with increasing electric field and at about 3 V/nm electric field, MoS<sub>2</sub> bilayer transforms from semiconducting to metallic state.

Apart from bilayer heterostructures, the effect of intercalation of 2D monolayers (boron nitride (BN) or another TMDC) between two layers of TMDC materials has been studied theoretically. Lu et al. [67] showed that intercalation of 2D monolayers can be used as an effective tool to further modulated electronic properties of TMDC materials. Moreover, their stacking at different configuration could lead to further tuning in their lattice structure and electronic properties. The trend of bilayer heterostructure formation is not limited to TMDC materials only. Heterostures of TMDC and other 2D materials have also been investigated theoretically and experimentally. Ebnonnasir et al. [68] showed the effect of Graphene orientation with respect to MoS<sub>2</sub> monolayer on the electronic properties of monolayer MoS<sub>2</sub>. The change in bandgap was attributed to changing thickness of MoS<sub>2</sub> layer as under the influence of changing Graphene orientation. Shi et al. [69] demonstrated a low-temperature MoS<sub>2</sub>/Graphene hybrid heterostructure



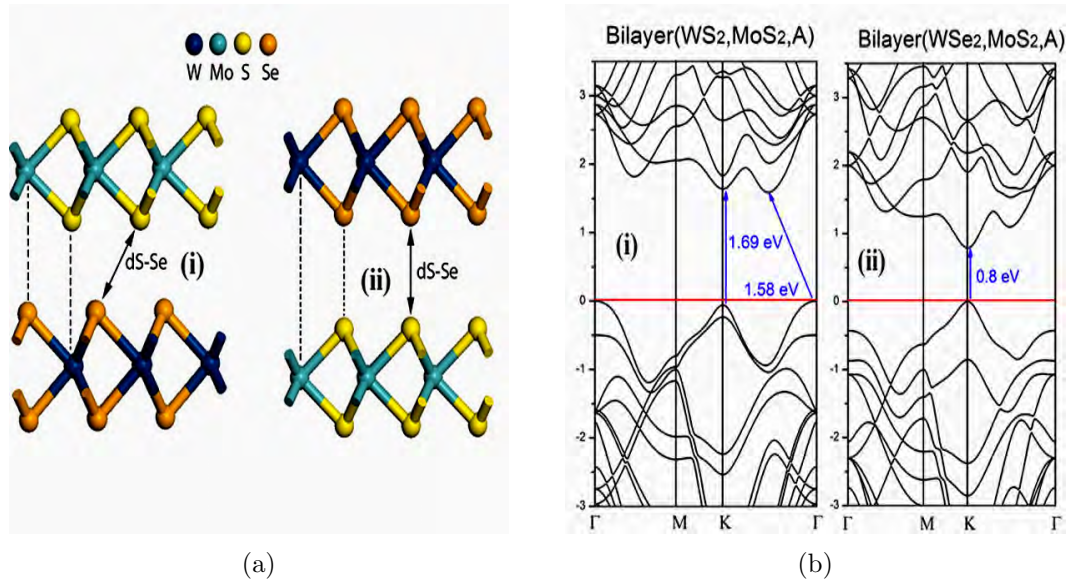


Figure 2.7: (a) Bilayer stacking of TMDC materials as shown in [66]. (i) shows the AB stacking (ii) shows the AA stacking. (b) Bandstructure of TMDC bilayers obtained from first principle analysis for (i) MoS<sub>2</sub>/WS<sub>2</sub> bilayer and (ii) MoS<sub>2</sub>/WSe<sub>2</sub> bilayer in AA stacking configuration [66].

growth technique using a growth template of graphene-covered Cu foil. The resulting hexagonal crystalline MoS<sub>2</sub> monolayer flakes range from several hundred nanometers to several micrometers. Lin et al. [70] demonstrated the growth of uniform large-size MoS<sub>2</sub>/graphene heterostructures fabricated directly on sapphire substrates with layer number controllability by chemical vapor deposition (CVD). The layer numbers of MoS<sub>2</sub>/graphene heterostructures were verified by high-resolution transmission electron microscopy (HRTEM) imaging. Moreover, the study also reported the growth of double heterostructures of graphene/MoS<sub>2</sub>/graphene by CVD fabrication of graphene layers on top of the MoS<sub>2</sub>, as confirmed by the cross-sectional HRTEM.

## 2.5 MoS<sub>2</sub>: Monolayer and Multilayer Devices

Radisavljevic et al. [41] demonstrated monolayer MoS<sub>2</sub> transistor with high-K dielectric HfO<sub>2</sub> in 2011. Monolayer MoS<sub>2</sub> was obtained using mechanical exfoliation method and was transferred to Si substrate covered with 270 nm SiO<sub>2</sub>. Au was used as source and drain contact. Characterization at room temperature revealed carrier mobility in the region of 200 cm<sup>2</sup>/V/s. This high mobility was attributed to suppression of Coulomb scattering in the presence of high-K gate dielectric environment [41].

Lin [71] et al. reported monolayer MoS<sub>2</sub> FET with enhanced mobility using a thin layer of polymer electrolyte (PE) consisting of polyethylene oxide (PEO) and lithium perchlorate (LiClO<sub>4</sub>) instead of high-K gate dielectric on top of the channel. The enhanced mobility

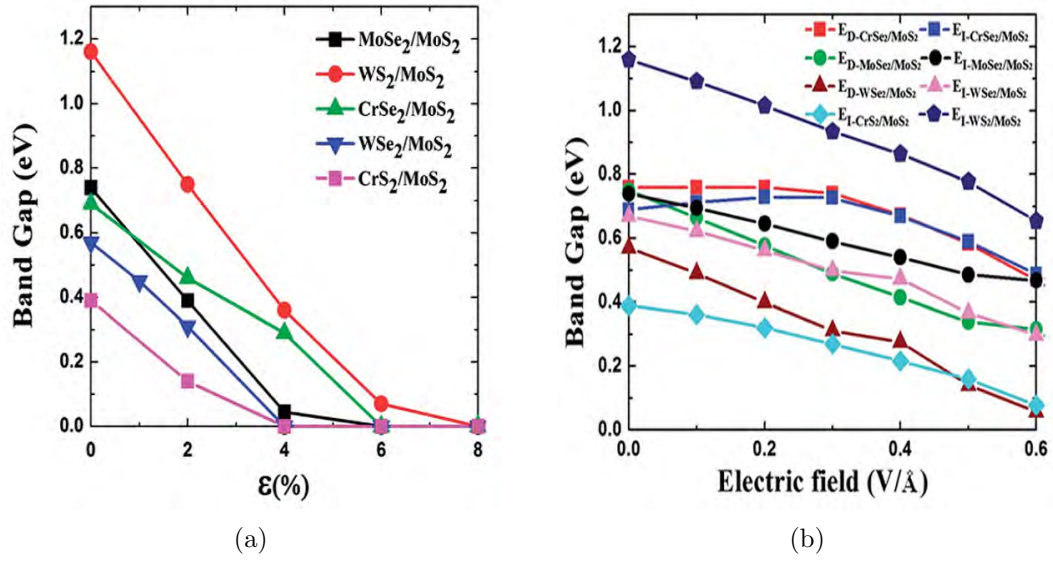


Figure 2.8: (a) Effect of biaxial strain on the bandgap of several bilayer TMDC heterostructure. With increasing in-plane biaxial strain, all the TMCD bilayers show semiconducting to metal transition. (b) Effect of the perpendicular electric field on the bandgap of bilayer TMDC which shows a monotonic decreasing trend with increasing electric field [39]

was attributed to reduced contact resistance in polymer electrolyte environment. A thin layer of PEO/LiClO<sub>4</sub> deposited on top of the devices not only substantially reduced the contact resistance but also boosted the channel mobility, leading up to three-orders-of-magnitude enhancement of the field-effect mobility of the device. When the PE is used as a gate medium, the MoS<sub>2</sub> field-effect transistors exhibit excellent device characteristics such as a near ideal subthreshold swing and an on/off ratio of 10<sup>6</sup> as a result of the strong gate-channel coupling.

Wang et al. [72] demonstrated large-scale CVD growth of monolayer MoS<sub>2</sub> and fabrication of integrated devices and circuits for the first time. Electrical characterization of the devices revealed on-state current of 16  $\mu\text{A}/\mu\text{m}$  at  $V_{DS}=5$  V and  $V_{TG}=2$  V. The threshold voltage was found to be at -2 V which indicated n-type doping the growth and fabrication process. The peak transconductance was around 3  $\mu\text{S}/\mu\text{m}$ . Their work also reported operation of simple logic circuits inverter, NAND gates using n-type monolayer MoS<sub>2</sub> FETs which showed the possibility of using monolayer MoS<sub>2</sub> as circuit building blocks in digital electronics. They also demonstrated enhanced mode and depletion mode FETs based on bilayer MoS<sub>2</sub> and application of these devices in SRAM cell and ring oscillator circuits [73].

Qiu et al. [74] reported the effect of characterization environment on the performance of bilayer MoS<sub>2</sub> FETs. Their study revealed that these devices are sensitive to oxygen and water in the environment. Air exposure dramatically reduced the 'on' current up to

2 orders of magnitude. This phenomenon was attributed to the creation of additional scattering centers which were created due to chemisorption at the defect sites of MoS<sub>2</sub>. They also demonstrated that vacuum annealing could effectively remove the adsorbates and reversibly recover the device performances.

Liu et al. [47] demonstrated high performance few-layer MoS<sub>2</sub> FETs using high-K dielectric HfO<sub>2</sub> and Ti contact with record low contact resistance which was compatible with concurrent contact resistance in CMOS technology. Their work strongly highlighted the importance of good edge contact in enhanced device performance which could be achieved by using top gate geometry. Their fabricated MOSFET showed good saturation behavior with high on-current in the region of 24  $\mu\text{A}/\mu\text{m}$  for 5nm MoS<sub>2</sub>.

Bao et al. [75] studied the effect of substrate and dielectric materials on carrier mobility of bulk MoS<sub>2</sub> FETs. Their study revealed that carrier mobility of about 30-60  $\text{cm}^2/\text{V}\cdot\text{s}$  can be obtained when the devices are grown on SiO<sub>2</sub>. The devices also show n-type characteristics when grown on SiO<sub>2</sub>. On the other hand, multilayer MoS<sub>2</sub> grown on polymethyl methacrylate (PMAA) showed thickness dependent mobility with monotonic mobility increment with PMAA thickness. These devices grown on PMAA also showed ambipolar transport nature.

Kang et al. [76] introduced Mo contact in MoS<sub>2</sub> FETs and showed that, Mo can form high-quality contact interface with monolayer MoS<sub>2</sub> with zero tunnel barrier and zero Schottky barrier under source/drain contact, as well as an ultra-low Schottky barrier (0.1 eV) at source/drain channel junction due to strong Fermi-level pinning. At the same time, high mobility, high on-current and low contact resistance were experimentally demonstrated on both monolayer and multilayer MoS<sub>2</sub> transistors using Mo contacts in their study.

Although Graphene is a zero bandgap material, Graphene/MoS<sub>2</sub> hybrid technology has attracted a lot of interest where MoS<sub>2</sub> is used as channel material and Graphene is used in contacts. Yu et al. [77] studied Graphene/MoS<sub>2</sub> hybrid technology for large scale electronics and showed that the tunability of the graphene workfunction with electrostatic doping significantly improves the ohmic contact to MoS<sub>2</sub>. At the same time, use of 2D semiconductors like Graphene could improve effective carrier injection into the channel. The possible tunability of workfunction in Graphene can lead to unprecedented flexibility in contact formation with the channel materials in high-frequency FETs. Therefore this technological framework could eventually open door to new opportunities in designing a wide variety of electronic systems.

Besides electronic applications, Graphene/MoS<sub>2</sub> structures have also been used in optoelectronic applications. Zhang et al. [78] demonstrated large area CVD grown MoS<sub>2</sub>/Graphene ultra-thin photodetector with photoresponsivity in the region of 10<sup>7</sup> A/W. Roy et al. [79] demonstrated gate tunable photoconductive behavior of Graphene/MoS<sub>2</sub> hybrid transistors. Their study also revealed that the Graphene/MoS<sub>2</sub> hybrid system could function as a rewriteable optoelectronic switch or memory when subjected to time dependent photoillumination. The responsivity of the hybrids was found to be nearly 1x10<sup>10</sup> A/W at 130 K and 5x10<sup>8</sup> A/W at room temperature, making them the most sensitive Graphene-based photodetectors at that time.

## 2.6 The MX<sub>2</sub> Monolayer

In this study, the MX<sub>2</sub> monolayer can be one of the three TMDCs- MoSe<sub>2</sub>, WS<sub>2</sub> or WSe<sub>2</sub>. Monolayer MoSe<sub>2</sub> shows direct bandgap nature with bandgap of 1.47 eV. Bilayer MoSe<sub>2</sub> also shows direct bandgap nature as shown from first principle simulation. On the other hand, bulk MoSe<sub>2</sub> is indirect bandgap material with bandgap in the region of 0.9 eV [35]. Back gated field effect transistors with ultrathin n-type MoSe<sub>2</sub> flakes on SiO<sub>2</sub>/Si substrate have been reported having high ‘On’/‘Off’ ratio in the region of 10<sup>6</sup> [80]. Monolayer WS<sub>2</sub> on the other hand, shows slightly higher bandgap in the region of 2 eV. Like other TMDC materials, it also shows direct to indirect bandgap transition as the number of layers stacked on top of each other increases [35]. Single layer WS<sub>2</sub> transistors sandwiched between hexagonal BN (h-BN) has been reported with high mobility around 214 cm<sup>2</sup>/Vs and ‘On’/‘Off’ ratio of about 10<sup>7</sup> [81]. Monolayer WSe<sub>2</sub> shows direct bandgap nature with bandgap of 1.6 eV with gradually reduces to 1.2 eV as we gradually shift from monolayer to bulk structure [82]. The electronic properties of monolayer WSe<sub>2</sub> have been investigated for both p-type and n-type transistor applications. Liu et al. [83] demonstrated the role of metal contacts on the performance of monolayer WSe<sub>2</sub> FETs and reported that, high performance FETs with good contacts and small Schotky barrier heights can be obtained using metals with low work function. Their work also demonstrated the scalability of WSe<sub>2</sub> FETs for sub-5 nm channel length transistor applications and suggested that Ag can be used as a good contact material to monolayer WSe<sub>2</sub> [82]. Fig. 2.9 shows the bandstructure of monolayer MoSe<sub>2</sub>, WS<sub>2</sub> and WSe<sub>2</sub> as extracted from DFT analysis and tight binding modeling.

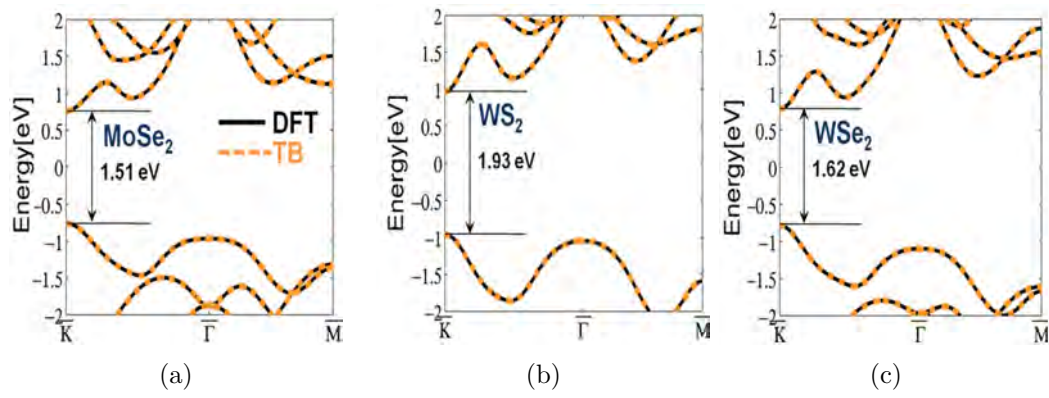


Figure 2.9: Extracted bandstructure from DFT calculation and tight binding modeling for monolayer (a) MoSe<sub>2</sub>; (b) WS<sub>2</sub>; (c) WSe<sub>2</sub> [84].

## Chapter 3

# Simulation Methods

### 3.1 Density Functional Theory: A Brief Overview

In simple words, density functional theory refers to a quantum mechanical modeling approach that allows us to calculate the ground state properties of a many body system. In this method, properties of the many body system under study are determined using functionals of spatially dependent electron density. DFT is widely regarded as one of the most versatile methods applied in computational chemistry and condensed matter physics.

#### 3.1.1 What We Seek

In order to discuss the properties of an interacting system such as electrons in a solid, one has to solve the many electron wave function. The first step, however, would be to solve the time-independent, non-relativistic Schrödinger equation [85]:

$$\hat{H}\Psi_i(\vec{x}_1, \vec{x}_2, \dots, \vec{x}_N, \vec{R}_1, \vec{R}_2, \dots, \vec{R}_M) = E_i\Psi_i(\vec{x}_1, \vec{x}_2, \dots, \vec{x}_N, \vec{R}_1, \vec{R}_2, \dots, \vec{R}_M) \quad (3.1)$$

where,  $\hat{H}$  is the Hamiltonian for a system with M nuclei and N electrons. The Hamiltonian can be written in general form as [85]:

$$\hat{H} = -\frac{1}{2} \sum_{i=1}^N \nabla_i^2 - \frac{1}{2} \sum_{A=1}^M \frac{1}{M_A} \nabla_A^2 - \sum_{i=1}^N \sum_{A=1}^M \frac{Z_A}{r_{iA}} + \sum_{i=1}^N \sum_{j>i}^M \frac{1}{r_{ij}} + \sum_{A=1}^M \sum_{B>A}^M \frac{Z_A Z_B}{R_{AB}} \quad (3.2)$$

Here, A and B run over the M nuclei while i and j denote the N electrons in the system.

The first two terms describe the kinetic energy of the electrons and nuclei. The other three terms represent the attractive electrostatic interaction between the nuclei and the electrons and repulsive potential due to the electron-electron and nucleus-nucleus interactions [85].

### 3.1.2 The Born-Oppenheimer Approximation

The problem stated above can be largely simplified by an approximation put forth by Max Born and J. Robert Oppenheimer. Using this assumption we can separate the motion of atomic nuclei and electrons. Since nuclei are much more massive compared to electrons, they must have very small velocities. Therefore, on a typical time scale of nuclear motion, the relaxation process to the ground state configuration of the light electrons will be instantaneous. So, by considering the nuclei to be stationary with respect to electrons, we can solve the time-independent Schrödinger equation for many body problem mentioned in eqn. 3.2 for the electronic ground state [86]. The Hamiltonian operator, therefore, can be reduced to:

$$\hat{H}_{elec} = -\frac{1}{2} \sum_{i=1}^N \nabla_i^2 - \sum_{i=1}^N \sum_{A=1}^M \frac{Z_A}{r_{iA}} + \sum_{i=1}^N \sum_{j>i}^M \frac{1}{r_{ij}} = T + \hat{V}_{Ne} + \hat{V}_{ee} \quad (3.3)$$

The solution of Schrödinger equation in this case would lead to electronic wave function,  $\Psi_{elec}$  of the many body system with electron energy  $E_{elec}$ . The total energy of the system then becomes the sum of electronic energy and constant nuclear repulsion energy  $E_{nuc}$

$$\hat{H}_{elec} \Psi_{elec} = E_{elec} \Psi_{elec} \quad (3.4)$$

$$E_{tot} = E_{elec} + E_{nuc} \quad \text{where} \quad E_{nuc} = \sum_{A=1}^M \sum_{B>A}^M \frac{Z_A Z_B}{R_{AB}} \quad (3.5)$$

Here, in eqn. 3.3 the second term can be considered as static external potential imposed by the static nuclei according to the Born-Oppenheimer approximation [86]. Therefore, the electronic hamiltonian operator can be decomposed into two components:

$$\begin{aligned} \hat{H} &= \hat{F} + \hat{V}_{Ne} \\ \hat{F} &= T + \hat{V}_{ee} \end{aligned} \quad (3.6)$$



Here, the operator  $\hat{F}$  is same for all N electron systems. Therefore, the number of electrons in the system, N and static external potential,  $\hat{V}_{N_e}$  determine the Hamiltonian operator and the ground state wavefunction  $\Psi_0$ . We can, therefore, express the ground state electron density  $n_0(\mathbf{r})$  [86] as:

$$n_0(\mathbf{r}) = \langle \Psi_0 | \hat{n} | \Psi_0 \rangle = \int \prod_{i=2}^N d\mathbf{r}_i |\Psi_0(\mathbf{r}_1, \mathbf{r}_2, \dots, \mathbf{r}_N)|^2 \quad (3.7)$$

### 3.1.3 The Hohenberg-Kohn Theorem [85][86]

According to Hohenberg and Kohn [87], the problem of ground state calculation of a interacting many electron system under the influence of an external potential can be solved by using a universal functional of electron density,  $F[n(\mathbf{r})]$  which is independent of the external static potential  $V_{ext}(\mathbf{r})$ . The Hohenberg-Kohn [H-K] theorem makes two remarkable statements:

- For ground state configuration, the static external potential must be uniquely expressed as a functional of the electron density  $n_0(\mathbf{r})$ . That is, the proper ground state carrier density,  $n_0(\mathbf{r})$  can uniquely determine the static external potential. This statement clearly states that two different ground state densities can not give the same external potential. The total number of electrons in the system can be written in terms of the electron density as  $N = \int d\mathbf{r} n_0(\mathbf{r})$ . The static external potential also determines the Hamiltonian operator and eventually the ground state electronic wave function. Therefore, this static potential also actively determines the ground state properties of the system.

So, for all densities  $n(\mathbf{r})$  which are ground-state densities for some external potential the functional  $F[n] = \langle \Psi | \hat{F} | \Psi \rangle$  is unique and well-defined, since  $n(\mathbf{r})$  determines the external potential and N (and therefore  $\hat{F}$ ) and thence  $|\Psi\rangle$ . According to this statement, a functional for an arbitrary external potential  $V(\mathbf{r})$  can be defined as [86]:

$$E_V[n] = F[n] + \int d\mathbf{r} V(\mathbf{r})n(\mathbf{r}) \quad (3.8)$$

Therefore,  $n(\mathbf{r})$  determines N and  $V_{ext}(\mathbf{r})$  and hence all the properties of the ground state, for example the kinetic energy  $T[n(\mathbf{r})]$ , the potential energy  $V[n(\mathbf{r})]$ , and the total energy  $E[n(\mathbf{r})]$ . Now, the total energy can be written as [85]:



$$E[n(\mathbf{r})] = E_{Ne} + T[n(\mathbf{r})] + E_{ee}[n(\mathbf{r})] = \int V_{Ne}(\mathbf{r})n(\mathbf{r})d\mathbf{r} + F_{HK}[n(\mathbf{r})] \quad (3.9)$$

$$F_{HK}[n(\mathbf{r})] = T[n(\mathbf{r})] + E_{ee} \quad (3.10)$$

The term  $F_{HK}[n(\mathbf{r})]$  contains the functional of kinetic energy and the electron-electron interaction term. This functional is universal in nature and is independent of the system at hand. The explicit form of this functional is still not known.

- The second H-K theorem states that, the lowest energy of the system can be obtained by using the functional  $F_{HK}[n(\mathbf{r})]$ , if the input density is the true ground state density. This is basically nothing but another presentation of the variational principle.

In other words this means that, if we have a trial electron density  $n(\mathbf{r})$ , which satisfies the necessary boundary conditions such as  $n(\mathbf{r}) \geq 0$ ,  $\int n(\mathbf{r})d\mathbf{r} = N$ , and which is associated with some external potential  $V_{ext}$ , the energy obtained using this trial density from eqn. 3.9 will provide an upper bound to the true ground state energy  $E_0$ .  $E_0$  results if and only if the exact ground state density is inserted in eqn. 3.9 [85].

### 3.1.4 The Kohn-Sham Equations [85][86]

The Kohn and Sham [88] method allows us the simplification of considering the interacting system of electrons by a fictitious system of non-interacting particles. According to the formulation depicted in [86], the variational problem for the Hohenberg-Kohn density functional can be written as:

$$\delta[F[n] + \int d\mathbf{r}V_{ext}(r)n(r) - \mu(\int d\mathbf{r}n(\mathbf{r}) - N)] = 0 \quad (3.11)$$

Kohn and Sham separated  $F[n]$  into three parts:

$$F[n] = T_s[n] + \frac{1}{2} \int d\mathbf{r}d\mathbf{r}' \frac{n(\mathbf{r})n(\mathbf{r}')}{|\mathbf{r} - \mathbf{r}'|} + \mathbf{E}_{xc}[\mathbf{n}] \quad (3.12)$$

in which  $T_s[n]$  is defined as the kinetic energy of a non-interacting gas with density  $n(\mathbf{r})$  (not the same as that of the interacting system), the second term is the classical

electrostatic (Hartree) energy and the final term is an implicit definition of the exchange-correlation energy which contains the non-classical electrostatic interaction energy and the difference between the kinetic energies of the interacting and non-interacting systems [86].

Using this separation, eqn. 3.11 can be rewritten:

$$\frac{\delta T_s[n]}{\delta n(\mathbf{r})} + V_{\text{KS}}(\mathbf{r}) = \mu \quad (3.13)$$

in which the Kohn-Sham potential  $V_{\text{KS}}(\mathbf{r})$  is given by

$$V_{\text{KS}}(\mathbf{r}) = \int d\mathbf{r}' \frac{n(\mathbf{r}')}{|\mathbf{r} - \mathbf{r}'|} + V_{\text{xc}}(\mathbf{r}) + V_{\text{ext}}(\mathbf{r}) \quad (3.14)$$

and the exchange-correlation potential  $V_{\text{xc}}(\mathbf{r})$  is

$$V_{\text{xc}}(\mathbf{r}) = \frac{\delta E_{\text{xc}}[n]}{\delta n(\mathbf{r})} \quad (3.15)$$

To find the ground-state density  $n_0(\mathbf{r})$  for this non-interacting system we simply solve the one-electron Schrödinger equation with the electrons under the effect of an external potential  $V_{\text{KS}}(\mathbf{r})$ :

$$\left[ -\frac{1}{2}\nabla^2 + V_{\text{KS}}(\mathbf{r}) \right] \psi_i(\mathbf{r}) = \varepsilon_i \psi_i(\mathbf{r}) \quad (3.16)$$

for  $\frac{1}{2}N$  single-particle states  $|\psi_i\rangle$  with energies  $\varepsilon_i$ , constructing the density from

$$n(\mathbf{r}) = 2 \sum_{i=1}^{N/2} |\psi_i(\mathbf{r})|^2 \quad (3.17)$$

(the factor 2 is for spin degeneracy - we assume the orbitals are singly-occupied) and the non-interacting kinetic energy  $T_s[n]$  from

$$T_s[n] = - \sum_{i=1}^{N/2} \int d\mathbf{r} \psi_i^*(\mathbf{r}) \nabla^2 \psi_i(\mathbf{r}) \quad (3.18)$$

Since the potential  $V_{\text{KS}}(\mathbf{r})$  and density  $n(\mathbf{r})$  are interdependent in nature, the Kohn-Sham equations must be solved in self-consistent manner. With an assumed potential

from electron density, the electronic Schrödinger equation is solved which gives us a set of orbitals from which we can construct a new electron density. The process continues until convergence is achieved and we obtain the desired electron density for the ground state.

### 3.1.5 Exchange and Correlation Functional [86]

The density functional theory allows us to use the universal functional,  $F[n]$  which is independent of the system under consideration. Instead of dealing with a function of  $3N$  variables (the many-electron wave-function) we can work with the electron density function,  $n(\mathbf{r})$  which is a function of three variables only (3 spatial variables). Therefore, the overall complexity of the system is largely reduced and the complexity now becomes dependent on system size i.e. the number of interacting particles in the system,  $N$ . As a result, the quantum-mechanical calculations based on density-functional theory can in principle be performed with an effort which scales linearly with system-size.

The exact form of the universal functional  $F[n]$  (eqn. 3.9) is unknown. The Thomas-Fermi model [89][90] mentioned in 1927 was one of the earliest schemes of solving the many body problem. According to this model the total energy of the system can be expressed as [91]:

$$E^{TF}[n(\mathbf{r})] = \frac{3}{10}(3\pi^2)^{2/3} \int n(\mathbf{r})^{5/3} d\mathbf{r} + \int n(\mathbf{r})V_{ext}(\mathbf{r})d\mathbf{r} + \frac{1}{2} \int \int \frac{n(\mathbf{r})n(\mathbf{r}')}{|\mathbf{r} - \mathbf{r}'|} d\mathbf{r}d\mathbf{r}' \quad (3.19)$$

The first term is the kinetic energy parameter for the system with non-interacting electrons. The second term refers to the classical electrostatic attraction energy between electrons and nuclei. The third term refers to the Coulomb repulsion between the negatively charged electrons, also referred to as the Hartree energy [92].

This simplified model of calculating the total energy of a many particle system however suffers from many deficiencies. To accurately describe the behaviour of an interacting system like the electron gas, the effects of exchange and correlation must be accurately explained. In a non-interacting system, particles can be considered to be spatially separated. In an interacting system such as the electron gas, the interaction energy will be reduced by the correlation between the particles. Besides, the electrons will also constantly repel each other which would eventually lower the overall system energy. Thus it is impossible to treat the electrons as independent particles. These effects are completely neglected by the Thomas-Fermi model, and must in part account for its failure, the other source of error being the local approximation for the kinetic energy.

### 3.1.6 Local Density Approximation [86]

Although the correct nature and expression of exchange-correlation energy is difficult to extract, it is possible to make simple approximations for the exchange-correlation energy which work extremely well. The local density approximation (LDA), is one of the simplest approximations adopted.

In the LDA, the exchange-correlation energy is approximated from the homogeneous electron gas system. According to [86], here, the contribution to the exchange-correlation energy from any infinitesimal volume in space,  $d\mathbf{r}$ , is taken to be same if the whole of space were filled with a homogeneous electron gas with the same density as is found in  $d\mathbf{r}$  i.e.

$$E_{XC}[n] = \int d\mathbf{r} \epsilon_{XC}(n(\mathbf{r}))n(\mathbf{r}) \quad (3.20)$$

where  $\epsilon_{xc}(n(\mathbf{r}))$  is the exchange-correlation energy per electron in a homogeneous electron gas of density  $n(\mathbf{r})$ . The exchange-correlation potential  $V_{xc}(\mathbf{r})$  then takes the form

$$V_{XC}(\mathbf{r}) = \frac{\delta E_{XC}}{\delta n(\mathbf{r})} = \epsilon_{XC}(n(\mathbf{r})) + n(\mathbf{r}) \frac{d\epsilon_{XC}(n)}{dn} \Big|_{n=n(\mathbf{r})} \quad (3.21)$$

The exchange-correlation energy can be decomposed into exchange and correlation terms linearly,  $E_{XC} = E_X + E_C$ , so that separate expressions for  $E_X$  and  $E_C$  are sought. The exchange term takes on a simple analytic form for the homogeneous electron gas. Only limiting expressions for the correlation density are known exactly, leading to numerous different approximations for  $E_C$ .

### 3.1.7 Generalized Gradient Approximation

As the LDA approximates the energy of the true density by the energy of a local constant density, it fails in situations where the density undergoes rapid changes such as in molecules [92]. An improvement to this can be made by considering the gradient of the electron density, the so-called Generalized Gradient Approximation (GGA)[93] [94]. Symbolically this can be written as

$$E_{XC}^{GGA}[n] = \int \epsilon_{XC}(n, \nabla n)n(\mathbf{r})d^3\mathbf{r} \quad (3.22)$$

### 3.1.8 The Pseudopotential Approximation

The pseudopotential approach allows simplification of complex atomic system by using an effective or pseudopotential function. In atomic structure formation, the core electrons are relatively unaffected by the chemical environment of an atom. Therefore when atoms are brought together to form molecules or solids, their contribution to the total binding energy does not change. The actual energy differences of interest are the changes in valence electron energies. This motivation that, the physical properties are mostly affected by the valence electrons allows the use of pseudopotential approximation. Besides, the strong nuclear Coulomb potential and highly localised core electron wave-functions are difficult to represent computationally.

We obtain atomic wave functions by solving the atomic Hamiltonian and therefore the eigenstates or the wavefunctions must be mutually orthogonal. The core states in an atom are localised in the vicinity of the nucleus. Therefore, to ensure orthogonality, the valence states must oscillate rapidly in the core region. Therefore, valence electrons in the core region would have large kinetic energy which roughly cancels the large potential energy due to the strong Coulomb force. Thus the valence electrons are much more weakly bound than the core electrons [86].

Therefore, in order to obtain computational convenience, we can replace the strong Coulomb potential at the core electrons by a weaker one and the rapidly oscillating valence wave functions at the core region can be replaced by smoothly varying pseudo-wave functions [86].

Norm-conserving and ultrasoft are the two most common forms of pseudopotential used in modern plane-wave electronic structure codes. They allow a basis-set with a significantly lower cut-off (the frequency of the highest Fourier mode) to be used to describe the electron wavefunctions and so allow proper numerical convergence with reasonable computing resources. Norm-conserving pseudopotential was first proposed by Hamann, Schlüter, and Chiang (HSC) in 1979 [95]. The original HSC norm-conserving pseudopotential takes the following form:

$$\hat{V}_{ps}(r) = \sum_l \sum_m |Y_{lm}\rangle V_{lm}(r) \langle Y_{lm}| \quad (3.23)$$

Norm-conserving pseudopotentials are constructed to enforce two conditions:

- Inside the cut-off radius  $r_c$ , the norm of each pseudo-wavefunction be identical to its corresponding all-electron wavefunction.

- All-electron and pseudo wavefunctions are identical outside cut-off radius  $r_c$ .

## 3.2 Computational Details of Electronic Structure Calculation

### 3.2.1 MoS<sub>2</sub>/MX<sub>2</sub>/MoS<sub>2</sub> Trilayer System Under Study

In this work, we have considered three different trilayer systems for atomistic simulation using first principle method. The top and bottom TMDC layer is always MoS<sub>2</sub>. However, the middle TMDC layer is composed of three different monolayers: MoSe<sub>2</sub> or, WS<sub>2</sub> or, WSe<sub>2</sub>. We have also considered three different stacking configurations for each trilayer system under study. The trilayer systems are shown in fig. 3.1. As can be seen from the figure, the stacking configurations can be described as:

- AAA stacking- The transition metal atoms (Mo & W) are situated along a vertical line. The chalcogen atoms are also placed along a vertical line.
- ABA stacking- In this case, the middle TMDC layer just gets shifted with respect to the top and bottom TMDC layers. Here, the transition atoms in the middle layer are placed along a straight line with the chalcogen atoms of the top and bottom layers. On the other hand, the chalcogen atoms in the middle layer are placed along a linear alignment with the transition metal atoms of the top and bottom layer.
- ACA stacking- In ACA stacking, the middle TMDC layer will be shifted as well. However, in this case, the transition metal atoms will be situated along a straight line with the chalcogen atoms of the top and bottom layers. However, the chalcogen atoms will not follow the linear arrangement with the transition metal atoms of the top and bottom layers as followed in the ABA stacking.

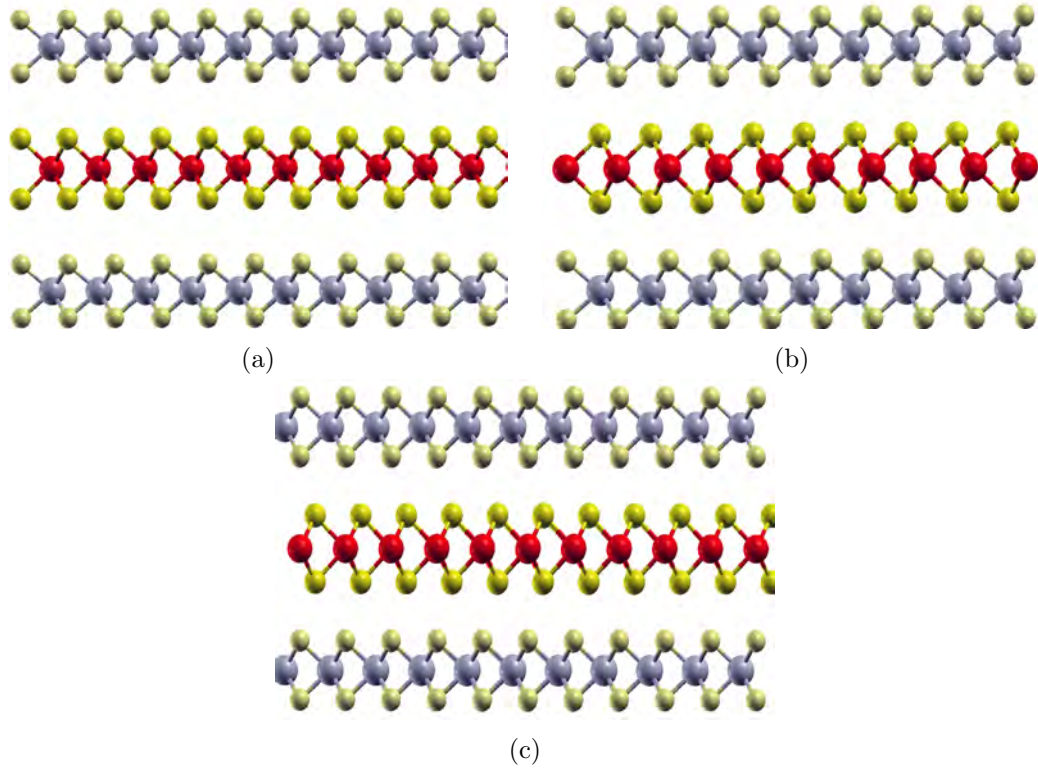


Figure 3.1: Stacking configurations used in this study- (a) AAA; (b) ABA; (c) ACA. Here, top and bottom layers are composed of  $\text{MoS}_2$ . The middle layer is composed of  $\text{MoSe}_2$  or,  $\text{WS}_2$  or,  $\text{WSe}_2$ . Different atoms of transition metals and chalcogens are shown in colors. The arrow in the figure shows interlayer distance between the two neighboring layers

### 3.2.2 Simulation Process Using Quantum Espresso

The first principle study was carried out using open source simulation package “Quantum Espresso” [96]. After geometry optimization of the trilayer structure, ground state energy of the relaxed structure was calculated and band structure calculation was performed. We performed study on three different stacking combinations of  $\text{MoS}_2/\text{MX}_2/\text{MoS}_2$  ( $\text{M}=\text{W}/\text{Mo}$ ;  $\text{X}=\text{S}/\text{Se}$ ) trilayer heterostructures. The simulation methodology started with a geometry optimization of the trilayer lattice structure and then performing a self-consistent field (scf) calculation for bandstructure extraction. For structural optimization, plane wave basis set with cut off energy 80 Ry was used. In our calculation we have considered norm conserving pseudopotentials for all the atoms with Perdew-Burke-Ernzerhof (PBE) exchange-correlation functional [65] [97]. For structural optimization, we used  $18 \times 18 \times 1$  Monkhorst-Pack K point meshing for brillouin zone sampling [98]. The structural optimization was performed until the force on each atom was less than  $0.01 \text{ eV}/\text{\AA}$ . The self-consistent convergence threshold for energy was set at  $10^{-9}$  Ry. To avoid interaction between two adjacent images of the unit cell of the trilayer lattice, 30

Å distance was maintained between two adjacent images.

After optimization of lattice structure, for better accuracy, scf calculation was performed with brillouin zone sampling of 24x24x1 K points. The output of the scf calculation was used in the extraction of bandstructure. We used the bands.x package for the bandstructure extraction. Finally, we plotted the bandstructure along  $\Gamma$ - $M$ - $K$ - $\Gamma$  direction in the brillouin zone and observed the effect of strain and different lattice stacking configurations.

### 3.3 Ballistic Simulation of Double Gate MOSFET

#### 3.3.1 Device Description

For quantum ballistic simulation, we have used the device structure as shown in fig. 3.2 The device is double gate MOSFET with 10 nm gate length. 2 nm HfO<sub>2</sub> has been considered as the gate dielectric material at both sides of the channel. High-k oxides i.e. Al<sub>2</sub>O<sub>3</sub> and HfO<sub>2</sub> has been used as gate dielectrics in high performance TMDC FETs with promising results [44][73][99][41]. The source/drain extension region length has been considered to be 10 nm as well. The source/drain region has been considered to be semiconducting in nature and made of the same trilayer TMDC material as the channel. The doping density at source /drain region is considered as  $1 \times 10^{25} \text{ m}^{-3}$ . The channel on the other hand, has been considered undoped.

#### 3.3.2 Transport Simulation Using Fast Uncoupled Mode Space Approach

In this study, we have used effective mass Hamiltonian along with fast uncoupled mode space (FUMS) [100] [101] approach for transport analysis of the 10 nm double gate MOSFET. The process is a bit more simplified and computationally efficient. With proper choice of device parameters, this approach can match experimental results with reasonable accuracy [102] [103]. Therefore, we have opted for a simplified fast uncoupled mode space approach with effective mass Hamiltonian. We have implemented the simplified quantum transport simulator using self-consistent analysis incorporating NEGF formalism. The self-consistent simulation approach is implemented using COMSOL Multiphysics and MATLAB. The simulation approach has already been implemented for analysis of multigate planar [104] [100] and non-planar device architectures [105].



The self-consistent process begins by assuming an initial charge density profile. Then Poisson equation is solved in Finite Element Method (FEM) using COMSOL Multiphysics to extract the potential profile  $E_C(x,z)$  inside the device. To extract the subband profile and carrier density profile inside the device structure, solution of 2D Schrodinger equation is required. Application of mode space approach reduces this 2D problem into two separate one dimensional problems. In Uncoupled Mode Space (UMS) approach, Schrodinger equation must be solved at every slice of the device structure along gate confinement direction to obtain subband profile, which can be used to obtain the overall carrier density using NEGF formalism. However, a more efficient subband calculation is possible through the application of Fast Uncoupled Mode Space (FUMS) approach. In this approach, the wavefunction for a particular eigen energy is considered to be invariant in the channel along the transport direction (X direction in fig. 3.2). Which means, carrier wavefunctions and subband energies can be calculated by solving Schrodinger equation for a single 1D slice in the channel.

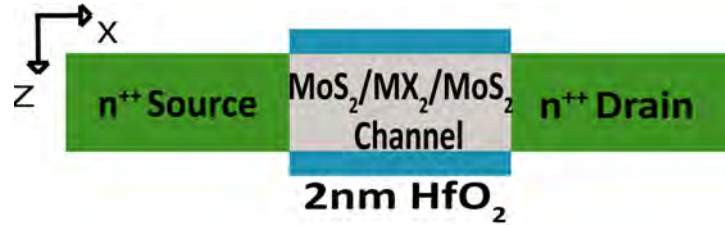


Figure 3.2: The double gate device used for ballistic simulation. 2 nm HfO<sub>2</sub> has been used as the gate dielectric material. Source and drain regions are both heavily doped. The channel material is MoS<sub>2</sub>/MX<sub>2</sub>/MoS<sub>2</sub> trilayer in AAA stacking configuration.

From the conduction band profile extracted using Poisson's equation, an average conduction band profile, is used to solve 1D Schrodinger equation along gate confinement direction eqn. 3.25.

$$\overline{E_C}(z) = \frac{1}{L_x} \int_0^{L_x} E_C(x, z) dx \quad (3.24)$$

$$\left[ -\frac{\hbar^2}{2} \frac{\partial}{\partial y} \left( \frac{1}{m_z^*} \frac{\partial}{\partial z} \right) + \overline{E_C}(z) \right] \overline{\psi_{sub}^m}(z) = \overline{E_{sub}^m} \cdot \overline{\psi_{sub}^m}(z) \quad (3.25)$$

Solving 1D Schrodinger equation gives us the average subband energy,  $\overline{E_{sub}^m}$  and wavefunction,  $\overline{\psi_{sub}^m}$  for the  $m^{th}$  subband. Using first order perturbation theory, the eigen energies in the channel is calculated as shown in eqn. 3.26. Then 1D Hamiltonian matrix is formed along the transport direction and the retarded Green's function,  $G(E)$  is formed (eqn. 3.27) [106].

$$E_{sub}^m(x) = \overline{E_{sub}^m} + \int_z E_C(x, z) |\overline{\psi_{sub}^m}(z)|^2 dz - \int_z \overline{E_C}(z) |\overline{\psi_{sub}^m}(z)|^2 dz \quad (3.26)$$

$$G(E) = [EI - H - \Sigma_S(E) - \Sigma_D(E)]^{-1} \quad (3.27)$$

Where,  $H$  refers to the device Hamiltonian formulated using the subband energy profiles in the channel.  $\Sigma_S(\Sigma_D)$  refers to self-energy matrices corresponding to the coupling between channel and source (drain) reservoirs. Self-energy matrices allow us to work within the simulation region presented in fig. 3.2 without including infinite reservoirs i.e. source and drain. The effect of infinite source and drain reservoirs are taken into account by self-energy matrices. From the self-energy matrices and retarded Green's function, the spectral density functions for source ( $A_S$ ) and drain ( $A_D$ ) contacts are calculated [106] [104]:

$$A_S = G\Gamma_S G^\dagger \quad \text{and} \quad A_D = G\Gamma_D G^\dagger \quad (3.28)$$

Here,  $\Gamma_S$  and  $\Gamma_D$  refers to the broadening matrices of source and drain contacts respectively [106], which are formulated as:

$$\Gamma_S = i(\Sigma_S - \Sigma_S^\dagger) \quad \text{and} \quad \Gamma_D = i(\Sigma_D - \Sigma_D^\dagger) \quad (3.29)$$

From spectral density function, 2-D carrier density for the  $m^{th}$  subband,  $n_{2D}^m$  in the channel, is calculated using eqn. 3.30

$$n_{2D}^m(E) = \frac{1}{\hbar a} \sqrt{\frac{m_y^* k_B T}{2\pi^3}} \int_{-\infty}^{\infty} (A_S^m \mathfrak{S}_{-1/2}(E, \mu_S) + A_D^m \mathfrak{S}_{-1/2}(E, \mu_D)) dE \quad (3.30)$$

Where,  $a$  refers to the grid spacing in the channel direction (X direction). Afterwards, 3-D carrier density for the  $m^{th}$  subband is calculated from 2-D carrier density and average carrier wavefunction using the following equation:

$$n_{3D}^m(x, z) = n_{1D}^m(x) |\overline{\psi^m}(z)|^2 \quad (3.31)$$

The calculated carrier density is fed back into Poisson's equation to solve and extract the new potential profile. Then using an update co-efficient, potential profile is updated

and the updated potential profile is used for further calculation in self-consistent procedure. Once self-consistency is achieved, current for a subband is calculated using NEGF formalism using the following equations:

$$I_{DS}^m(E) = \frac{q}{\hbar^2} \sqrt{\frac{m_y^* k_B T}{2\pi^3}} T^m(E) [\mathfrak{S}_{-1/2}(E, \mu_S) - \mathfrak{S}_{-1/2}(E, \mu_D)] \quad (3.32)$$

$$T^m(E) = \text{Trace}(\Gamma_S(E)G^m(E)\Gamma_D(E)G^{m\dagger}(E)) \quad (3.33)$$

Here,  $T^m(E)$  is the transmission probability calculated using eqn. 3.33 for  $m^{\text{th}}$  subband.

The physics of interband tunneling has been exploited in MOSFETs to design low power switching devices. In MOSFETs, although carrier transport takes place over the potential barrier at the source-channel junction, interband tunneling could still affect device performance in the sub-threshold regime when carrier effective mass and bandgap get lowered in the channel. In this study, we have incorporated the effect of interband tunneling using the formulation depicted in [107].

## Chapter 4

# Results and Discussion

In this chapter, we will discuss the results obtained from first principle simulation of the trilayer  $\text{MoS}_2/\text{MX}_2/\text{MoS}_2$  heterostructure. We will mainly concentrate on the atomic structure and electronic properties of the trilayer system. In the later part, we will use the results obtained from atomistic simulation in the simulation of a simple double gate MOSFET with 10 nm gate length and try to explore the potential of these trilayers as channel materials in ultra-scaled transistors.

### 4.1 Lattice Structure of Trilayer $\text{MoS}_2$ Heterostructure

As mentioned earlier, the optimization was performed self-consistently using Quantum Espresso simulation package. The optimization was performed by varying both lattice parameter and interlayer distance. After optimization had been achieved, we extracted bond length between transition metal atom and chalcogen atom, bond angle and interlayer distance of the optimized lattice. The results obtained from the optimization is reported below for all three stacking configuration of the trilayer heterostructure in table 4.1 to 4.3.

As seen from the extracted information given in table 4.1 to 4.3, the interlayer distance is higher for AAA stacking in all three material systems. This can be attributed to the linear vertical alignment of atoms in AAA stacking that increases interaction between the atoms. When the stacking is changed to ABA or ACA condition, the interlayer distance decreases. The extracted interlayer distance obtained from first principle simulation of AAA stacking closely matches with the results reported in [66] for bilayer structures in AA (linear vertical alignment of transition metal and chalcogen atoms in both layers) configuration. The interlayer separation of ABA and ACA stacking configuration of

different trilayers are reported in [67]. Our results for ABA and ACA stacking also closely matches with the values reported in [67] for interlayer separation which supports the validation of atomic structure simulation . We have also extracted lattice constant values for the trilayer heterostructures. The lattice constant values are reported in table 4.1 to 4.3. These lattice constant values also closely match with the results reported in [67].

**Table 4.1: Optimized Lattice Parameters Obtained Using First Principle Simulation of  $\text{MoS}_2/\text{MoSe}_2/\text{MoS}_2$  at Different Stacking Configuration**

Parameters		AAA	ABA	ACA
Lattice Constant ( $\text{\AA}$ )		3.239	3.24	3.238
Bond Length ( $\text{\AA}$ )	Mo-S	2.4231	2.4272	2.4242
	Mo-Se	2.5242	2.5241	2.5241
Atomic Distance, ( $\text{\AA}$ )	S-Se	3.7527	3.15254	3.1524
	S-S	3.0831	3.08268	3.08231
	Se-Se	3.3911	3.39073	3.3904
Bond Angle (degrees)	S-Mo-S	79.2	78.996	79.002
	Se-Mo-Se	84.398	84.39	84.386

**Table 4.2: Optimized Lattice Parameters Obtained Using First Principle Simulation of  $\text{MoS}_2/\text{WS}_2/\text{MoS}_2$  at Different Stacking Configuration**

Parameters		AAA	ABA	ACA
Lattice Constant ( $\text{\AA}$ )		3.186	3.183	3.186
Bond Length ( $\text{\AA}$ )	Mo-S	2.4109	2.41087	2.412
	W-S	2.4419	2.4417	2.44284
Atomic Distance, ( $\text{\AA}$ )	S-S <sup>+</sup>	3.6897	3.07983	3.17583
	S-S	3.11672	3.1161	3.11751
	S-S*	3.21064	3.20974	3.21347
Bond Angle (degrees)	S-Mo-S	80.525	80.514	80.539
	S-W-S	82.207	82.191	82.251

- S – S\* indicates the atomic S-S distance in the middle  $\text{WS}_2$  layer.
- S – S<sup>+</sup> indicates the distance between  $\text{MoS}_2$  and  $\text{WS}_2$  monolayer.

**Table 4.3: Optimized Lattice Parameters Obtained Using First Principle Simulation of MoS<sub>2</sub>/WSe<sub>2</sub>/MoS<sub>2</sub> at Different Stacking Configuration**

Parameters		AAA	ABA	ACA
Lattice Constant (Å)		3.241	3.237	3.243
Bond Length (Å)	Mo-S	2.42396	2.4235	2.4243
	W-Se	2.5522	2.55038	2.55236
Atomic Distance,(Å)	S-Se	3.7753	3.07998	3.17386
	S-S	3.0838	3.0812	3.0839
	Se-Se	3.4739	3.46922	3.47395
Bond Angle (degrees)	S-Mo-S	79.014	78.975	79.017
	Se-W-Se	85.774	85.684	85.776

## 4.2 Electronic Properties of the Trilayer

### 4.2.1 Bandstructure and Density of States of the Relaxed Trilayer Heterostructure

After geometry optimization, we performed scf calculation on the trilayer heterostructure to determine the electronic states and bandstructure. We extracted the bandstructure along  $\Gamma$ -M-K- $\Gamma$  direction in the first Brillouin zone. The extracted bandstructure also shows interesting characteristics. At first, we would discuss bandstructure of the relaxed trilayer lattice at three different stacking configurations. In all these cases, we have considered the valance band maxima to be at 0 eV i.e valance band maxima as the reference. In our study, we have not considered the effect of spin-orbit coupling.

For MoS<sub>2</sub>/MoSe<sub>2</sub>/MoS<sub>2</sub> trilayer at AAA stacking configuration, the bandgap was found to be 0.707 eV which was direct in nature. For the other two stacking configurations- ABA and ACA, the bandgaps were indirect in nature with values 0.729 eV and 0.752 eV respectively. There lies very little energy difference between valance band positions at  $\Gamma$  point and K point for ABA and ACA stacking. The extracted bandgaps closely match with the values reported in [67]. For the indirect bandgap materials, the valance band maxima was found to be at  $\Gamma$  point and the conduction band minima was found to be at K point. Here, the extracted bandgaps are slightly lower than the values reported for bilayer MoS<sub>2</sub>/MoSe<sub>2</sub> heterostructures. The extracted bandgaps from the simulation are shown in fig. 4.1.

When a WS<sub>2</sub> monolayer is inserted between two MoS<sub>2</sub> monolayers, we have found the bandgap to be indirect in nature. The bandgap appears to be highest for MoS<sub>2</sub>/WS<sub>2</sub>/MoS<sub>2</sub> trilayer heterostructure. In all these cases, the conduction band minima was found at K point and the valance band maxima was found at  $\Gamma$  point. The trilayers showed maximum bandgap under AAA stacking configuration. The extracted bandgap values appear

to be slightly higher than the values reported in [67] for both ABA and ACA stacking. The extracted bandgaps are shown in fig. 4.2. However, in this case, the valance band maxima at  $\Gamma$  point can be clearly separated from the valance band position at K point i.e. the energy separation is higher than MoS<sub>2</sub>/MoSe<sub>2</sub>/MoS<sub>2</sub> trilayer.

Extracted bandstructures of MoS<sub>2</sub>/WSe<sub>2</sub>/MoS<sub>2</sub> trilayers at different stacking configurations are shown in fig. 4.3. These trilayers provide the lowest bandgaps of the material systems studied in this work. The bandgap appears to be always direct at all stacking configurations. The valance band maxima at K point can be clearly identified in this case as well. The direct band gap nature can be attributed to S/Se-interface present in the lattice structure [67]. Recent literature also reports MoS<sub>2</sub>/WSe<sub>2</sub> bilayer heterostructure to be direct bandgap material. However, the bandgap of the trilayer heterostructure is lower than the values obtained for the bilayer heterostructure. The values obtained from our calculation is slightly higher than the values reported in [67]. Energy separation between different symmetry points at the valance band and the conduction band of the trilayer heterostructure for different stacking configuration is reported in table 4.4.

**Table 4.4: Energy Separation Between Symmetry Points in the First Brillouin Zone**

Material	Stacking	Energy separation between K and $\Delta$ point in conduction band (eV)	Energy separation between K and $\Gamma$ point in valance band (eV)
MoS <sub>2</sub> /MoSe <sub>2</sub> /MoS <sub>2</sub>	AAA	0.445	0.236
	ABA	0.352	0.046
	ACA	0.372	0.064
MoS <sub>2</sub> /WS <sub>2</sub> /MoS <sub>2</sub>	AAA	0.192	0.082
	ABA	0.117	0.309
	ACA	0.14	0.284
MoS <sub>2</sub> /WSe <sub>2</sub> /MoS <sub>2</sub>	AAA	0.484	0.457
	ABA	0.389	0.123
	ACA	0.42	0.177

We have also extracted the projected density of states characteristics of the trilayer heterostructure. Projected density of states profile can be used to get an idea of the contribution of different atomic states on the electronic properties of the trilayer heterostructure and deeply understand the nature of the bandgap. For the study of the projected density of states characteristics, we have only considered d orbitals of transition metal atoms and p orbitals of chalcogen atoms.

Fig. 4.4 to fig. 4.6 show the projected density of states profiles along with extracted bandstructure of MoS<sub>2</sub>/MoSe<sub>2</sub>/MoS<sub>2</sub> trilayer for all three stacking configurations under relaxed condition. As can be seen from the figure, at the top of the valance band, the states are mainly contributed by the middle MoSe<sub>2</sub> layer. On the other hand, states at



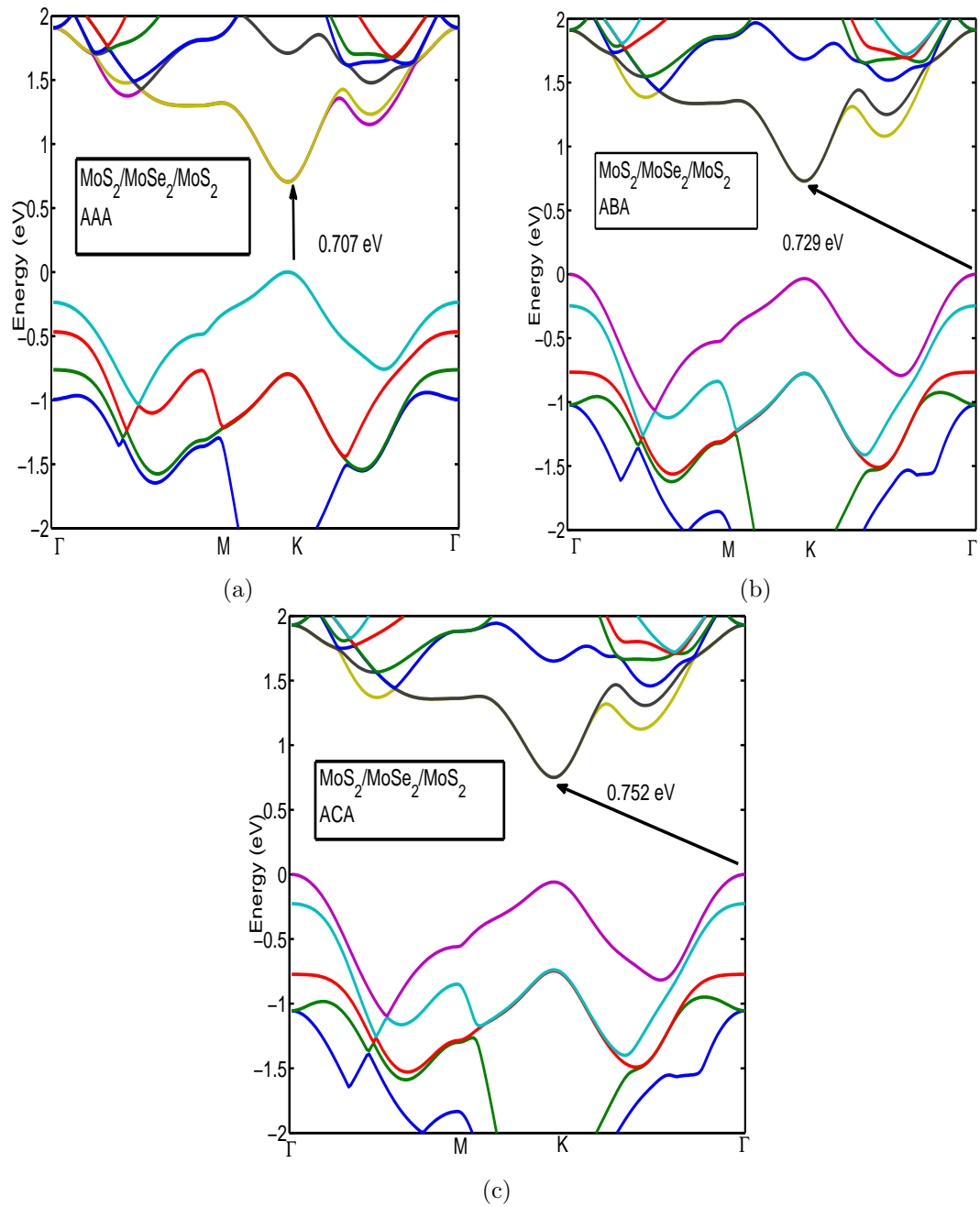


Figure 4.1: Extracted bandstructures of relaxed  $\text{MoS}_2/\text{MoSe}_2/\text{MoS}_2$  trilayer heterostructure at: (a) AAA, (b) ABA, (c) ACA stacking configurations

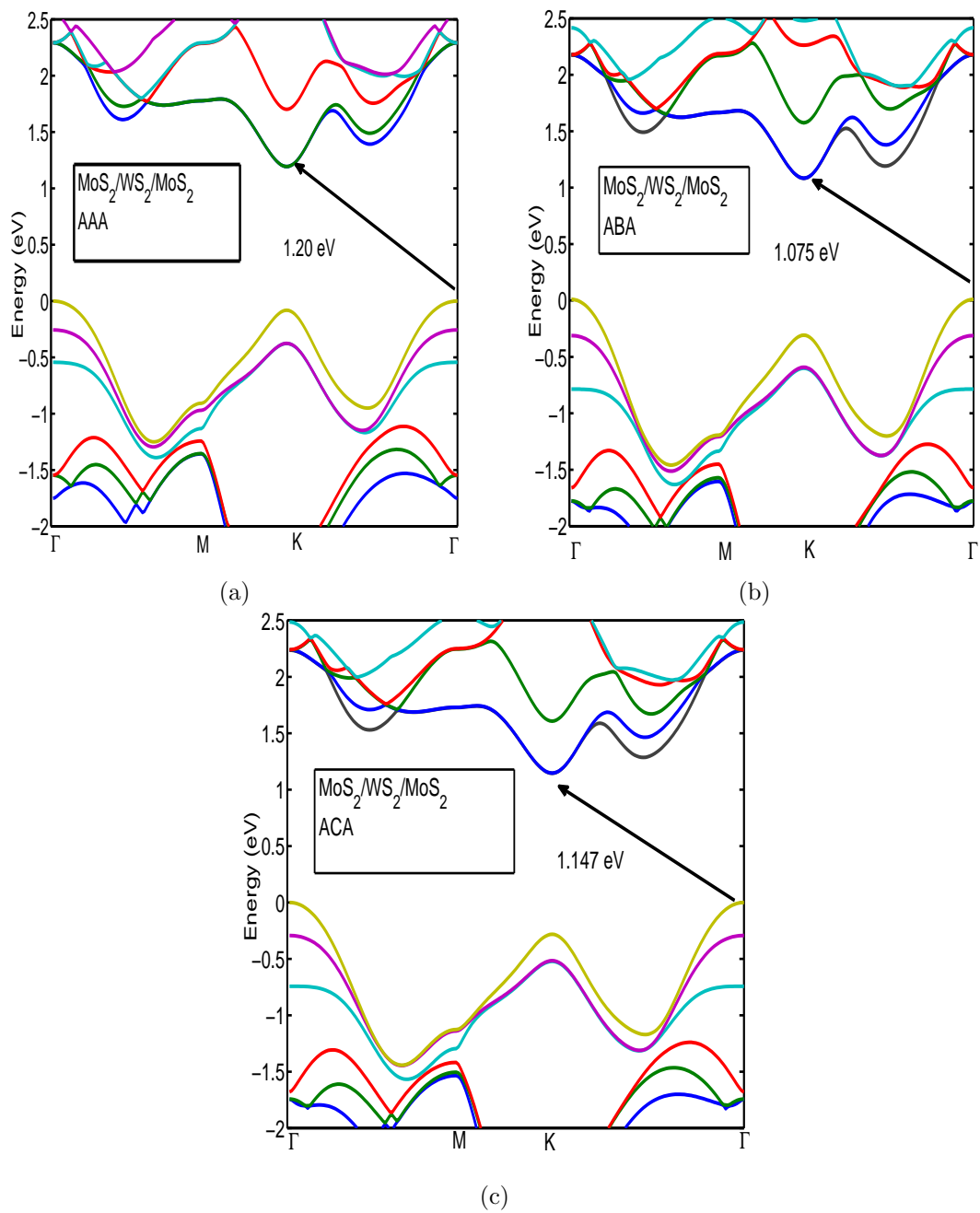


Figure 4.2: Extracted bandstructures of relaxed  $\text{MoS}_2/\text{WS}_2/\text{MoS}_2$  trilayer heterostructure at: (a) AAA, (b) ABA, (c) ACA stacking configurations

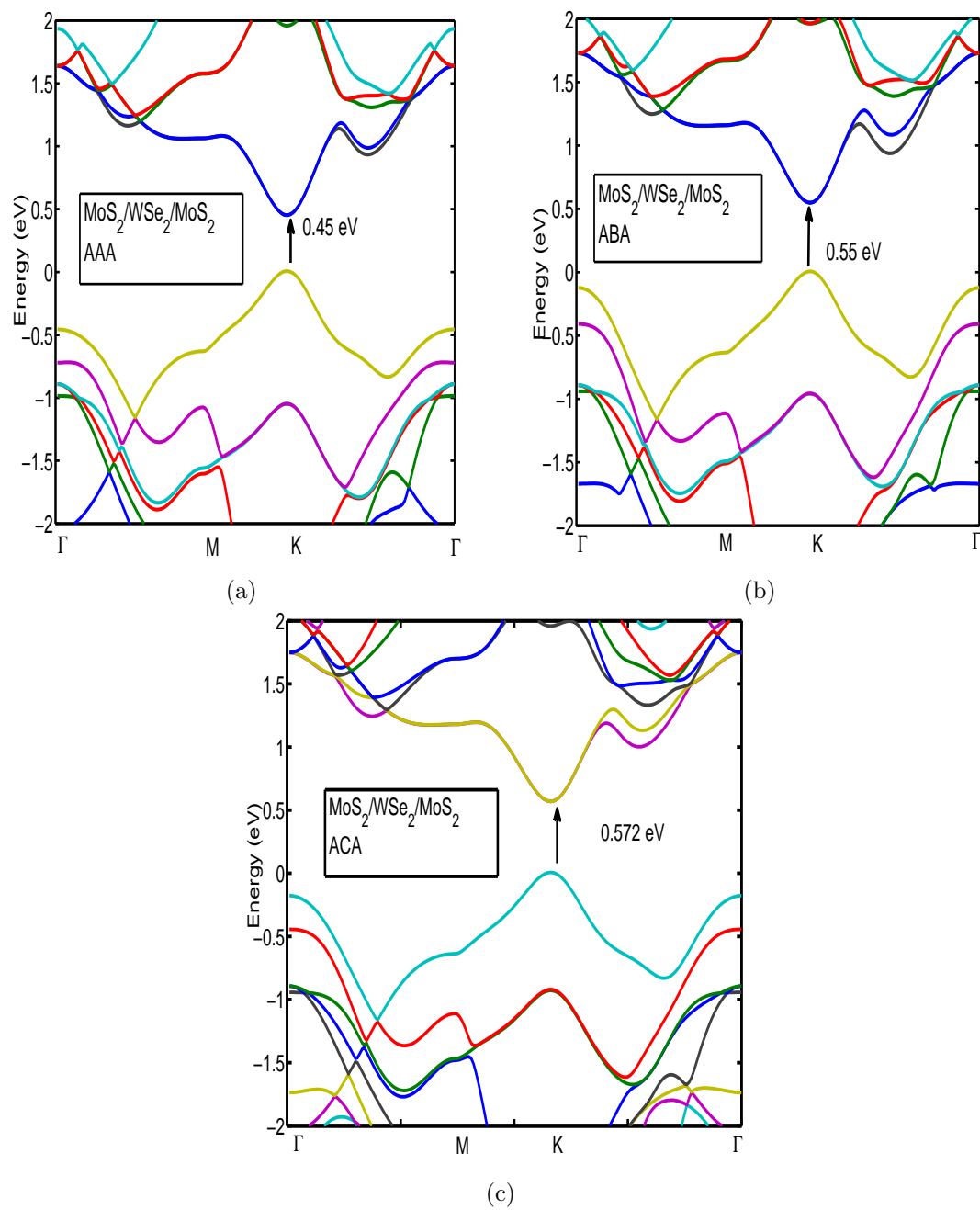


Figure 4.3: Extracted bandstructures of relaxed  $\text{MoS}_2/\text{WSe}_2/\text{MoS}_2$  trilayer heterostructure at: (a) AAA, (b) ABA, (c) ACA stacking configurations

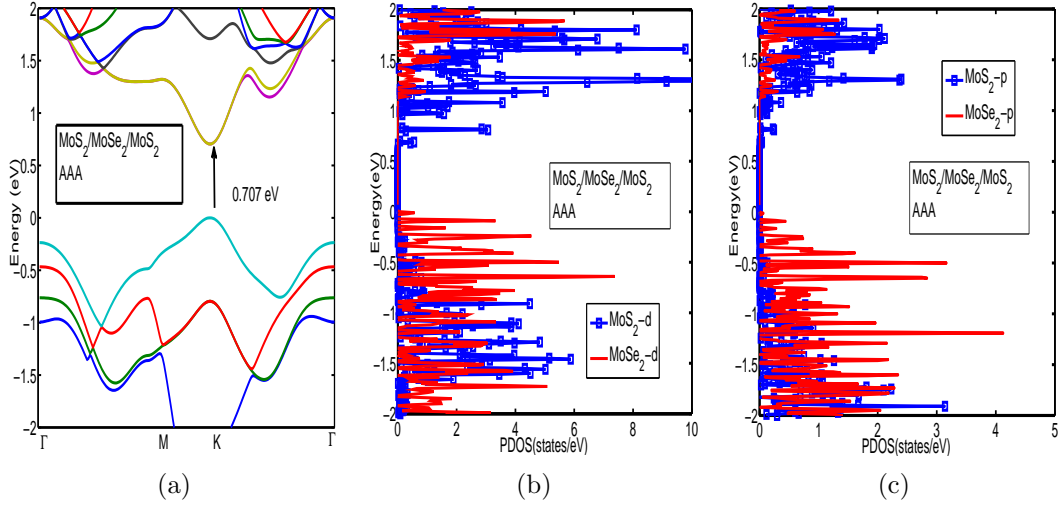


Figure 4.4: (a) Extracted bandstructure for MoS<sub>2</sub>/MoSe<sub>2</sub>/MoS<sub>2</sub> trilayer at AAA stacking; (b) PDOS profile for transition metal atoms; (c) PDOS profile for chalcogen atoms.

the bottom of the conduction band are mainly contributed by MoS<sub>2</sub> monolayers. This separation like the behaviour of electron and hole states was also observed and reported for bilayer MoS<sub>2</sub>/MoSe<sub>2</sub> heterostructures [66].

Fig. 4.7 to fig. 4.9 shows the projected density of states profile for MoS<sub>2</sub>/WS<sub>2</sub>/MoS<sub>2</sub> trilayer for all three stacking conditions. We also observe similar characteristics like before in this trilayer. The valance band states at maxima are mostly contributed by the middle WS<sub>2</sub> layer whereas the conduction band states at minima are contributed by the MoS<sub>2</sub> layers on the side.

Fig. 4.10 to fig. 4.12 shows the projected density of states of MoS<sub>2</sub>/WSe<sub>2</sub>/MoS<sub>2</sub> trilayer heterostructure for three different stacking configurations under relaxed condition. The projected density of states profile also shows same characteristics as shown by the previous trilayers. Here, conduction and valance and states are separated and contributed by two different TMDC layers as well. Similar nature of conduction and valance band states of TMDC trilayer heterostructures has also been reported in [67].

#### 4.2.2 Electronic Properties of Strained Trilayer Heterostructure

We have also investigated the effect of bi-axial strain on the electronic properties of the trilayer heterostructures. The bi-axial strain was applied to all the configurations to observe how the electronic structure and hence the material electronic properties vary with strain. In this study, the bi-axial strain is applied by stretching and compressing the lattice bi-axially and the strain is formulated as  $st = \frac{a-a_0}{a_0}$ . Here  $a$  refers to the lattice constant of the strained lattice,  $a_0$  is the lattice constant of the unstrained lattice.

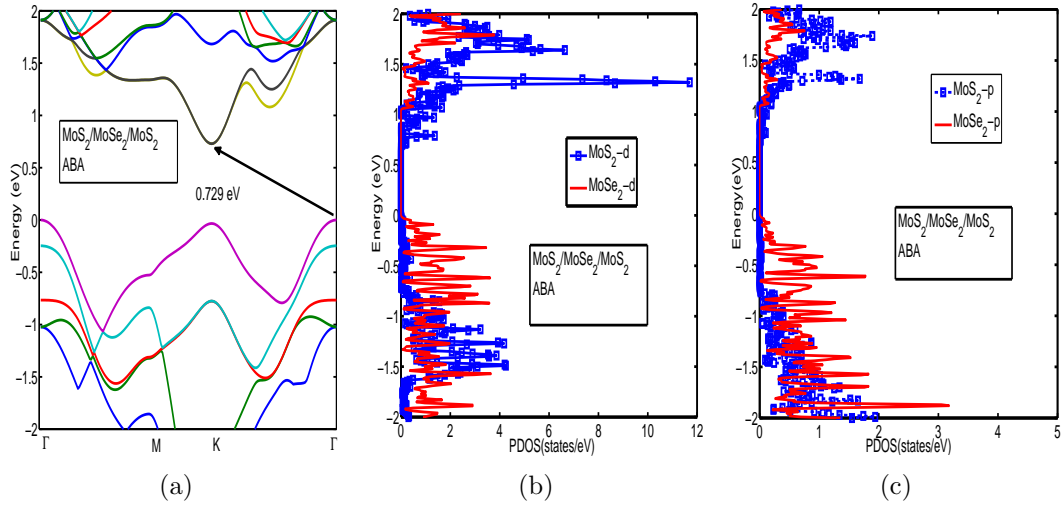


Figure 4.5: (a) Extracted bandstructure for  $\text{MoS}_2/\text{MoSe}_2/\text{MoS}_2$  trilayer at ABA Stacking; (b) PDOS profile for transition metal atoms; (c) PDOS profile for chalcogen atoms.

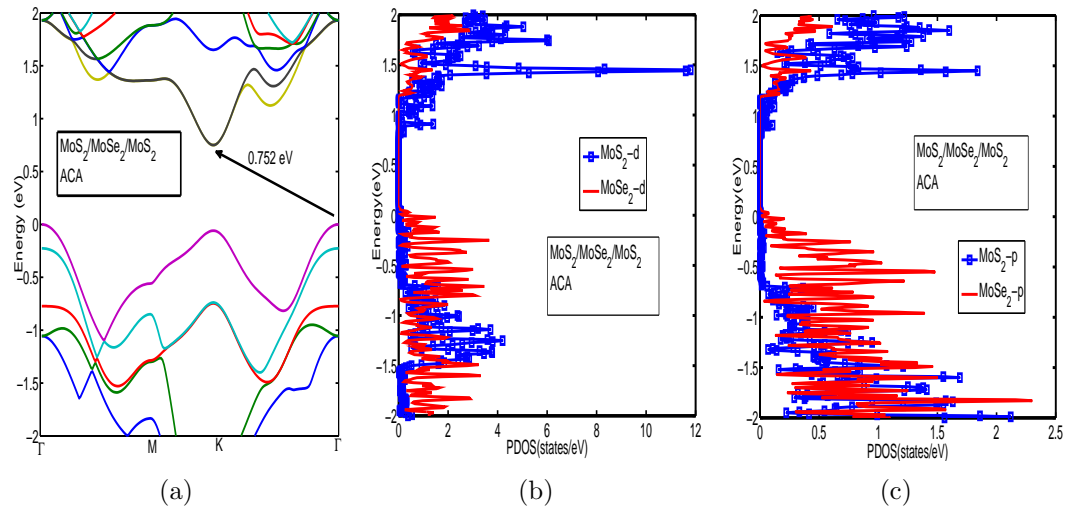


Figure 4.6: (a) Extracted bandstructure for  $\text{MoS}_2/\text{MoSe}_2/\text{MoS}_2$  trilayer at ACA Stacking; (b) PDOS profile for transition metal atoms; (c) PDOS profile for chalcogen atoms.

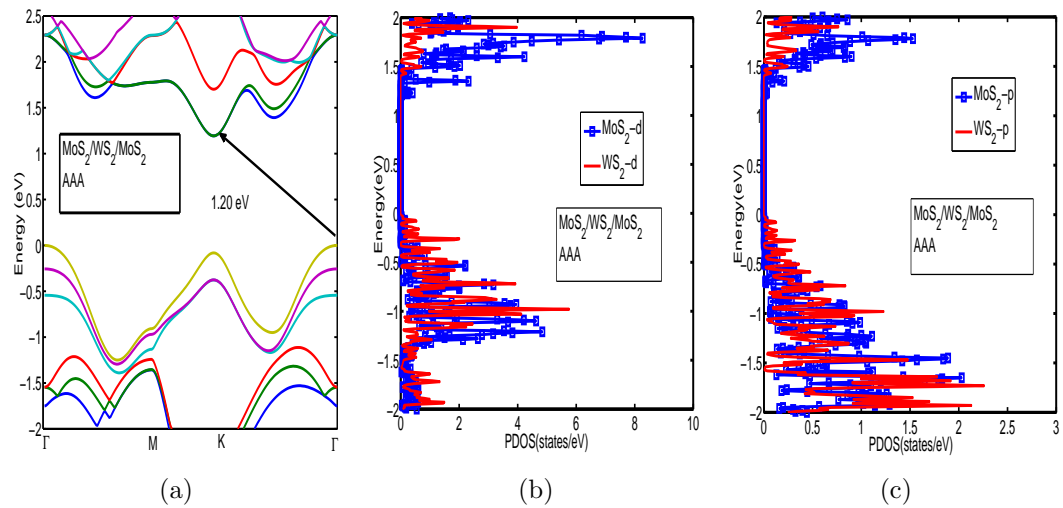


Figure 4.7: (a) Extracted bandstructure for  $\text{MoS}_2/\text{WS}_2/\text{MoS}_2$  trilayer at AAA Stacking; (b) PDOS profile for transition metal atoms; (c) PDOS profile for chalcogen atoms.

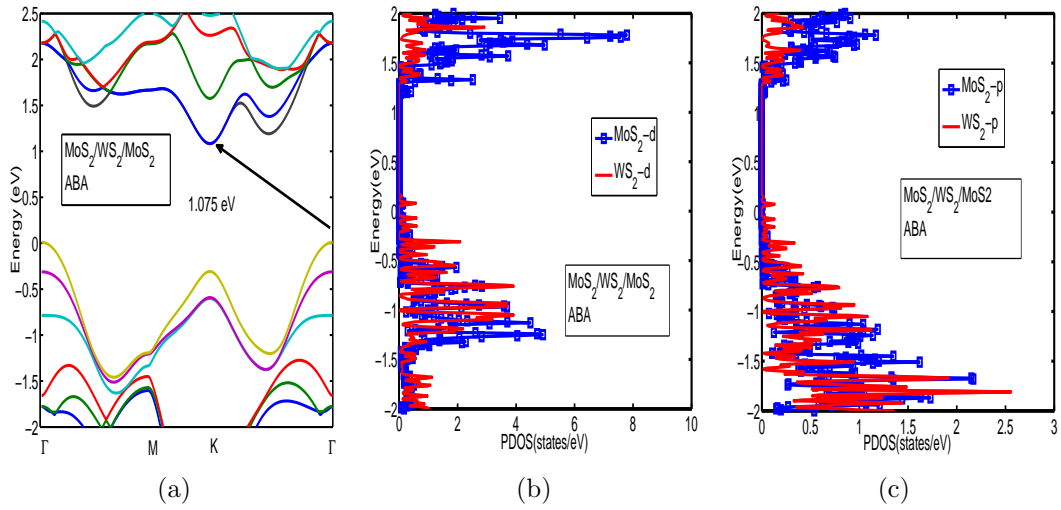


Figure 4.8: (a) Extracted bandstructure for MoS<sub>2</sub>/WS<sub>2</sub>/MoS<sub>2</sub> trilayer at ABA Stacking; (b) PDOS profile for transition metal atoms; (c) PDOS profile for chalcogen atoms.

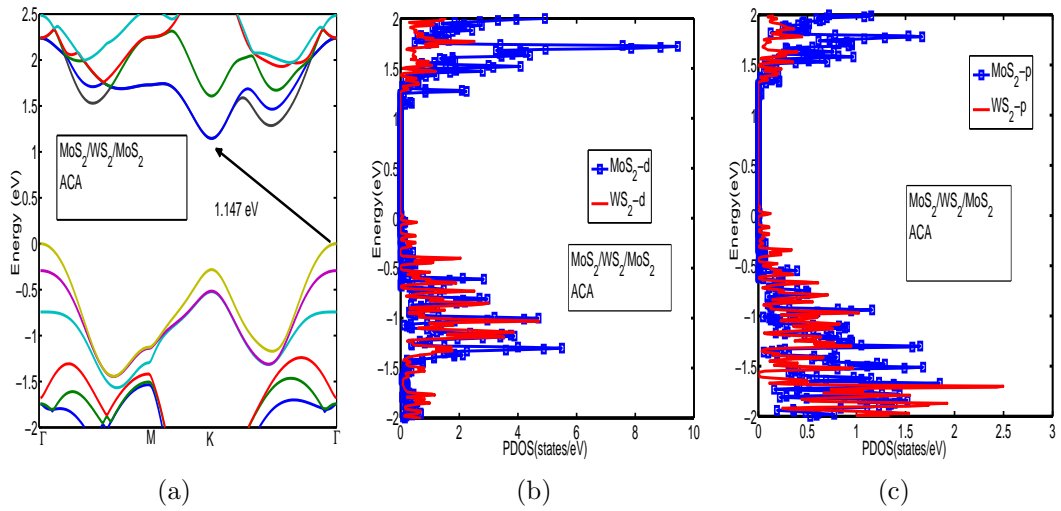


Figure 4.9: (a) Extracted bandstructure for MoS<sub>2</sub>/WS<sub>2</sub>/MoS<sub>2</sub> trilayer at ACA Stacking; (b) PDOS profile for transition metal atoms; (c) PDOS profile for chalcogen atoms.

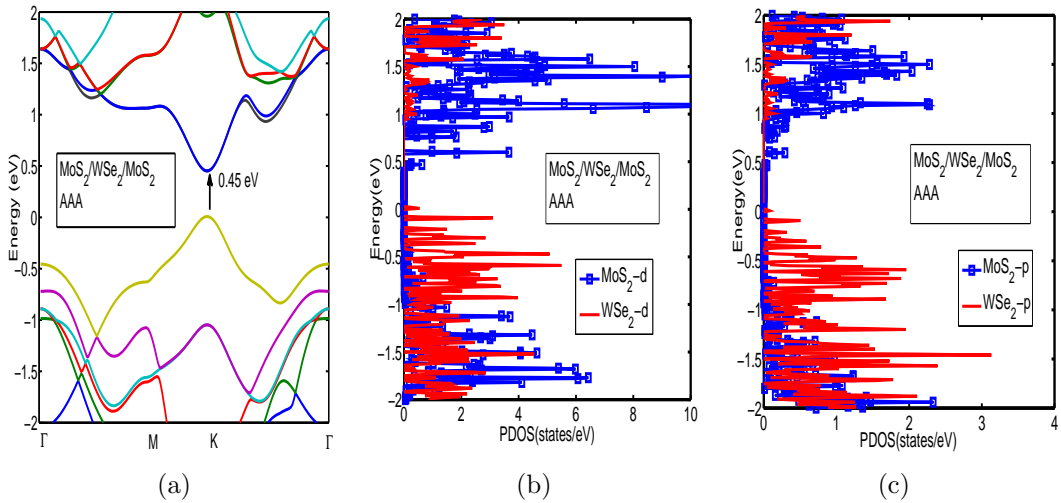


Figure 4.10: (a) Extracted bandstructure for MoS<sub>2</sub>/WSe<sub>2</sub>/MoS<sub>2</sub> trilayer at AAA Stacking; (b) PDOS profile for transition metal atoms; (c) PDOS profile for chalcogen atoms.

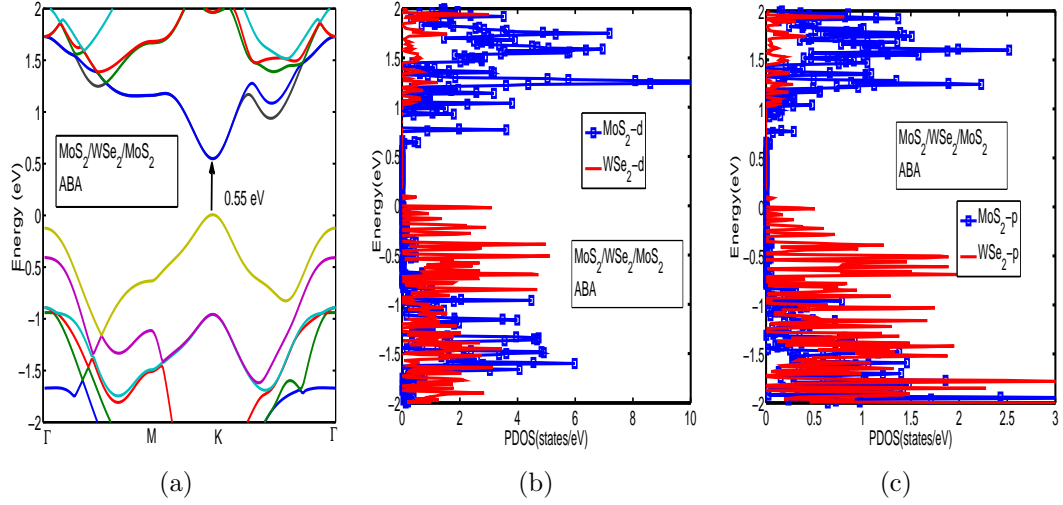


Figure 4.11: (a) Extracted bandstructure for MoS<sub>2</sub>/WSe<sub>2</sub>/MoS<sub>2</sub> trilayer at ABA Stacking; (b) PDOS profile for transition metal atoms; (c) PDOS profile for chalcogen atoms.

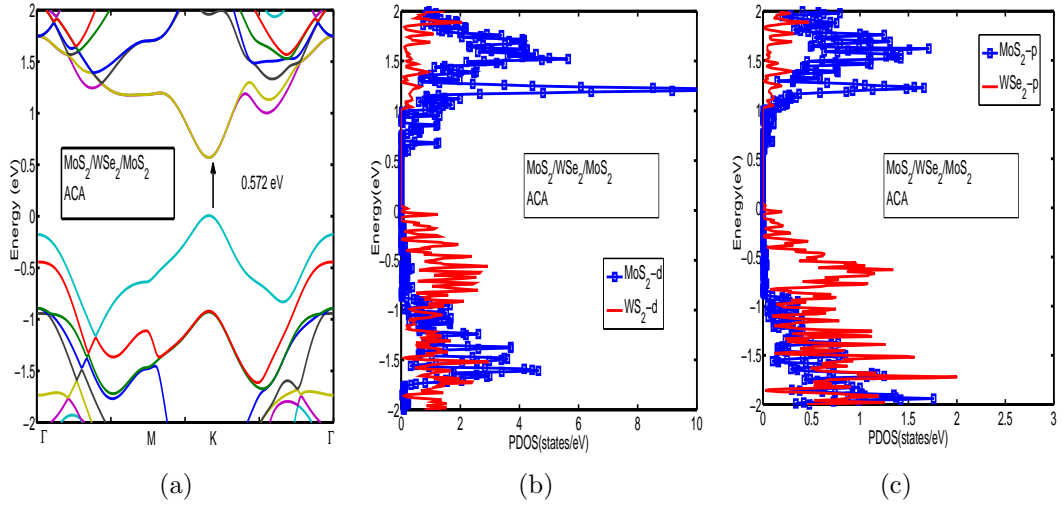


Figure 4.12: (a) Extracted bandstructure for MoS<sub>2</sub>/WSe<sub>2</sub>/MoS<sub>2</sub> trilayer at ACA Stacking; (b) PDOS profile for transition metal atoms; (c) PDOS profile for chalcogen atoms.

For MoS<sub>2</sub>/MoSe<sub>2</sub>/MoS<sub>2</sub> trilayers, under compressive strain, valence band maxima appears at K point in the first Brillouin zone. On the other hand, conduction band minima occurs at  $\Delta$  point (at a point between K and  $\Gamma$  point) and therefore, the nature of the bandgap is indirect. However, as we move from compressive to tensile strain, the valence band energy at K point decreases and energy at  $\Gamma$  point gradually increases. On the other hand, conduction band minima shifts from  $\Delta$  point to K point in the Brillouin zone. Therefore, for a certain region of applied strain, the AAA stacking shows direct bandgap nature as observed from our simulation results. In the case of ABA and ACA stacking, valence band maxima in compressively strained lattice appeared at K point and conduction band minima occurred at  $\Delta$  point. However, as mentioned earlier, under relaxed condition, these two lattices had shown indirect bandgap nature with very little energy separation between the valence band symmetry points at K and  $\Delta$ . As



we move to tensile strain regime, we see that the valance band maxima and conduction band minima stay at  $\Gamma$  point and K point respectively and the bandstructure of trilayer lattice preserves its indirect bandgap nature. Here, the energy separation between the valance band symmetry points at  $\Gamma$  and K increases with increased tensile strain. The extracted bandstructures are shown in fig. 4.13 to fig. 4.15.

As a  $\text{WS}_2$  monolayer is inserted between two  $\text{MoS}_2$  monolayers at AAA stacking, the bandgap was found to be indirect in our study. Here, the conduction band minima appeared at K point and valance band maxima occurred at  $\Gamma$  point. Under compressive strain, the valance band maxima was found at K point and conduction band minima was found at  $\Delta$  point. As tensile strain was applied, the valance band position at  $\Gamma$  point increased in energy and conduction band minima moved to K point. Therefore the lattice showed indirect bandgap nature as both compressive and tensile strain were applied. However, for ABA and ACA stacking configurations, the bandgap always showed indirect nature for our region of strain application. The valance band maxima always appeared at  $\Gamma$  point and the conduction band maxima moved from  $\Delta$  point to K point in both ABA and ACA stacking configurations. The extracted bandstructures are shown in fig. 4.16 to fig. 4.18.

For  $\text{MoS}_2/\text{WSe}_2/\text{MoS}_2$  trilayer at AAA stacking, when compressive strain is applied, the valance band maxima appears at K point in the Brillouin zone. The conduction band minima occurs at  $\Delta$  point and therefore, the bandgap becomes indirect in nature. As we move from compressive to tensile region, under relaxed condition, the conduction band minima moves from  $\Delta$  point to K point. However, the valance band maxima still appears at K point. The bandgap, therefore, shows direct nature under relaxed condition. As tensile strain is increased further, the bandgap remains direct in nature. However, the bandgap decreases monotonically as we move from compressive to tensile strain regime. For ABA and ACA stacking configurations, the extracted bandstructure show almost similar characteristics. Under compressive strain regime, the bandstructure shows indirect bandgap nature (valance band maxima at K point and conduction band minima at  $\Delta$  point). As we move to tensile strain regime, the bandgap shows direct nature for a particular range of applied strain and as higher tensile strain is applied, the bandgap becomes indirect in nature (valance band maxima at  $\Gamma$  point and conduction band minima at K point). The extracted bandstructures are shown in fig. 4.19 to fig. 4.21.

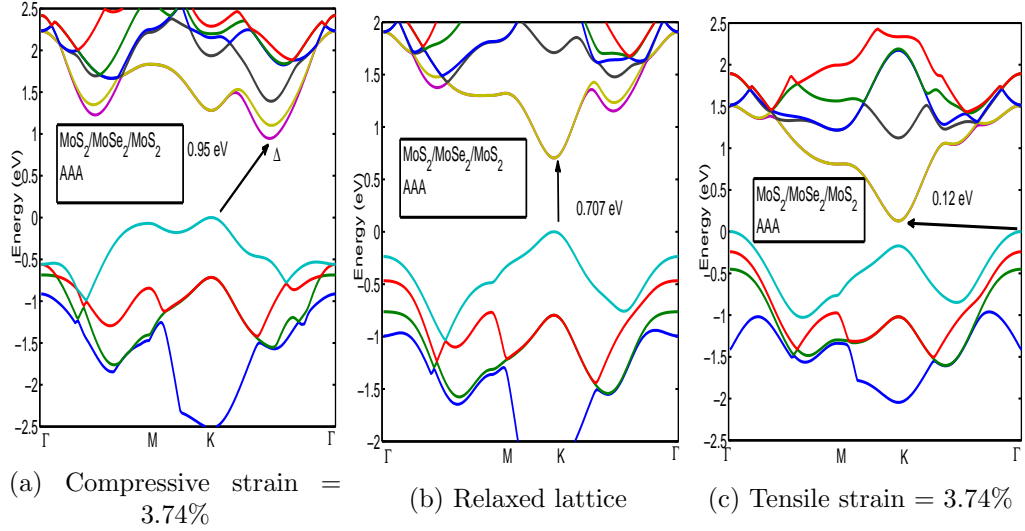


Figure 4.13: Extracted bandstructure of  $\text{MoS}_2/\text{MoSe}_2/\text{MoS}_2$  at AAA stacking under bi-axial strain

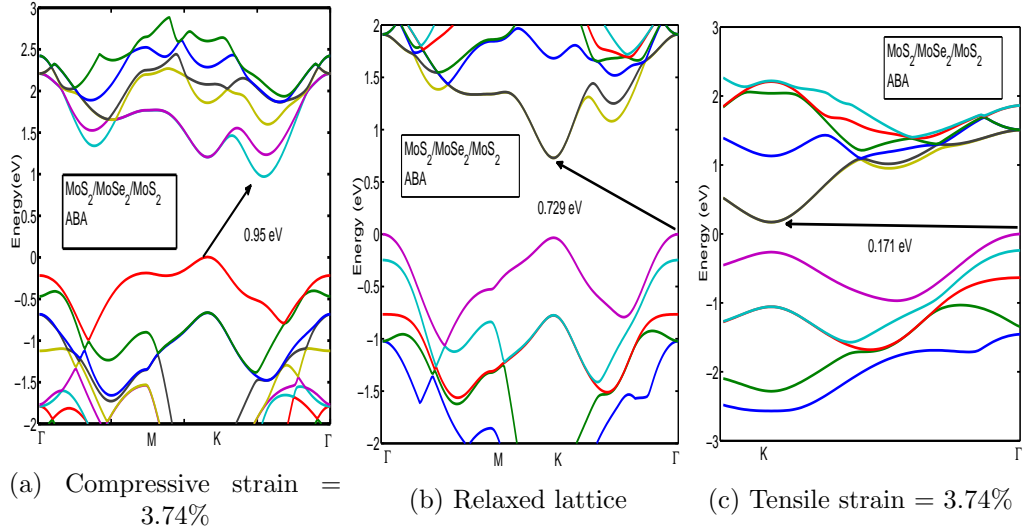


Figure 4.14: Extracted bandstructure of  $\text{MoS}_2/\text{MoSe}_2/\text{MoS}_2$  at ABA stacking under bi-axial strain

### 4.2.3 Effect of Strain on Projected Density of States

In this sub-section, we would discuss the effect of strain on the projected density of states of the trilayer heterostructures. We will report results for the trilayers in AAA stacking configurations only.

Fig. 4.22 shows the extracted bandstructure and projected density of states properties of the trilayers with  $\text{MoSe}_2$  inserted in between the  $\text{MoS}_2$  layers. As can be seen from the figures, under compressive strain, the effect of transition metal atoms of both top/bottom and middle layer on the conduction band minima remains almost similar. This nature is also observed for the p orbital contribution of the chalcogen atoms. The valance band

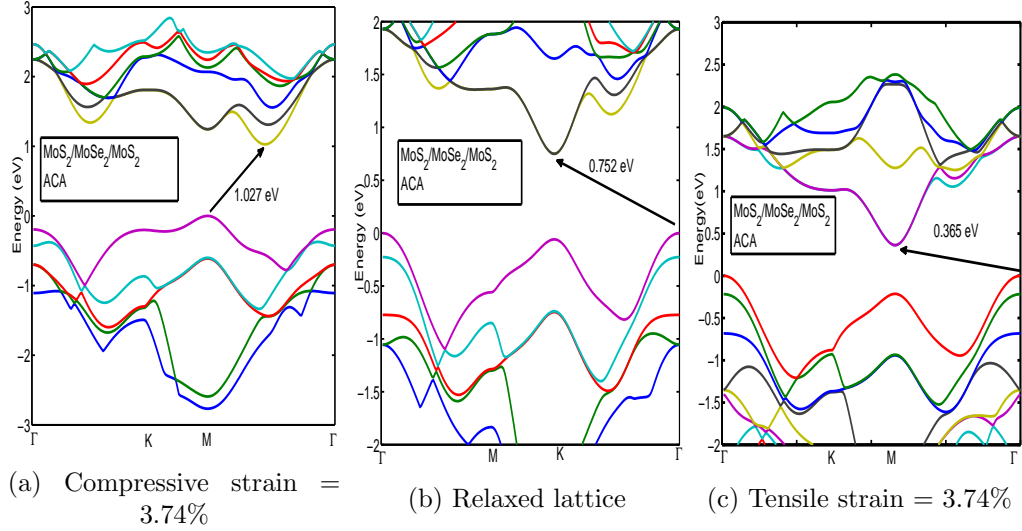


Figure 4.15: Extracted bandstructure of  $\text{MoS}_2/\text{MoSe}_2/\text{MoS}_2$  at ACA stacking under bi-axial strain

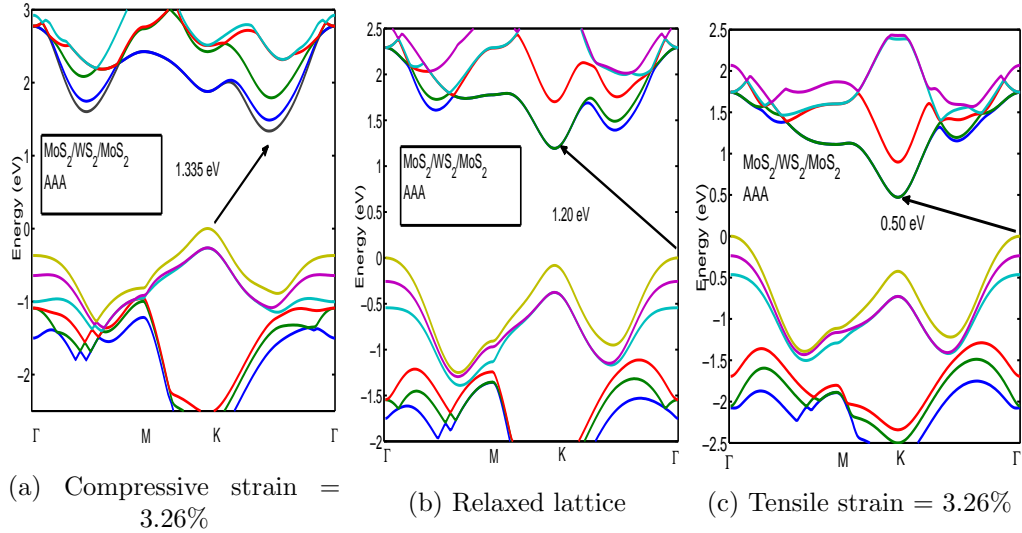


Figure 4.16: Extracted bandstructure of  $\text{MoS}_2/\text{WS}_2/\text{MoS}_2$  at AAA stacking under bi-axial strain

remains mostly affected by the middle TMDC layer under compressive strain as seen from the figure. This observation is different from the trend observed for relaxed trilayers as seen in fig. 4.6 where the top and bottom  $\text{MoS}_2$  layers were found to be contributing to conduction band and the middle  $\text{MoSe}_2$  layer mainly contributed to valance band. Fig. 4.23 shows the projected density of states profile of  $\text{MoS}_2/\text{MoSe}_2/\text{MoS}_2$  trilayer under tensile strain. As can be seen from the figure, the contribution of top and bottom  $\text{MoS}_2$  layers to the conduction band minima is higher compared to the contribution of the middle  $\text{MoSe}_2$  layer. On the other hand, the valance band under tensile strain is contributed mostly by the middle  $\text{MoSe}_2$  layer.

Fig. 4.24 shows the projected density of states profile for the  $\text{MoS}_2/\text{WS}_2/\text{MoS}_2$  trilayer

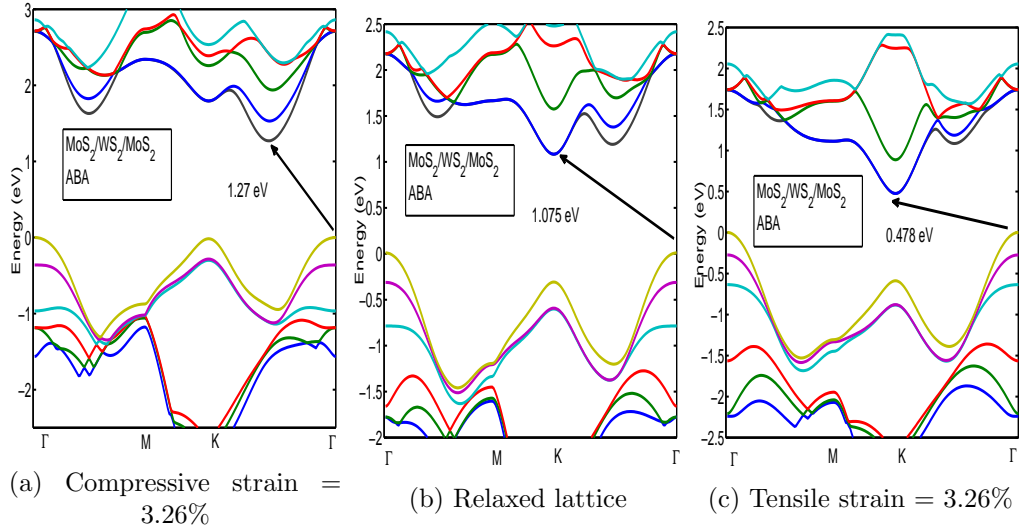


Figure 4.17: Extracted bandstructure of  $\text{MoS}_2/\text{WS}_2/\text{MoS}_2$  at ABA stacking under bi-axial strain

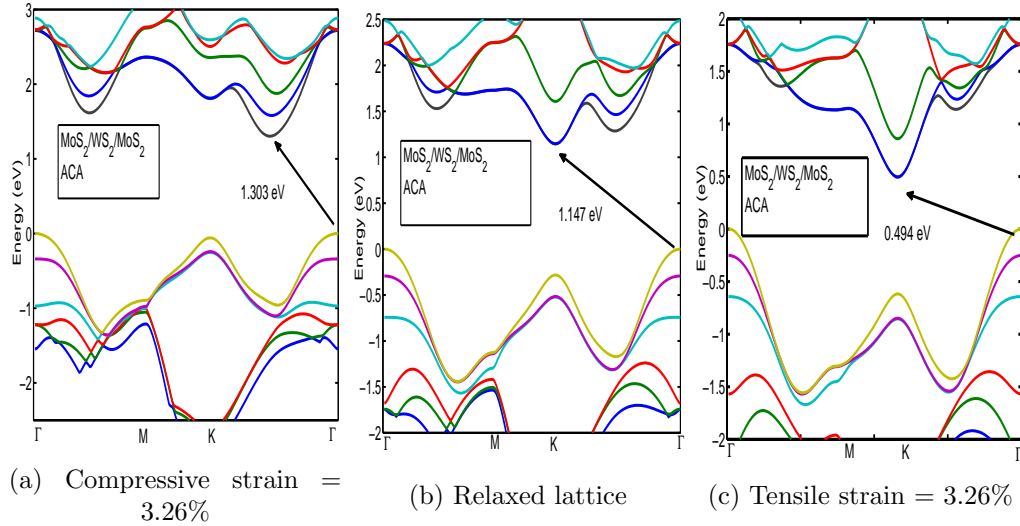


Figure 4.18: Extracted bandstructure of  $\text{MoS}_2/\text{WS}_2/\text{MoS}_2$  at ACA stacking under bi-axial strain

under compressive strain. As seen in the case of  $\text{MoS}_2/\text{MoSe}_2/\text{MoS}_2$ , under compressive strain, the contribution to the conduction band minima appears to be showing similar profile for top/ bottom  $\text{MoS}_2$  and middle  $\text{WS}_2$  layers. On the other hand, valance band appears to be contributed by middle  $\text{WS}_2$  layer only. Fig. 4.25 shows the projected density of states profile for  $\text{MoS}_2/\text{WS}_2/\text{MoS}_2$  under tensile strain. Fig. 4.26 and fig. 4.27 show the projected density of states profile for trilayer  $\text{MoS}_2/\text{WSe}_2/\text{MoS}_2$  heterostructure under compressive and tensile strain respectively.

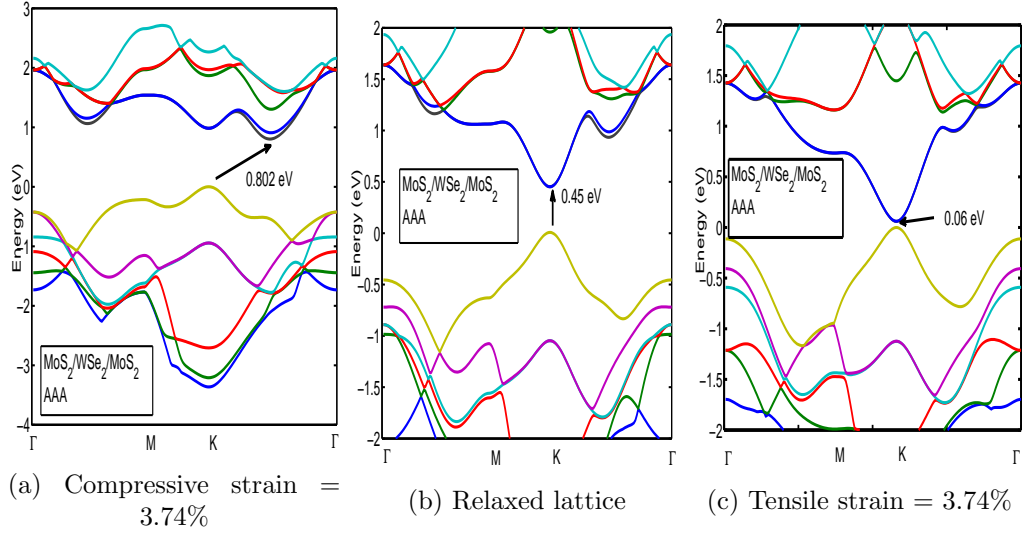


Figure 4.19: Extracted bandstructure of  $\text{MoS}_2/\text{WSe}_2/\text{MoS}_2$  at AAA stacking under bi-axial strain

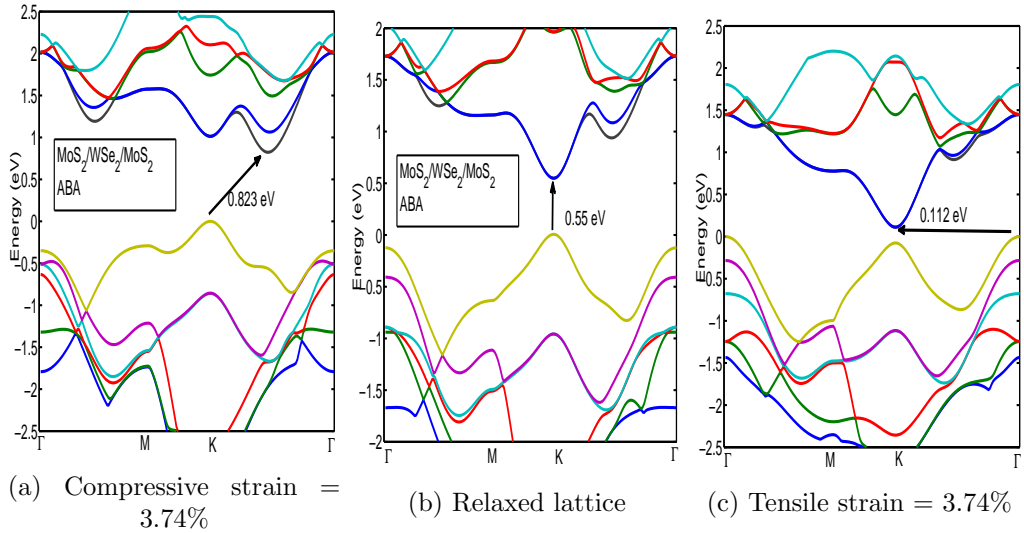


Figure 4.20: Extracted bandstructure of  $\text{MoS}_2/\text{WSe}_2/\text{MoS}_2$  at ABA stacking under bi-axial strain

#### 4.2.4 Effect of Bi-axial Strain on Effective Mass and Bandgap

The effect of in-plane bi-axial strain on bandgap of the trilayer heterostructure at different stacking configurations is shown in fig. 4.28. The bandgap shows a monotonic decreasing trend with compressive to tensile strain application for all the trilayers. For  $\text{MoS}_2/\text{WS}_2/\text{MoS}_2$  and  $\text{MoS}_2/\text{WSe}_2/\text{MoS}_2$  trilayers, ABA and ACA stacking combinations were observed to be showing lower bandgap. However, for  $\text{MoS}_2/\text{MoSe}_2/\text{MoS}_2$  trilayer, ABA and ACA stackings showed higher bandgap in compressive strain region only. The observed bandgap for different trilayer heterostructures also showed indirect to direct transition as a function of applied strain on the trilayer lattice.

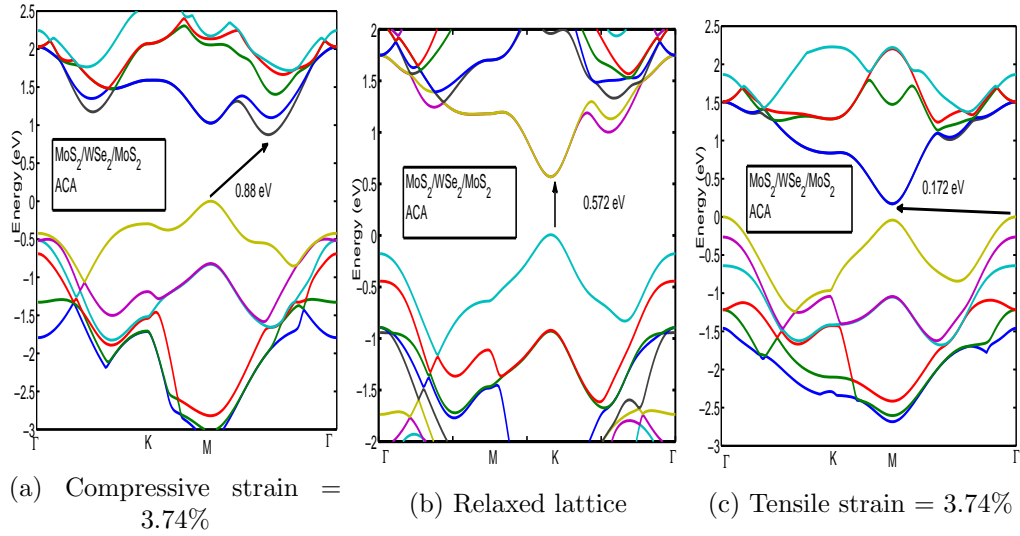


Figure 4.21: Extracted bandstructure of  $\text{MoS}_2/\text{WSe}_2/\text{MoS}_2$  at ACA stacking under bi-axial strain

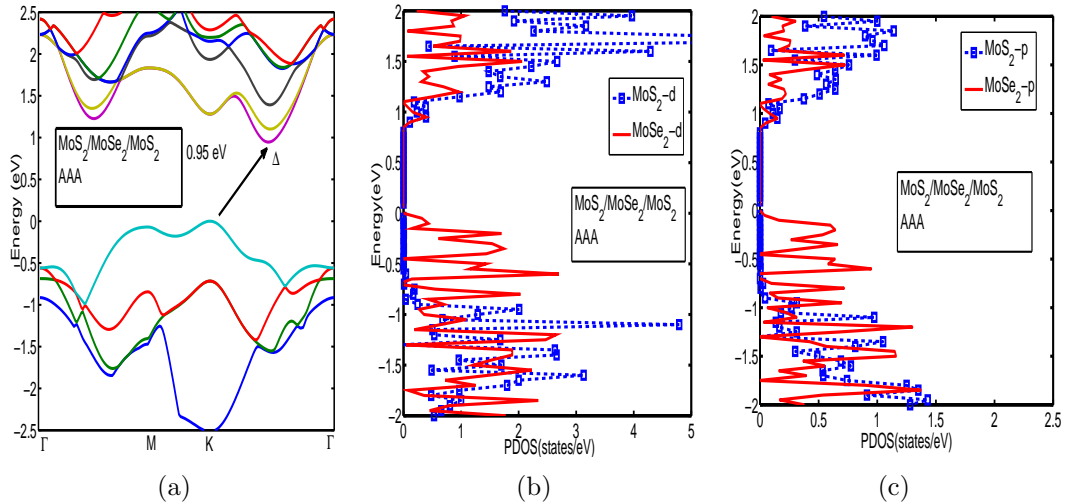


Figure 4.22: (a) Extracted bandstructure for  $\text{MoS}_2/\text{MoSe}_2/\text{MoS}_2$  trilayer at AAA stacking under compressive strain; (b) PDOS profile for transition metal atoms; (c) PDOS profile for chalcogen atoms.

We have also extracted electron effective mass from the extracted bandstructure. Effective mass was calculated by fitting the ab-initio bandstructure at different symmetry points of the Brillouin zone using simple parabolic approach. The effect of bi-axial strain on electron effective mass at different symmetry points (K point and  $\Delta$  point) was also observed.

Fig. 4.29 shows the effective mass at K point in the Brillouin zone as in-plane bi-axial strain is applied for the three trilayer lattice structures. As can be seen from the figure, at K point, the electron effective mass decreases as we move from compressive to tensile strain regime. Under relaxed condition i.e. when applied strain is 0%, for  $\text{MoS}_2/\text{MoSe}_2/\text{MoS}_2$  trilayer, the effective mass at K point is almost same for all

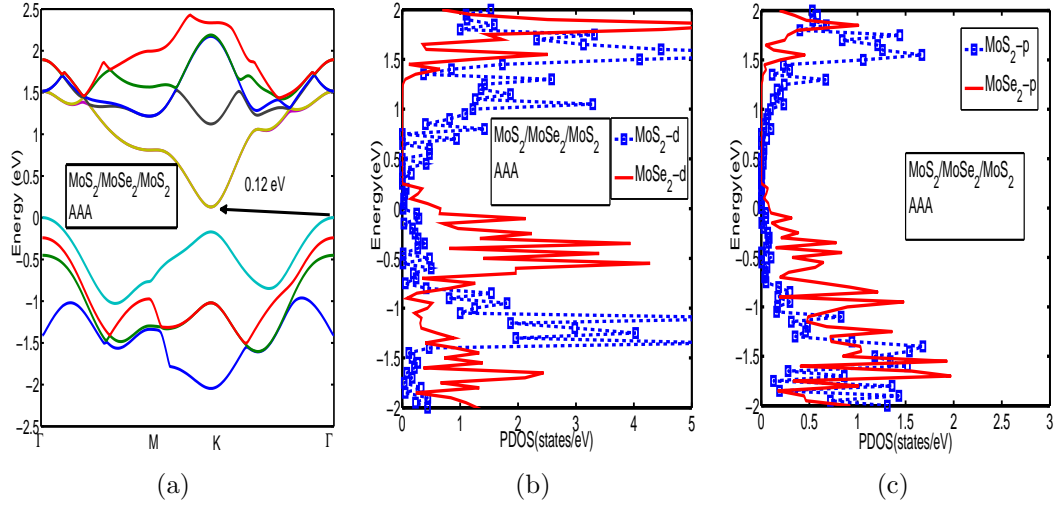


Figure 4.23: (a) Extracted bandstructure for MoS<sub>2</sub>/MoSe<sub>2</sub>/MoS<sub>2</sub> trilayer at AAA stacking under tensile strain; (b) PDOS profile for transition metal atoms; (c) PDOS profile for chalcogen atoms.

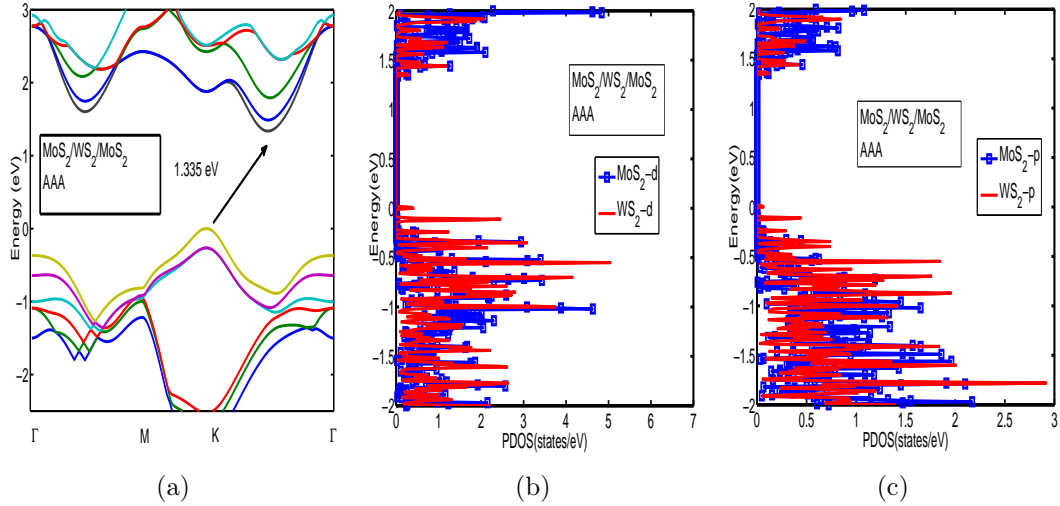


Figure 4.24: (a) Extracted bandstructure for MoS<sub>2</sub>/WS<sub>2</sub>/MoS<sub>2</sub> trilayer at AAA stacking under compressive strain; (b) PDOS profile for transition metal atoms; (c) PDOS profile for chalcogen atoms.

three stacking combinations. This result is also observed for MoS<sub>2</sub>/WS<sub>2</sub>/MoS<sub>2</sub> and MoS<sub>2</sub>/WSe<sub>2</sub>/MoS<sub>2</sub> trilayers. According to our simulation, MoS<sub>2</sub>/WS<sub>2</sub>/MoS<sub>2</sub> trilayer provides slightly higher effective mass among the trilayers studied in this work. At high compressive strain, AAA stacking configuration appears to be giving higher effective mass for MoS<sub>2</sub>/WS<sub>2</sub>/MoS<sub>2</sub> and MoS<sub>2</sub>/WSe<sub>2</sub>/MoS<sub>2</sub> trilayers. However, as tensile strain is applied, the extracted effective mass remains almost same for different stacking configurations of the three trilayers and the effective mass shows decreasing trend with applied tensile strain in all cases.

The change in effective mass at  $\Delta$  point with applied strain for the trilayer heterostructures at different stacking configurations is shown in fig. 4.30 . As seen from the figure,



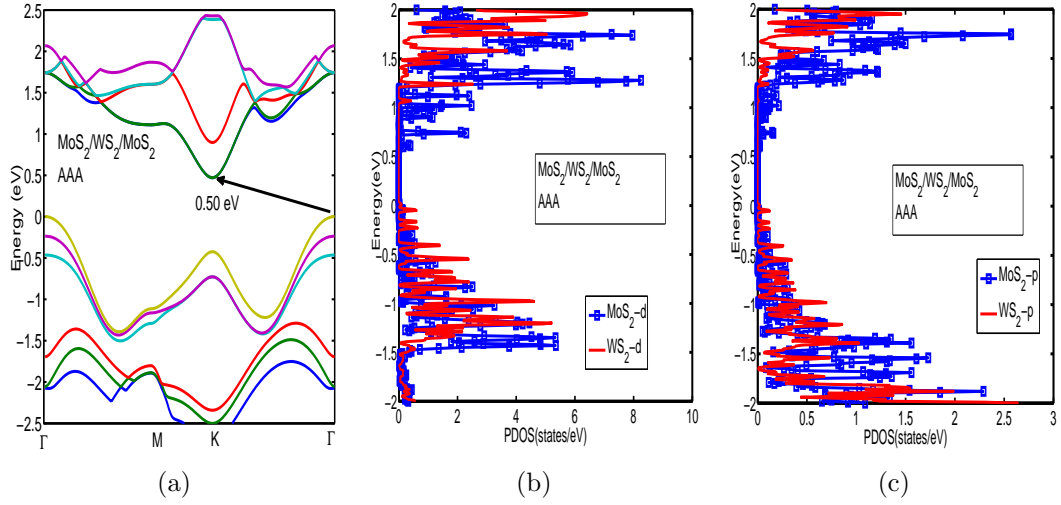


Figure 4.25: (a) Extracted bandstructure for  $\text{MoS}_2/\text{WS}_2/\text{MoS}_2$  trilayer at AAA Stacking under tensile strain; (b) PDOS profile for transition metal atoms; (c) PDOS profile for chalcogen atoms.

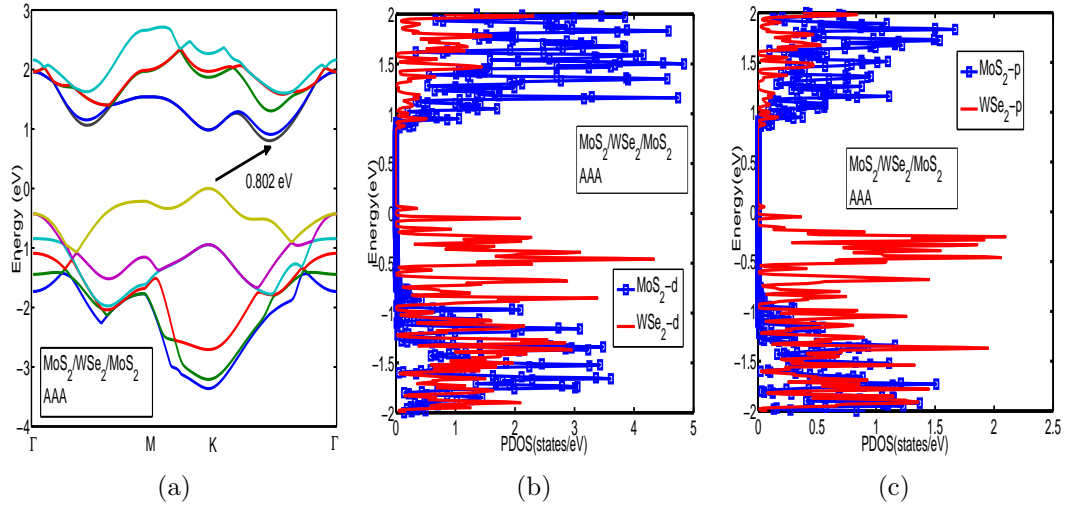


Figure 4.26: (a) Extracted bandstructure for  $\text{MoS}_2/\text{WSe}_2/\text{MoS}_2$  trilayer at AAA Stacking under compressive strain; (b) PDOS profile for transition metal atoms; (c) PDOS profile for chalcogen atoms.

as we move from compressive to tensile strain regime, electron effective mass increases. This can be attributed to the increment in energy at  $\Delta$  point in the conduction band and shift of global conduction band minima to K point with applied tensile strain. This trend of increasing electron effective mass at  $\Delta$  point was observed for all the stacking configurations used in this work. This trend of effective mass variation is also reported for monolayer strained  $\text{MoS}_2$  and other TMDC materials [108] [109]. However, the observed trend for TMDC materials is different from that observed in strained Graphene/h-BN hetero bilayer structures [110], where the electron effective mass increases with applied in-plane tensile strain. Strain engineering, therefore, can be utilized as an effective tool for tuning electronic properties of 2D layered semiconductor heterostructures.

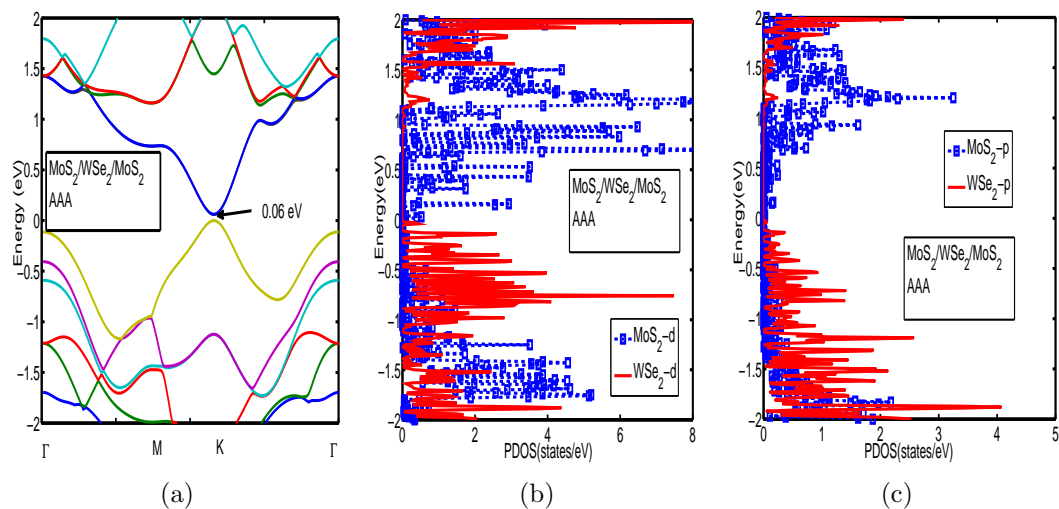


Figure 4.27: (a) Extracted bandstructure for  $\text{MoS}_2/\text{WSe}_2/\text{MoS}_2$  trilayer at AAA Stacking under tensile strain; (b) PDOS profile for transition metal atoms; (c) PDOS profile for chalcogen atoms.

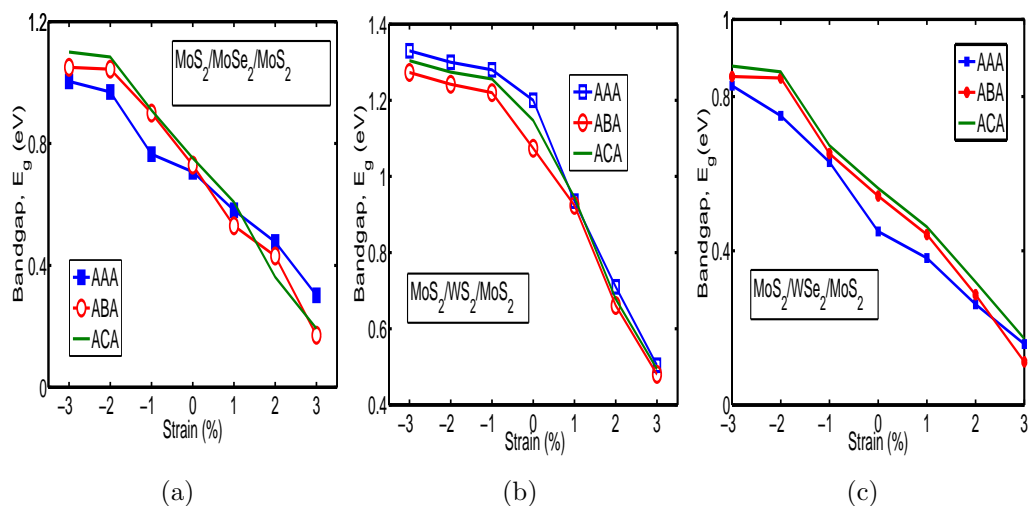


Figure 4.28: Extracted bandgap with applied strain at different stacking configurations for (a)  $\text{MoS}_2/\text{MoSe}_2/\text{MoS}_2$ ; (b)  $\text{MoS}_2/\text{WS}_2/\text{MoS}_2$ ; (c)  $\text{MoS}_2/\text{WSe}_2/\text{MoS}_2$  trialayers.

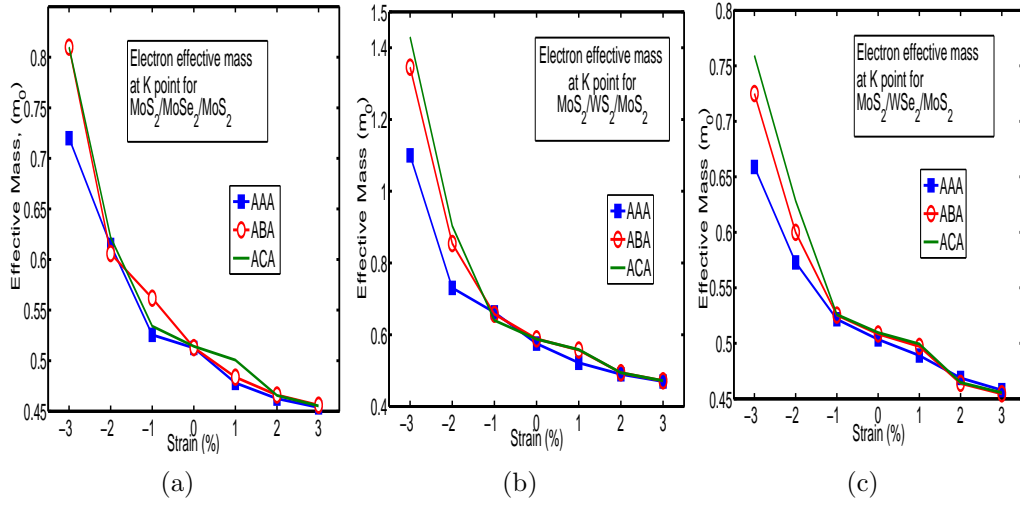


Figure 4.29: Extracted effective mass at K point with applied strain at different stacking configurations for (a)  $\text{MoS}_2/\text{MoSe}_2/\text{MoS}_2$ ; (b)  $\text{MoS}_2/\text{WS}_2/\text{MoS}_2$ ; (c)  $\text{MoS}_2/\text{WSe}_2/\text{MoS}_2$  trilayers.

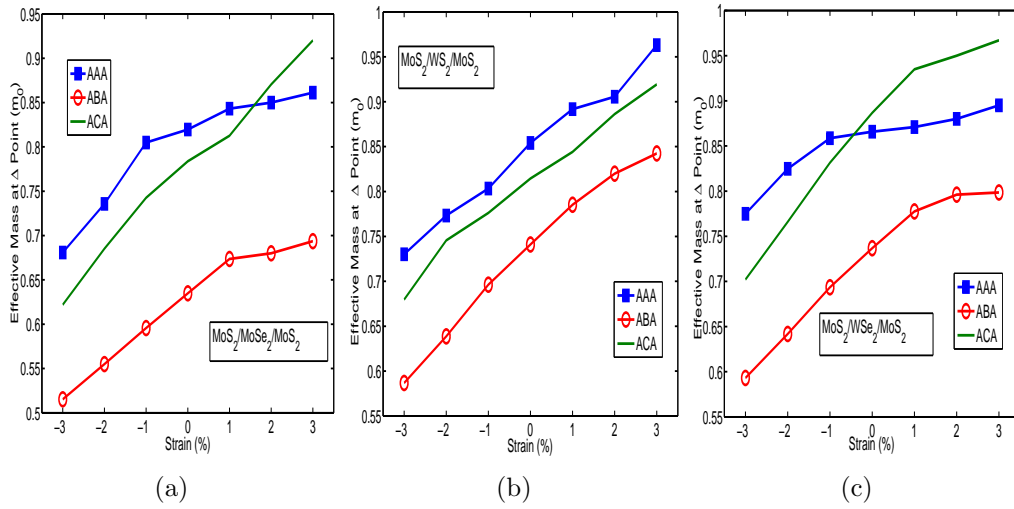


Figure 4.30: Extracted effective mass at  $\Delta$  point with applied strain at different stacking configurations for (a)  $\text{MoS}_2/\text{MoSe}_2/\text{MoS}_2$ ; (b)  $\text{MoS}_2/\text{WS}_2/\text{MoS}_2$ ; (c)  $\text{MoS}_2/\text{WSe}_2/\text{MoS}_2$  trilayers.

### 4.3 MOSFET Application of Trilayer TMDC Heterostructures

In this section, we will present and discuss the results obtained from quantum ballistic simulation of 10 nm double gate MOSFET using trilayer TMDC heterostructure as the channel material. We will use the material parameters extracted from the previous section from transport simulation. We will discuss simulation results for the unstrained

lattice parameters at first. Then simulation results for strained TMDC trilayer MOSFETs will be presented. We will also present the effect of gate underlap geometry on the transport characteristics of the double gate device. In order to discuss basic transport characteristics, we will focus on MoS<sub>2</sub>/MoSe<sub>2</sub>/MoS<sub>2</sub> trilayer at AAA stacking configuration.

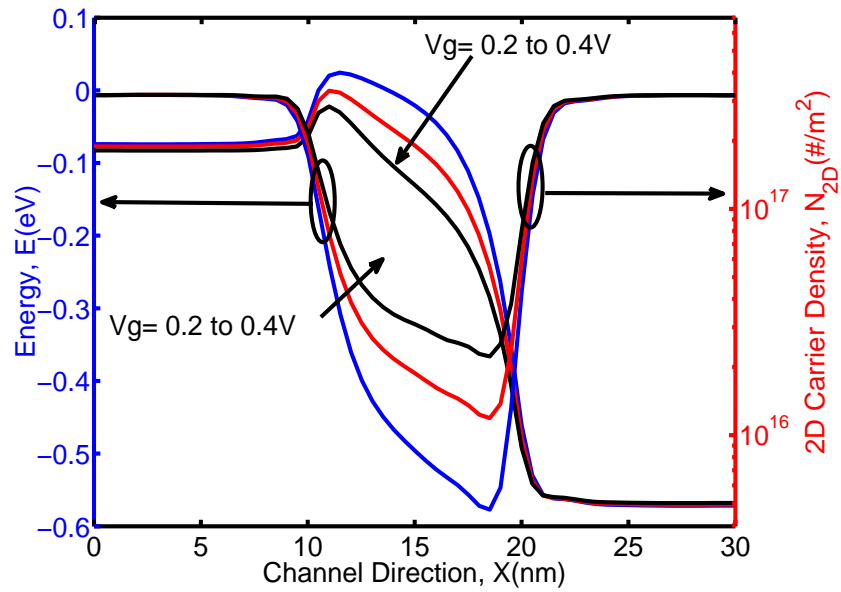
### 4.3.1 Ballistic Simulation of MoS<sub>2</sub>/MoSe<sub>2</sub>/MoS<sub>2</sub> MOSFET

For ballistic simulation of 10 nm double gate MOSFET using trilayer MoS<sub>2</sub>/MoSe<sub>2</sub>/MoS<sub>2</sub> as channel material, we have used the following parameters extracted from first principle simulation:

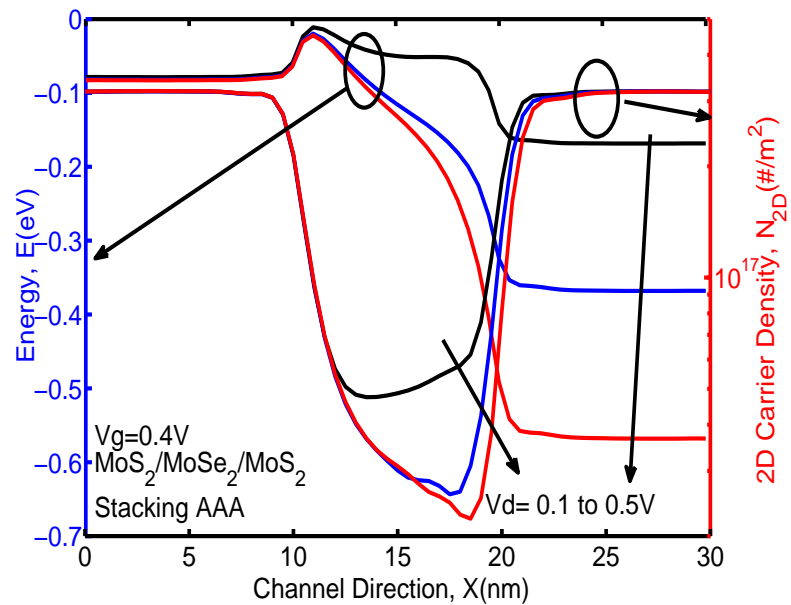
**Table 4.5: Extracted Values of Effective Mass at Conduction Band Minima, Bandgap, Dielectric Constant from First Principle Simulation**

Material	Effective Mass ( $m_0$ )	Bandgap (eV)	Dielectric Constant ( $\epsilon_0$ )
MoS <sub>2</sub> /MoSe <sub>2</sub> /MoS <sub>2</sub>	0.5126	0.707	$\epsilon_{xx}=6.99$
			$\epsilon_{yy}=6.99$
			$\epsilon_{zz}=1.52$
MoS <sub>2</sub> /WSe <sub>2</sub> /MoS <sub>2</sub>	0.5035	0.45	$\epsilon_{xx}=6.84$
			$\epsilon_{yy}=6.84$
			$\epsilon_{zz}=1.53$
MoS <sub>2</sub> /WS <sub>2</sub> /MoS <sub>2</sub>	0.5753	1.2	$\epsilon_{xx}=6.50$
			$\epsilon_{yy}=6.50$
			$\epsilon_{zz}=6.50$

Fig. 4.31a shows the subband energy in the channel at  $V_d=0.5$  V at different gate bias voltage. The figure shows typical MOSFET behavior with gate voltage variation. As gate voltage is increased, gradual lowering of the energy barrier is observed. Top of the barrier energy is also lowered with gate voltage increment to facilitate carrier injection from the source end. At the same time, position of the top of the barrier energy in the channel also shows a slight shift towards the source end. The figure also shows the channel carrier density variation with applied gate bias voltage for  $V_d=0.5$  V. As gate voltage increases, carrier density in the channel increases as well. In our simulation, we have considered only one subband in the channel and only one conduction band valley for carrier density calculation. Fig. 4.31b shows the subband energy with drain bias voltage application along with 2D carrier density in the channel. As can be seen from the figure, subband energy at drain end gets lowered with applied drain bias. The energy barrier height at the source end also gets affected by the applied drain bias which can be attributed to drain induced barrier lowering effect that becomes prominent at 10 nm channel length.



(a)



(b)

Figure 4.31: (a) 1<sup>st</sup> subband energy and 2D carrier density in the channel when MoS<sub>2</sub>/MoSe<sub>2</sub>/MoS<sub>2</sub> trilayer is used as the channel material as the gate voltage is varied. (b) 1<sup>st</sup> subband energy and 2D carrier density in the channel when MoS<sub>2</sub>/MoSe<sub>2</sub>/MoS<sub>2</sub> trilayer is used as the channel material at different drain voltages.

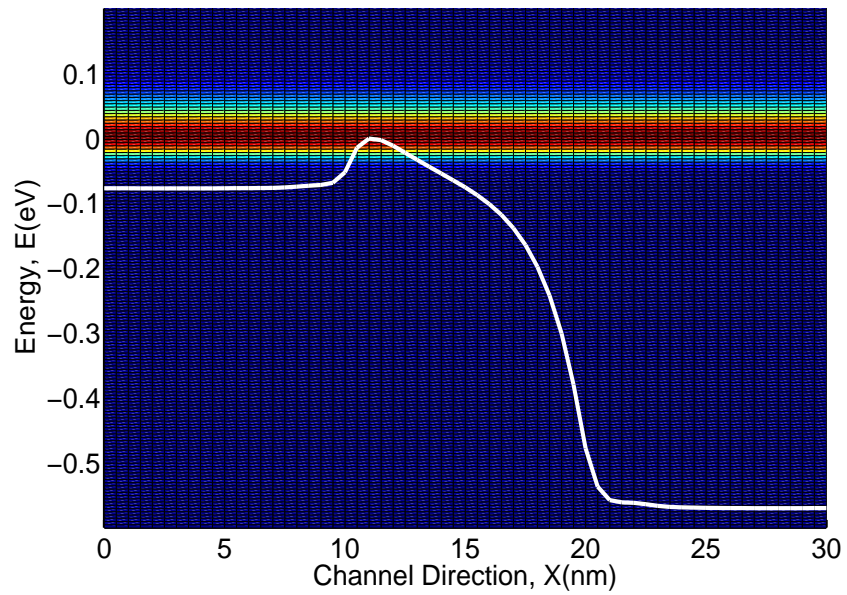
Fig. 4.32a shows the energy resolved current density extracted from the ballistic simulation. As can be seen from the figure, under the barrier transport is very small compared to over the barrier ballistic transport which refers to strong electrostatic control as channel thickness extremely scaled down to a thickness of 2 nm. The local density of states (LDOS) characteristics is shown in fig. 4.32b. The LDOS profile shows strong interference patterns as carriers are being reflected from the energy barriers at source end and drain end.

Fig. 4.33a shows the transmission co-efficient along with first subband energy in the channel for  $V_g=0.4$  V and  $V_d=0.5$  V. As ballistic simulation is considered, the transmission co-efficient rises sharply at about top of the barrier energy and becomes 1 for carriers with higher energy. Fig 4.33b) shows the Id- $V_d$  characteristics of the double gate device with  $\text{MoS}_2/\text{MoSe}_2/\text{MoS}_2$  trilayer TMDC material used as the channel material. The figure shows nice saturation behavior with applied drain bias voltage which highlights good electrostatic effect of the double gate device at 2 nm channel thickness. 4.34 shows the Id- $V_g$  characteristics of the double gate device at two different drain bias voltages. The figure shows device characteristics in both linear and log scale. From the log scale characteristics of the device, we can calculate the device subthreshold swing (SS) which highlights the sharp turn-on characteristics of the device. The logscale characteristics at two different drain voltages can be used to calculate drain induced barrier lowering (DIBL) of the device. From our calculation, we extracted SS and DIBL values of 80.256 mV/dec and 26.2 mV/V respectively when  $\text{MoS}_2/\text{MoSe}_2/\text{MoS}_2$  trilayer was used as the channel material.

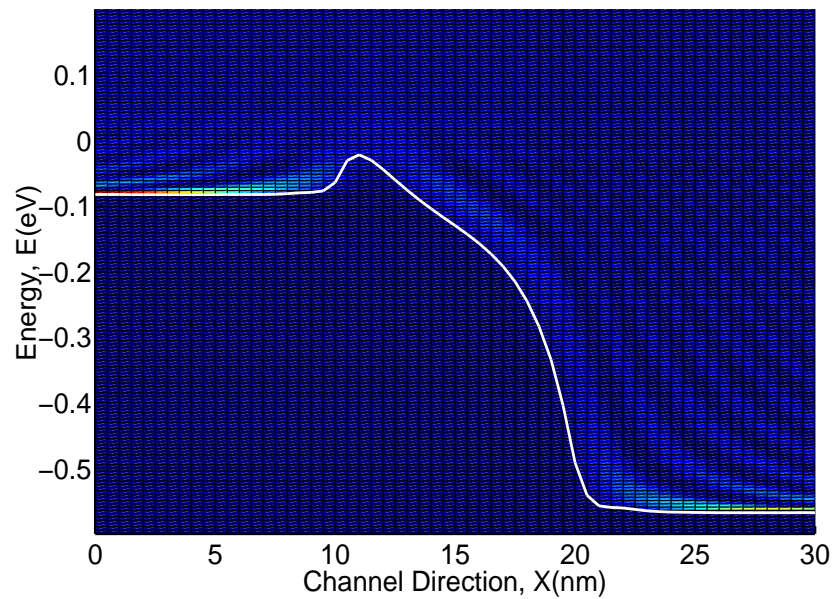
### 4.3.2 Ballistic Simulation of the Double Gate Device with Different TMDC Trilayers as Channel Material

We have explored the effect of different trilayer TMDC materials on the ballistic performance of the double gate device. In our study of material variation, we have kept other physical device parameters same as before. We have considered only AAA stacking configuration of the trilayers for ballistic simulation study.

Fig. 4.35a shows the first subband profile of the double gate device at  $V_g=0.4$  V and  $V_d=0.5$  V for different trilayer heterostructure. For  $\text{MoS}_2/\text{WS}_2/\text{MoS}_2$  trilayer, the simulation shows slightly lowered energy barrier height at the source end. On the other hand, the insertion of  $\text{MoSe}_2$  or  $\text{WSe}_2$  monolayer between  $\text{MoS}_2$  monolayers does not cause a significant change in subband profile. This can be attributed to similar carrier effective mass at conduction band minima for these two trilayer heterostructures in AAA stacking under relaxed condition. 2D carrier density in the channel at  $V_d=0.5$  V



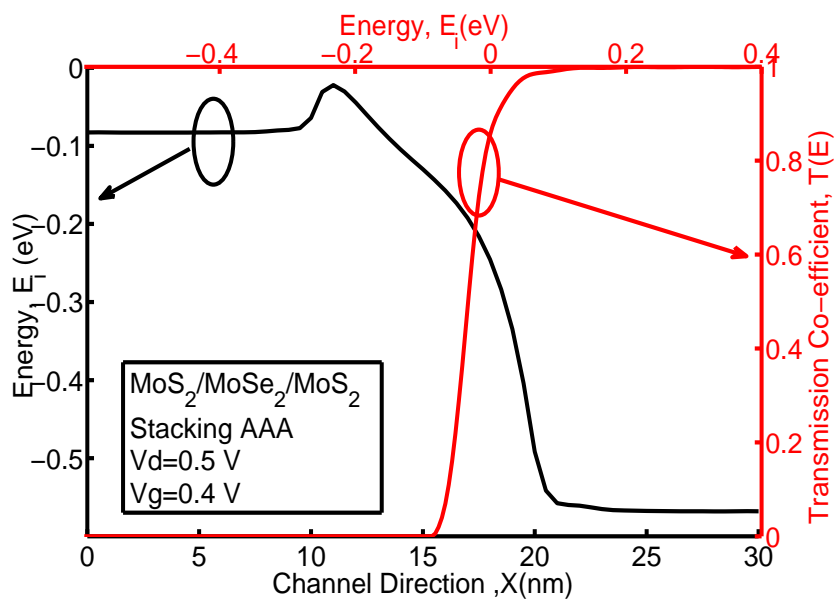
(a)



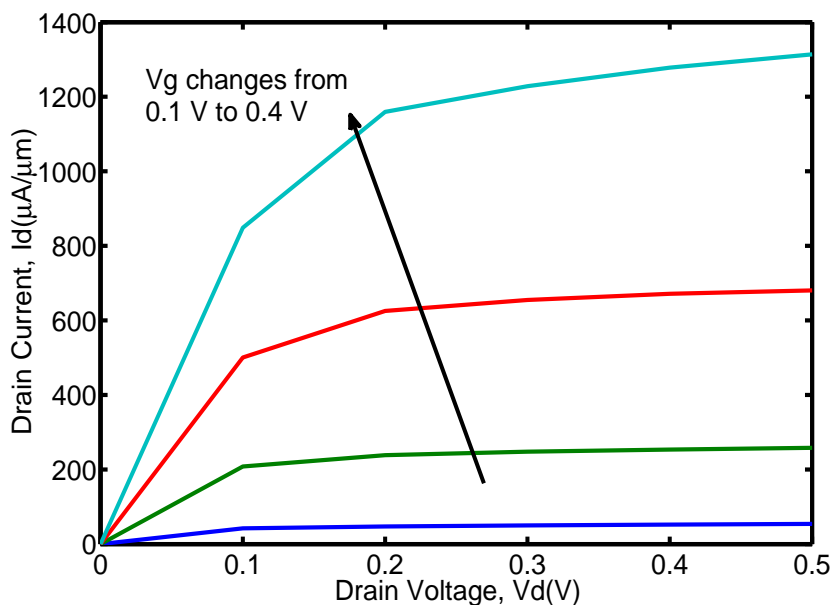
(b)

Figure 4.32: (a) Energy resolved current density in the channel at  $V_d=0.5\text{V}$  and  $V_g=0.4\text{V}$ . As seen from the figure, carriers above the top of the barrier contribute significantly to total drain current. (b) Local density of states profile obtained from ballistic simulation. Interference type patterns at source and drain end suggest strong carrier reflection from energy barriers at source and drain ends.





(a)



(b)

Figure 4.33: (a) 1<sup>st</sup> subband energy along with transmission coefficient extracted from NEGF simulation. Transmission co-efficient rises to a value of 1.0 just at about the top of the barrier energy. (b)  $I_d$ - $V_d$  characteristics of the double gate device using  $\text{MoS}_2/\text{MoSe}_2/\text{MoS}_2$  trilayer as the channel material.

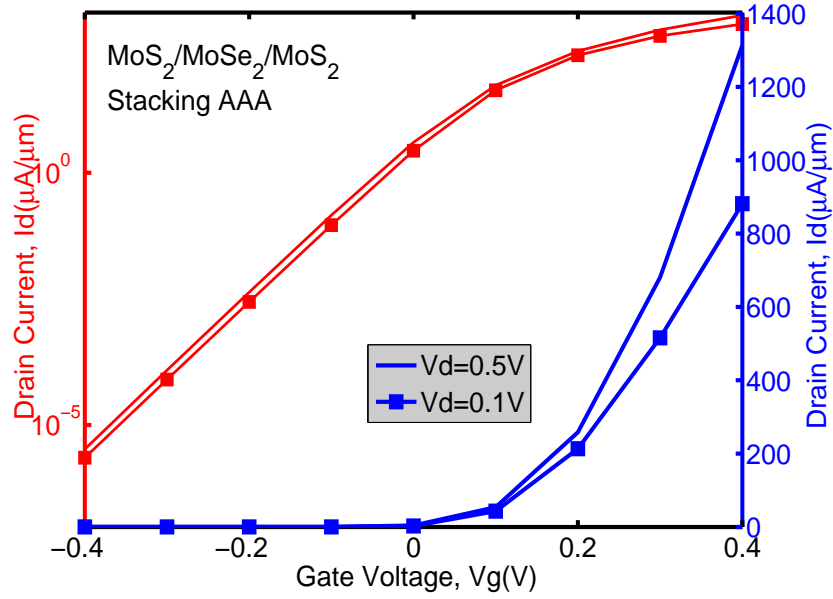
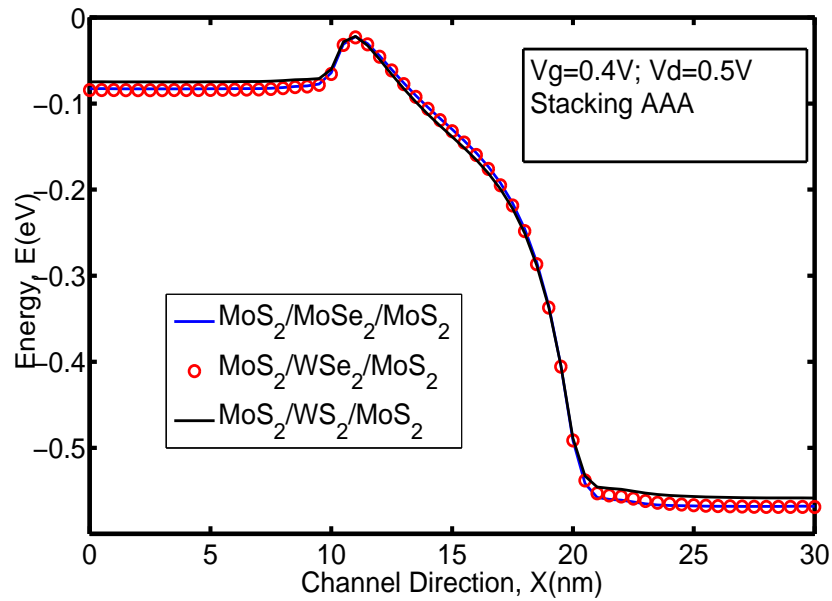


Figure 4.34: Id-Vg characteristics of the 10 nm double gate device in both linear and log scale for two different drain bias voltage conditions.

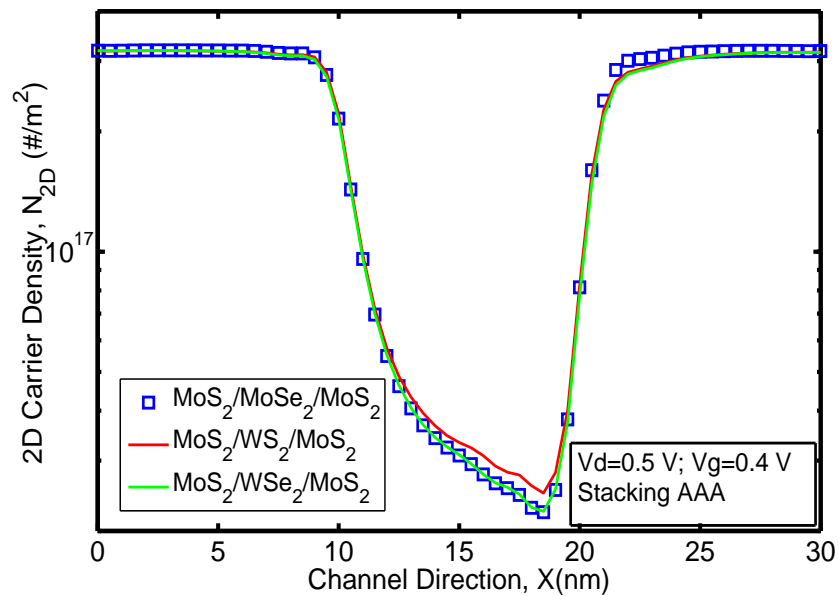
and  $V_g=0.4$  V for the heterostructures in fig. 4.35b shows that with the insertion of a  $WS_2$  monolayer, the carrier density in the channel increases slightly. Although  $WSe_2$  monolayer and  $MoSe_2$  monolayer insertion result in similar subband energy profiles, the insertion of  $MoSe_2$  monolayer was seen to be providing a slightly higher carrier density in the channel for the same gate and drain bias voltage condition. Fig. 4.36a shows the gate capacitance profile for the double gate device for different trilayer heterostructures. Gate capacitance has been calculated using the carrier density at the top of the barrier position obtained at  $V_d=0.0$  V. According to our study,  $MoS_2/WS_2/MoS_2$  appears to be showing higher gate capacitance which can be attributed to higher carrier accumulation in the channel for the trilayer. Fig. 4.36b shows the Id-Vg characteristics of the device at  $V_d=0.5$  V in both linear and log scale for different trilayer TMDC heterostructure. Higher carrier density in the channel results in slightly higher drain current for  $MoS_2/WS_2/MoS_2$  trilayer device. From the ballistic simulation, we have extracted values of SS and DIBL for different trilayer material systems. The extracted values of SS, DIBL is given in Table 4.6. In our simulation, we have found the lowest DIBL and SS values for  $MoS_2/WS_2/MoS_2$  trilayer.

**Table 4.6: Comparison of SS and DIBL for MOSFETs Using Different Trilayer TMDC as Channel Materials**

Material	SS (mV/dec)	DIBL (mV/V)
$MoS_2/MoSe_2/MoS_2$	80.256	26.2
$MoS_2/WS_2/MoS_2$	79.122	25.3
$MoS_2/WSe_2/MoS_2$	83.47	30.1

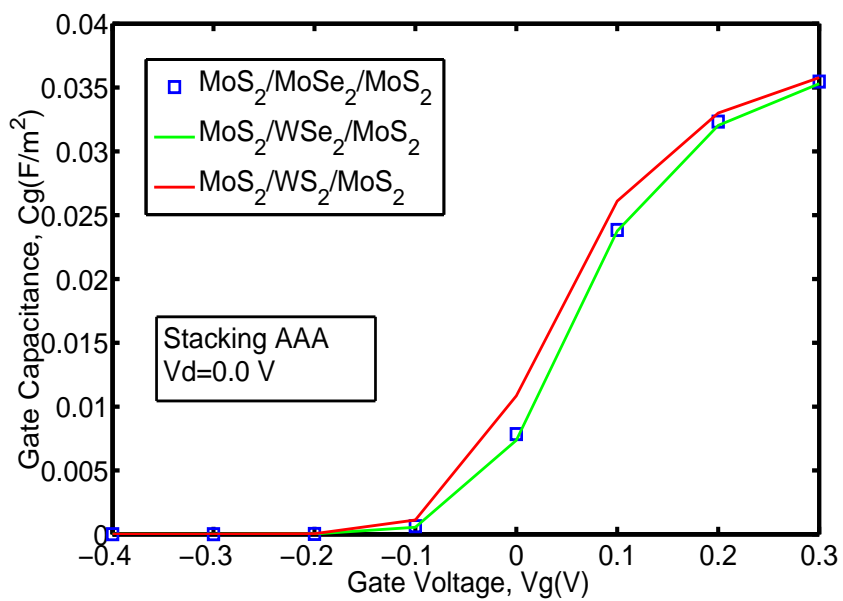


(a)

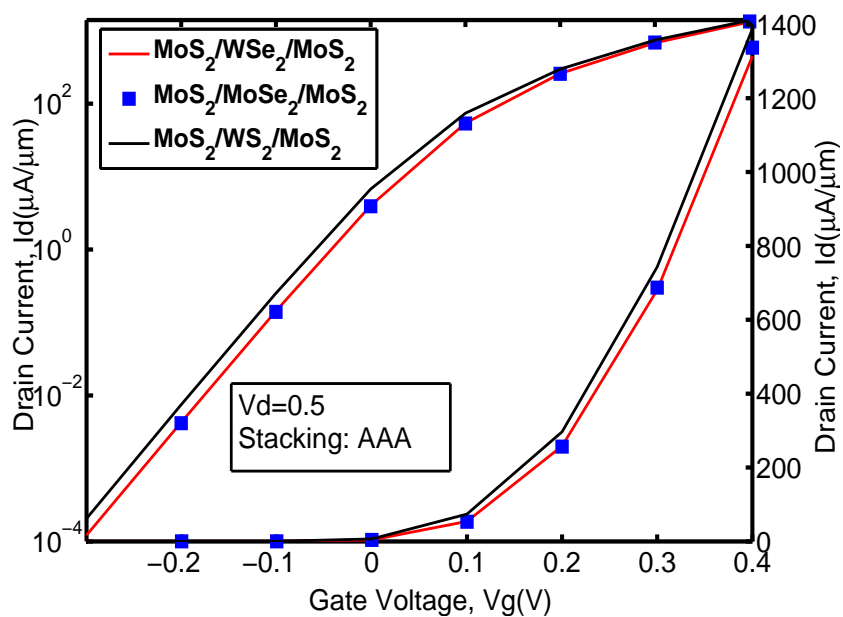


(b)

Figure 4.35: (a) 1<sup>st</sup> subband energy in the channel for three different trilayer configurations. MoS<sub>2</sub>/WS<sub>2</sub>/MoS<sub>2</sub> trilayer results in slightly lower energy barrier height near source end which results in more carrier injection from the source. (b) 2D carrier density in the channel extracted from NEGF simulations. Due to higher source carrier injection, the carrier density in the channel is higher for MoS<sub>2</sub>/WS<sub>2</sub>/MoS<sub>2</sub> trilayer.



(a)



(b)

Figure 4.36: (a) Gate capacitance calculated from 2D carrier density in the channel at the top of the barrier at  $V_d = 0.0$  V. (b)  $I_d$ - $V_g$  characteristics for three different trilayer structures in both linear and log scale at  $V_d = 0.5$  V.

### 4.3.3 Ballistic Simulation of Strained Trilayer TMDC Double Gate MOSFET

We have also performed ballistic simulation of the double gate device using strained trilayer TMDC heterostructure as the channel material. We will be discussing simulation results for tensile strain regime only. As seen from the first principle simulation data, tensile strain lowers electron effective mass at the conduction band minima and reduces bandgap of the trilayer system. The conduction band minima moves to K point in the Brillouin zone with applied tensile strain. Fig. 4.37 shows the effect of tensile strain on the 1<sup>st</sup> subband energy and 2D carrier density in the channel when MoS<sub>2</sub>/MoSe<sub>2</sub>/MoS<sub>2</sub> at AAA stacking is used as the channel material. As seen from the figure, 1% tensile strain application does not cause a significant change in 1<sup>st</sup> subband energy in the device. However, the energy barrier height is slightly lower at the source end when relaxed MoS<sub>2</sub>/MoSe<sub>2</sub>/MoS<sub>2</sub> trilayer is used as the channel material. Carrier density in the channel appears to be slightly higher for the relaxed lattice structure which can be attributed to slightly higher carrier effective mass.

Fig. 4.38 shows that tensile strain application lowers drain current for all the trilayer material systems. This can be attributed to lowering of electron effective mass at the conduction band minima with increased tensile strain. Although we see a lowering in drain current, there appears to be no significant change in the sub-threshold characteristics of the device i.e. value of sub-threshold swing (SS) with applied tensile strain in case of MoS<sub>2</sub>/MoSe<sub>2</sub>/MoS<sub>2</sub> and MoS<sub>2</sub>/WS<sub>2</sub>/MoS<sub>2</sub> trilayers under just 1% tensile strain application. However, for MoS<sub>2</sub>/WSe<sub>2</sub>/MoS<sub>2</sub> trilayer, lower bandgap and carrier effective mass results in an increase in the band to band tunneling current which becomes significant at low gate bias voltage condition and therefore we observe an increase in SS and deterioration in sub-threshold device performance. In fig. 4.38a, we have incorporated the results of ballistic simulation using 2% tensile strain for MoS<sub>2</sub>/MoSe<sub>2</sub>/MoS<sub>2</sub> trilayer. The profile shows slightly lowered drain current than 1% tensile strained trilayer. However, as the bandgap decreases with increasing tensile strain (Fig. 4.28a), the source-drain leakage current becomes higher and an increment of sub-threshold swing is observed.

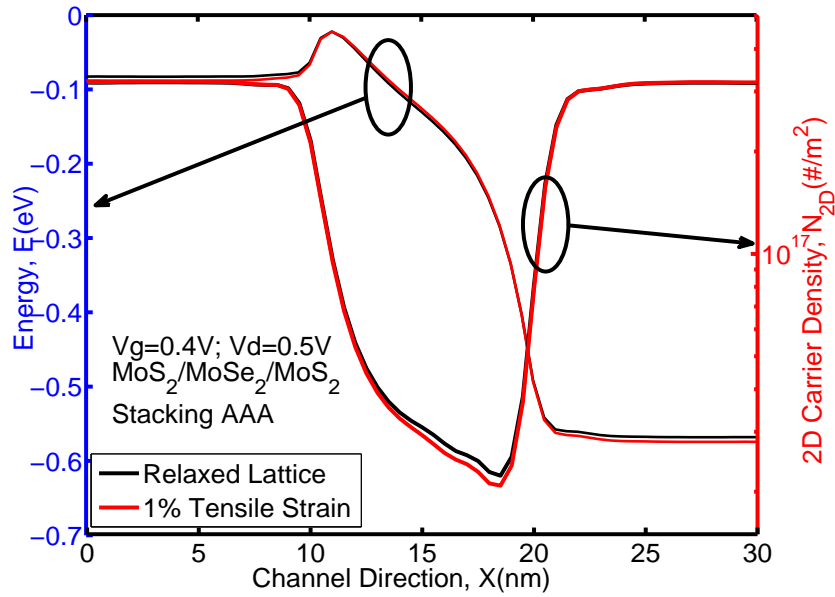


Figure 4.37: 1<sup>st</sup> subband energy along with 2D carrier density in the channel at  $V_g=0.4$  V and  $V_d=0.5$  V for the  $\text{MoS}_2/\text{MoSe}_2/\text{MoS}_2$  trilayer under the relaxed condition and under 1% tensile strain.

#### 4.3.4 Ballistic Simulation of the Double Gate MOSFET Using Gate Underlap Geometry

We have studied the effect of gate underlap geometry on device performance of trilayer TMDC MOSFETs. Effect of gate underlap geometry on the performance of monolayer  $\text{MoS}_2$  FET has been studied for sub-10 nm VLSI applications in detail in [111]. Implementation of gate underlap geometry, increases effective channel length which, in turn, increases series resistance in the channel. Underlap geometry also reduces effective coupling of source and drain contact with the channel and therefore lowers the effect of drain electric field on device performance and therefore could improve device electrostatics by reducing SS. In the study of gate underlap geometry, gate length has been kept fixed at 10 nm and  $\text{HfO}_2$  has been used as the gate dielectric material.

Fig. 4.39a shows the schematic diagram of underlap geometry. We performed ballistic simulation with gate underlap length varying uniformly from 0 nm to 3 nm in 1 nm step. The other physical device parameters have been kept unchanged. Fig. 4.39b shows the  $I_d$ - $V_g$  characteristics when  $\text{MoS}_2/\text{MoSe}_2/\text{MoS}_2$  trilayer has been used as the channel material. The figure shows a reduction in ‘on’ current when gate underlap length is increased. This can be attributed to the fact that, increasing channel underlap length increases effective channel length and therefore induces additional resistance in the channel. Fig. 4.39c and fig. 4.39d show the  $I_d$ - $V_g$  characteristics at different gate

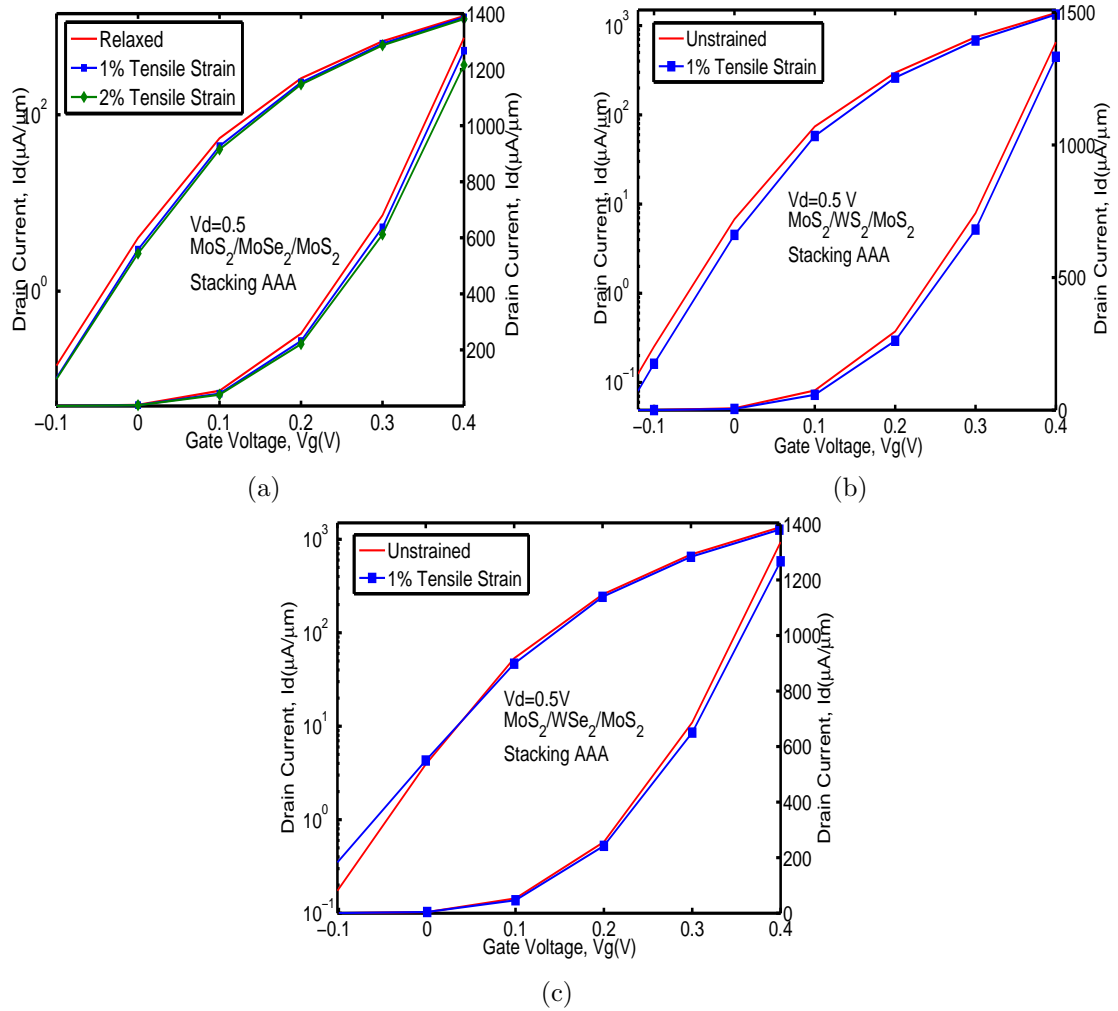


Figure 4.38:  $I_d$ - $V_g$  characteristics at  $V_d=0.5$  V for three different trilayer heterostructure channel materials: (a)  $\text{MoS}_2/\text{MoSe}_2/\text{MoS}_2$ ; (b)  $\text{MoS}_2/\text{WS}_2/\text{MoS}_2$ ; (c)  $\text{MoS}_2/\text{WSe}_2/\text{MoS}_2$ . In all the cases, the simulation shows a decrease in drain current when tensile strain is applied in the channel. This could be attributed to lower carrier density in the channel under tensile strain application.

underlap lengths for  $\text{MoS}_2/\text{WS}_2/\text{MoS}_2$  and  $\text{MoS}_2/\text{WSe}_2/\text{MoS}_2$  respectively. However, despite this reduction in ‘on’ current, increasing gate underlap region length does improve sub-threshold performance by lowering effect of the fringing electric field from source and drain. Proper optimization of gate underlap region therefore, is required to design TMDC transistor that could meet the low sub-threshold requirement for future technology nodes without significantly compromising the ‘on’ current requirement.

Fig. 4.40a shows the variation of ‘on’ current calculated at  $V_g=0.4$  V and  $V_d=0.5$  V at different gate underlap lengths. As can be seen from the figure, at different underlap lengths, the  $\text{MoS}_2/\text{MoSe}_2/\text{MoS}_2$  and  $\text{MoS}_2/\text{WSe}_2/\text{MoS}_2$  trilayers give almost equal ‘on’ currents. However,  $\text{MoS}_2/\text{WS}_2/\text{MoS}_2$  trilayer improves the ‘on’ current performance of the device. 4.40b shows the variation of sub-threshold swing with gate underlap length. In all cases, we see a decrease in SS with increased gate underlap length. Of these



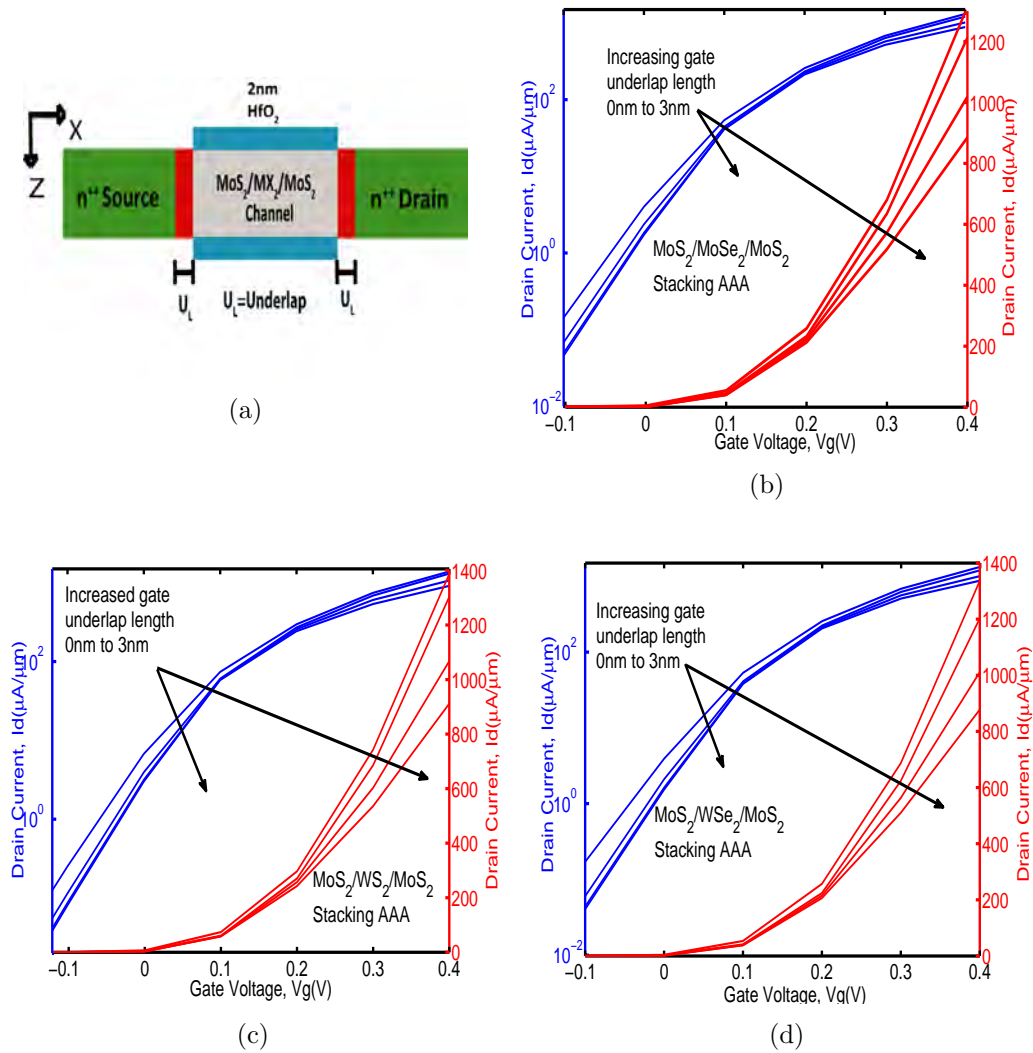
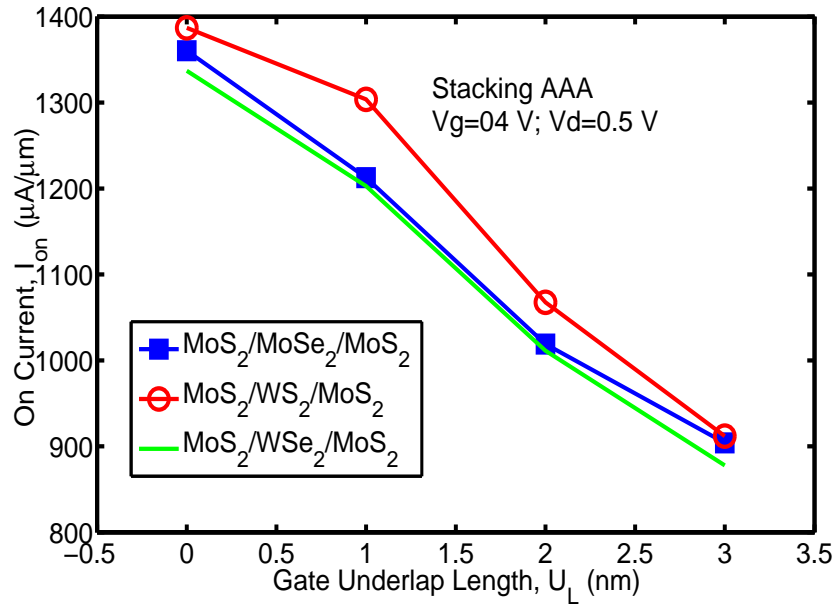
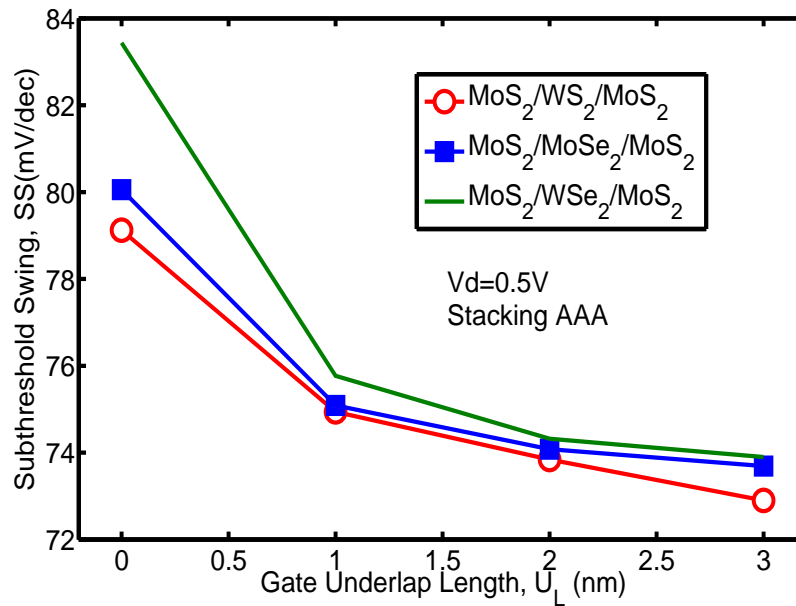


Figure 4.39: (a) Schematic representation of the underlap device geometry used in this study. Here, the red segment shows the underlap length which has been kept constant on both sides of the gate. The gate length is kept fixed at  $10\text{ nm}$ .  $I_d$ - $V_g$  characteristics at  $V_d=0.5\text{ V}$  when (b)  $\text{MoS}_2/\text{MoSe}_2/\text{MoS}_2$ ; (c)  $\text{MoS}_2/\text{WS}_2/\text{MoS}_2$  (d)  $\text{MoS}_2/\text{WSe}_2/\text{MoS}_2$  has been used as the channel material. As seen from these figures, underlap device geometry improves sub-threshold characteristics. However, due to increase in effective channel length, the ‘on’ current drops as well.

material systems,  $\text{MoS}_2/\text{WSe}_2/\text{MoS}_2$  trilayer shows highest sub-threshold swing values which can be attributed to its low bandgap.



(a)



(b)

Figure 4.40: (a) Variation of ‘on’ current with gate underlap length. ‘On’ condition is taken at  $V_g=0.4$  V and  $V_d=0.5$  V. As revealed from simulation MoS<sub>2</sub>/WS<sub>2</sub>/MoS<sub>2</sub> trilayer gives higher ‘on’ current up to 3 nm of gate underlap length. (b) Variation of sub-threshold swing (SS) with underlap length. As seen from the simulation, increased gate underlap length improves device electrostatics and lowers the value of sub-threshold swing. MoS<sub>2</sub>/WS<sub>2</sub>/MoS<sub>2</sub> trilayer appears to be giving the lowest sub-threshold swing among the three trilayer heterostructures.

# Chapter 5

## Conclusion

### 5.1 Summary

In this work, we have performed a first principle simulation study on trilayer  $\text{MoS}_2/\text{MX}_2/\text{MoS}_2$  (M=Mo or, W; X=S or, Se) heterostructures using open source simulation package Quantum Espresso. The effect of different stacking configuration, bi-axial compressive and tensile strain on the electronic properties was observed and studied. To get better understanding of the bandstructure profile, projected density of states of different atoms were also studied. Of the three inserted monolayers under study ( $\text{WS}_2$ ,  $\text{WSe}_2$ ,  $\text{MoSe}_2$ ),  $\text{WS}_2$  insertion resulted in higher bandgap. Under relaxed condition,  $\text{MoS}_2/\text{MoSe}_2/\text{MoS}_2$  trilayer at AAA stacking configuration shows direct bandgap nature. On the other hand, ABA and ACA stacking lead to indirect bandgap semiconductors. As for the  $\text{MoS}_2/\text{WS}_2/\text{MoS}_2$  trilayer, the bandgap was found to be indirect under relaxed condition for the stacking configurations used in this study. The study also revealed that  $\text{MoS}_2/\text{WSe}_2/\text{MoS}_2$  lattice at all stacking configurations might show direct bandgap characteristics under relaxed condition. This trilayer shows the lowest bandgap among the material systems under study in this work. Their direct bandgap nature under relaxed condition can be utilized in optoelectronic applications. Extracted bandgap from first principle simulation of different stackings of this trilayer suggests possible application in infrared region of the electromagnetic spectrum. Application of tensile strain may result in lowering of bandgap in all the heterostructures configurations. Application of tensile strain also increases the curvature at the conduction band minima and therefore lowers the electron effective mass. We have also performed a ballistic simulation study on the performance of van der Waal trilayer TMDC heterostructures as channel materials in MOSFETs for sub-10 nm region operation. For ballistic simulation of the double gate MOSFET structure, we have used FUMS approach with NEGF

formalism. Of the three trilayer heterostructures studied, MoS<sub>2</sub>/WS<sub>2</sub>/MoS<sub>2</sub> trilayer appears to be showing better sub-threshold performance and higher drain current due to higher carrier accumulation. MoS<sub>2</sub>/WSe<sub>2</sub>/MoS<sub>2</sub> trilayer shows degraded sub-threshold performance due to its low bandgap and lower carrier effective mass. Application of tensile strain causes a reduction in drain current for all the materials studied. Implementation of gate underlap geometry could improve sub-threshold performance at the cost of ‘on’ current reduction of these devices, as seen from our simulation.

## 5.2 Suggestion for Future Work

- Vertical electric field application has been used as an effective way to tune the electronic properties of monolayer and multilayer TMDC materials. The effect of vertical electric field on the bandstructure and electronic properties of trilayer TMDC heterostructure could lead to more interesting and exciting results.
- To get more realistic results of device characteristics, the effect of interface traps can be included in the simulation of double gate TMDC MOSFET.
- Although ballistic transport has been assumed in this work at 10 nm gate length regime, the inclusion of scattering in transport simulation using Buttiker probe method can be implemented to evaluate the transport characteristics more accurately.
- Multiscale simulation and modeling which incorporates the application of Wannier functions to represent electronic states to simulate nanoribbon devices can be found for Graphene treated with hydrogen, fluorine etc. Such simulation framework can be developed for TMDC bilayer and trilayer heterostructure FETs to get more realistic results and insight into their transport properties.

# Bibliography

- [1] G. E. Moore, “Cramming more components onto integrated circuits, reprinted from electronics, volume 38, number 8, april 19, 1965, pp. 114 ff.” *IEEE Solid-State Circuits Newsletter*, vol. 3, no. 20, pp. 33–35, 2006.
- [2] G. E. Moore *et al.*, “Progress in digital integrated electronics,” in *Electron Devices Meeting*, vol. 21, 1975, pp. 11–13.
- [3] S. Thompson, N. Anand, M. Armstrong, C. Auth, B. Arcot, M. Alavi, P. Bai, J. Bielefeld, R. Bigwood, J. Brandenburg *et al.*, “A 90 nm logic technology featuring 50 nm strained silicon channel transistors, 7 layers of cu interconnects, low k ild, and  $1\mu\text{m}^2$  sram cell,” in *Electron Devices Meeting, 2002. IEDM’02. International*. IEEE, 2002, pp. 61–64.
- [4] C. Auth, “45 nm high-k+metal gate strain-enhanced cmos transistors,” in *2008 IEEE Custom Integrated Circuits Conference*. IEEE, 2008, pp. 379–386.
- [5] R. Courtland, “The status of moore’s law: It’s complicated,” *IEEE Spectrum*, vol. 28, 2013.
- [6] C. Auth, C. Allen, A. Blattner, D. Bergstrom, M. Brazier, M. Bost, M. Buehler, V. Chikarmane, T. Ghani, T. Glassman *et al.*, “A 22 nm high performance and low-power cmos technology featuring fully-depleted tri-gate transistors, self-aligned contacts and high density mim capacitors,” in *VLSI technology (VLSIT), 2012 symposium on*. IEEE, 2012, pp. 131–132.
- [7] S. Natarajan, M. Agostinelli, S. Akbar, M. Bost, A. Bowonder, V. Chikarmane, S. Chouksey, A. Dasgupta, K. Fischer, Q. Fu *et al.*, “A 14 nm logic technology featuring 2<sup>nd</sup>-generation finfet, air-gapped interconnects, self-aligned double patterning and a  $0.0588\ \mu\text{m}^2$  sram cell size,” in *2014 IEEE International Electron Devices Meeting*. IEEE, 2014, pp. 3–7.
- [8] I. Home. [online]. available. [Online]. Available: <http://www.itrs2.net/>
- [9] M. M. Waldrop, “The chips are down for moore’s law,” *Nature News*, vol. 530, no. 7589, p. 144, 2016.

- [10] R. Ramanathan, "Intel multi-core processors: Making the move to quad-core and beyond, white paper," *Intel Corporation*.
- [11] T. Cross. (2016) After moore's law. [Online]. Available: <http://www.economist.com/technology-quarterly/2016-03-12/after-moores-law>.
- [12] INTEL. [online]. available. [Online]. Available: <http://www.intel.com/content/www/us/en/homepage.html>.
- [13] K. Ahmed and K. Schuegraf, "Transistor wars," *IEEE Spectrum*, vol. 48, no. 11, pp. 50–66, 2011.
- [14] D. E. Nikonov and I. A. Young, "Overview of beyond-cmos devices and a uniform methodology for their benchmarking," *Proceedings of the IEEE*, vol. 101, no. 12, pp. 2498–2533, 2013.
- [15] J.-A. Carballo, W.-T. J. Chan, P. A. Gargini, A. B. Kahng, and S. Nath, "Itrs 2.0: Toward a re-framing of the semiconductor technology roadmap," in *2014 IEEE 32nd International Conference on Computer Design (ICCD)*. IEEE, 2014, pp. 139–146.
- [16] K. Bernstein, R. K. Cavin, W. Porod, A. Seabaugh, and J. Welser, "Device and architecture outlook for beyond cmos switches," *Proceedings of the IEEE*, vol. 98, no. 12, pp. 2169–2184, 2010.
- [17] D. E. Nikonov and I. A. Young, "Benchmarking of beyond-cmos exploratory devices for logic integrated circuits," *IEEE Journal on Exploratory Solid-State Computational Devices and Circuits*, vol. 1, pp. 3–11, 2015.
- [18] J. A. Del Alamo, "Nanometre-scale electronics with iii-v compound semiconductors," *Nature*, vol. 479, no. 7373, pp. 317–323, 2011.
- [19] Y. Chen, Y. Baeyens, N. Weimann, J. Lee, J. Weiner, V. Houtsma, and Y. Yang, "Recent advances in iii-v electronics," in *IEEE Custom Integrated Circuits Conference 2006*, 2006.
- [20] K. S. Novoselov, A. K. Geim, S. V. Morozov, D. Jiang, Y. Zhang, S. V. Dubonos, I. V. Grigorieva, and A. A. Firsov, "Electric field effect in atomically thin carbon films," *science*, vol. 306, no. 5696, pp. 666–669, 2004.
- [21] M. Y. Han, B. Özyilmaz, Y. Zhang, and P. Kim, "Energy band-gap engineering of graphene nanoribbons," *Physical review letters*, vol. 98, no. 20, p. 206805, 2007.

- [22] M. P. Lima, A. Fazzio, and A. J. da Silva, “Edge effects in bilayer graphene nanoribbons: Ab initio total-energy density functional theory calculations,” *Physical Review B*, vol. 79, no. 15, p. 153401, 2009.
- [23] S. Zhou, G.-H. Gweon, A. Fedorov, P. First, W. De Heer, D.-H. Lee, F. Guinea, A. C. Neto, and A. Lanzara, “Substrate-induced bandgap opening in epitaxial graphene,” *Nature materials*, vol. 6, no. 10, pp. 770–775, 2007.
- [24] X. Peng and R. Ahuja, “Symmetry breaking induced bandgap in epitaxial graphene layers on sic,” *Nano letters*, vol. 8, no. 12, pp. 4464–4468, 2008.
- [25] E. V. Castro, K. Novoselov, S. Morozov, N. Peres, J. L. Dos Santos, J. Nilsson, F. Guinea, A. Geim, and A. C. Neto, “Biased bilayer graphene: semiconductor with a gap tunable by the electric field effect,” *Physical Review Letters*, vol. 99, no. 21, p. 216802, 2007.
- [26] P. Gava, M. Lazzeri, A. M. Saitta, and F. Mauri, “Ab initio study of gap opening and screening effects in gated bilayer graphene,” *Physical Review B*, vol. 79, no. 16, p. 165431, 2009.
- [27] T. Ohta, A. Bostwick, T. Seyller, K. Horn, and E. Rotenberg, “Controlling the electronic structure of bilayer graphene,” *Science*, vol. 313, no. 5789, pp. 951–954, 2006.
- [28] R. Mas-Balleste, C. Gomez-Navarro, J. Gomez-Herrero, and F. Zamora, “2d materials: to graphene and beyond,” *Nanoscale*, vol. 3, no. 1, pp. 20–30, 2011.
- [29] T. Cao, G. Wang, W. Han, H. Ye, C. Zhu, J. Shi, Q. Niu, P. Tan, E. Wang, B. Liu *et al.*, “Valley-selective circular dichroism of monolayer molybdenum disulphide,” *Nature communications*, vol. 3, p. 887, 2012.
- [30] U. of Twente. [online]. available. [Online]. Available: <https://www.utwente.nl/ewi/ne/archive/!/2014/4/331901/marie-curie-fellowship-for-nepostdoc-johnny-wong>.
- [31] D. Jariwala, V. K. Sangwan, L. J. Lauhon, T. J. Marks, and M. C. Hersam, “Emerging device applications for semiconducting two-dimensional transition metal dichalcogenides,” *ACS nano*, vol. 8, no. 2, pp. 1102–1120, 2014.
- [32] H. Fang, S. Chuang, T. C. Chang, K. Takei, T. Takahashi, and A. Javey, “High-performance single layered wse<sub>2</sub> p-fets with chemically doped contacts,” *Nano letters*, vol. 12, no. 7, pp. 3788–3792, 2012.

- [33] Z. Zeng, C. Tan, X. Huang, S. Bao, and H. Zhang, "Growth of noble metal nanoparticles on single-layer  $\text{TiS}_2$  and  $\text{TaS}_2$  nanosheets for hydrogen evolution reaction," *Energy & Environmental Science*, vol. 7, no. 2, pp. 797–803, 2014.
- [34] Z. Zeng, Z. Yin, X. Huang, H. Li, Q. He, G. Lu, F. Boey, and H. Zhang, "Single-layer semiconducting nanosheets: High-yield preparation and device fabrication," *Angewandte Chemie International Edition*, vol. 50, no. 47, pp. 11 093–11 097, 2011.
- [35] W. S. Yun, S. Han, S. C. Hong, I. G. Kim, and J. Lee, "Thickness and strain effects on electronic structures of transition metal dichalcogenides:  $2\text{h-mx}_2$  semiconductors ( $m = \text{Mo, W}$ ;  $x = \text{S, Se, Te}$ )," *Physical Review B*, vol. 85, no. 3, p. 033305, 2012.
- [36] A. Kumar and P. Ahluwalia, "Semiconductor to metal transition in bilayer transition metals dichalcogenides  $\text{mx}_2$  ( $m = \text{Mo, W}$ ;  $x = \text{S, Se, Te}$ )," *Modelling and Simulation in Materials Science and Engineering*, vol. 21, no. 6, p. 065015, 2013.
- [37] S. Bhattacharyya and A. K. Singh, "Semiconductor-metal transition in semiconducting bilayer sheets of transition-metal dichalcogenides," *Physical Review B*, vol. 86, no. 7, p. 075454, 2012.
- [38] A. Ramasubramaniam, D. Naveh, and E. Towe, "Tunable band gaps in bilayer transition-metal dichalcogenides," *Physical Review B*, vol. 84, no. 20, p. 205325, 2011.
- [39] N. Lu, H. Guo, L. Li, J. Dai, L. Wang, W.-N. Mei, X. Wu, and X. C. Zeng, "MoS<sub>2</sub>/mx<sub>2</sub> heterobilayers: bandgap engineering via tensile strain or external electrical field," *Nanoscale*, vol. 6, no. 5, pp. 2879–2886, 2014.
- [40] A. Kumar and P. Ahluwalia, "Electronic structure of transition metal dichalcogenides monolayers  $1\text{h-mx}_2$  ( $m = \text{Mo, W}$ ;  $x = \text{S, Se, Te}$ ) from ab-initio theory: new direct band gap semiconductors," *The European Physical Journal B*, vol. 85, no. 6, pp. 1–7, 2012.
- [41] B. Radisavljevic, A. Radenovic, J. Brivio, i. V. Giacometti, and A. Kis, "Single-layer mos<sub>2</sub> transistors," *Nature nanotechnology*, vol. 6, no. 3, pp. 147–150, 2011.
- [42] S.-L. Li, K. Wakabayashi, Y. Xu, S. Nakaharai, K. Komatsu, W.-W. Li, Y.-F. Lin, A. Aparecido-Ferreira, and K. Tsukagoshi, "Thickness-dependent interfacial coulomb scattering in atomically thin field-effect transistors," *Nano letters*, vol. 13, no. 8, pp. 3546–3552, 2013.



- [43] S. Kim, A. Konar, W.-S. Hwang, J. H. Lee, J. Lee, J. Yang, C. Jung, H. Kim, J.-B. Yoo, J.-Y. Choi *et al.*, “High-mobility and low-power thin-film transistors based on multilayer mos<sub>2</sub> crystals,” *Nature communications*, vol. 3, p. 1011, 2012.
- [44] S. Das, H.-Y. Chen, A. V. Penumatcha, and J. Appenzeller, “High performance multilayer mos<sub>2</sub> transistors with scandium contacts,” *Nano letters*, vol. 13, no. 1, pp. 100–105, 2012.
- [45] I. Popov, G. Seifert, and D. Tománek, “Designing electrical contacts to mos<sub>2</sub> monolayers: a computational study,” *Physical review letters*, vol. 108, no. 15, p. 156802, 2012.
- [46] H. Liu, M. Si, Y. Deng, A. T. Neal, Y. Du, S. Najmaei, P. M. Ajayan, J. Lou, and P. D. Ye, “Switching mechanism in single-layer molybdenum disulfide transistors: an insight into current flow across schottky barriers,” *ACS nano*, vol. 8, no. 1, pp. 1031–1038, 2013.
- [47] W. Liu, J. Kang, W. Cao, D. Sarkar, Y. Khatami, D. Jena, and K. Banerjee, “High-performance few-layer-mos<sub>2</sub> field-effect-transistor with record low contact-resistance,” in *2013 IEEE International Electron Devices Meeting*. IEEE, 2013, pp. 19–4.
- [48] D. Voiry, A. Mohite, and M. Chhowalla, “Phase engineering of transition metal dichalcogenides,” *Chemical Society Reviews*, vol. 44, no. 9, pp. 2702–2712, 2015.
- [49] E. Kadantsev, “Electronic structure of exfoliated mos<sub>2</sub>,” in *MoS<sub>2</sub>*. Springer, 2014, pp. 37–51.
- [50] T. Li and G. Galli, “Electronic properties of mos<sub>2</sub> nanoparticles,” *The Journal of Physical Chemistry C*, vol. 111, no. 44, pp. 16 192–16 196, 2007.
- [51] Y. Cheng and U. Schwingenschlögl, “Mos<sub>2</sub>: A first-principles perspective,” in *MoS<sub>2</sub>*. Springer, 2014, pp. 103–128.
- [52] E. S. Kadantsev and P. Hawrylak, “Electronic structure of a single mos<sub>2</sub> monolayer,” *Solid State Communications*, vol. 152, no. 10, pp. 909–913, 2012.
- [53] S.-M. Choi, S.-H. Jhi, and Y.-W. Son, “Effects of strain on electronic properties of graphene,” *Physical Review B*, vol. 81, no. 8, p. 081407, 2010.
- [54] G. Gui, J. Li, and J. Zhong, “Band structure engineering of graphene by strain: first-principles calculations,” *Physical Review B*, vol. 78, no. 7, p. 075435, 2008.
- [55] K. F. Mak, C. H. Lui, J. Shan, and T. F. Heinz, “Observation of an electric-field-induced band gap in bilayer graphene by infrared spectroscopy,” *Physical review letters*, vol. 102, no. 25, p. 256405, 2009.

- [56] A. Kumar and P. Ahluwalia, “Mechanical strain dependent electronic and dielectric properties of two-dimensional honeycomb structures of  $\text{mox}_2$  ( $x = \text{s, se, te}$ ),” *Physica B: Condensed Matter*, vol. 419, pp. 66–75, 2013.
- [57] P. Johari and V. B. Shenoy, “Tuning the electronic properties of semiconducting transition metal dichalcogenides by applying mechanical strains,” *ACS nano*, vol. 6, no. 6, pp. 5449–5456, 2012.
- [58] T. Niu and A. Li, “From two-dimensional materials to heterostructures,” *Progress in Surface Science*, vol. 90, no. 1, pp. 21–45, 2015.
- [59] Q. Wang, P. Wu, G. Cao, and M. Huang, “First-principles study of the structural and electronic properties of  $\text{mos}_2/\text{ws}_2$  and  $\text{mos}_2/\text{mote}_2$  monolayer heterostructures,” *Journal of Physics D: Applied Physics*, vol. 46, no. 50, p. 505308, 2013.
- [60] J. Kang, J. Li, S.-S. Li, J.-B. Xia, and L.-W. Wang, “Electronic structural moire pattern effects on  $\text{mos}_2/\text{mose}_2$  2d heterostructures,” *Nano letters*, vol. 13, no. 11, pp. 5485–5490, 2013.
- [61] Y. Gong, J. Lin, X. Wang, G. Shi, S. Lei, Z. Lin, X. Zou, G. Ye, R. Vajtai, B. I. Yakobson *et al.*, “Vertical and in-plane heterostructures from  $\text{ws}_2/\text{mos}_2$  monolayers,” *Nature materials*, vol. 13, no. 12, pp. 1135–1142, 2014.
- [62] M. Sharma, P. Jamdagni, A. Kumar, and P. Ahluwalia, “Electronic and dielectric properties of  $\text{mos}_2\text{-mox}_2$  heterostructures,” in *AIP Conference Proceedings*, vol. 1661, no. 1, 2015.
- [63] H.-P. Komsa and A. V. Krasheninnikov, “Electronic structures and optical properties of realistic transition metal dichalcogenide heterostructures from first principles,” *Physical Review B*, vol. 88, no. 8, p. 085318, 2013.
- [64] G. Kresse and J. Hafner, “Ab initio molecular dynamics for liquid metals,” *Physical Review B*, vol. 47, no. 1, p. 558, 1993.
- [65] J. P. Perdew, K. Burke, and M. Ernzerhof, “Generalized gradient approximation made simple,” *Physical review letters*, vol. 77, no. 18, p. 3865, 1996.
- [66] H. Terrones, F. López-Urías, and M. Terrones, “Novel hetero-layered materials with tunable direct band gaps by sandwiching different metal disulfides and diselenides,” *Scientific reports*, vol. 3, 2013.
- [67] N. Lu, H. Guo, L. Wang, X. Wu, and X. C. Zeng, “van der waals trilayers and superlattices: modification of electronic structures of  $\text{mos}_2$  by intercalation,” *Nanoscale*, vol. 6, no. 9, pp. 4566–4571, 2014.

- [68] A. Ebnonnasir, B. Narayanan, S. Kodambaka, and C. V. Ciobanu, "Tunable  $\text{mos}_2$  bandgap in  $\text{mos}_2$ -graphene heterostructures," *Applied Physics Letters*, vol. 105, no. 3, p. 031603, 2014.
- [69] Y. Shi, W. Zhou, A.-Y. Lu, W. Fang, Y.-H. Lee, A. L. Hsu, S. M. Kim, K. K. Kim, H. Y. Yang, L.-J. Li *et al.*, "van der waals epitaxy of  $\text{mos}_2$  layers using graphene as growth templates," *Nano letters*, vol. 12, no. 6, pp. 2784–2791, 2012.
- [70] M.-Y. Lin, C.-E. Chang, C.-H. Wang, C.-F. Su, C. Chen, S.-C. Lee, and S.-Y. Lin, "Toward epitaxially grown two-dimensional crystal hetero-structures: Single and double  $\text{mos}_2$ /graphene hetero-structures by chemical vapor depositions," *Applied Physics Letters*, vol. 105, no. 7, p. 073501, 2014.
- [71] M.-W. Lin, L. Liu, Q. Lan, X. Tan, K. S. Dhindsa, P. Zeng, V. M. Naik, M. M.-C. Cheng, and Z. Zhou, "Mobility enhancement and highly efficient gating of monolayer  $\text{mos}_2$  transistors with polymer electrolyte," *Journal of Physics D: Applied Physics*, vol. 45, no. 34, p. 345102, 2012.
- [72] H. Wang, L. Yu, Y.-H. Lee, W. Fang, A. Hsu, P. Herring, M. Chin, M. Dubey, L.-J. Li, J. Kong *et al.*, "Large-scale 2d electronics based on single-layer  $\text{mos}_2$  grown by chemical vapor deposition," *arXiv preprint arXiv:1302.4027*, 2013.
- [73] H. Wang, L. Yu, Y.-H. Lee, Y. Shi, A. Hsu, M. L. Chin, L.-J. Li, M. Dubey, J. Kong, and T. Palacios, "Integrated circuits based on bilayer  $\text{mos}_2$  transistors," *Nano letters*, vol. 12, no. 9, pp. 4674–4680, 2012.
- [74] H. Qiu, L. Pan, Z. Yao, J. Li, Y. Shi, and X. Wang, "Electrical characterization of back-gated bi-layer  $\text{mos}_2$  field-effect transistors and the effect of ambient on their performances," *Applied Physics Letters*, vol. 100, no. 12, p. 123104, 2012.
- [75] W. Bao, X. Cai, D. Kim, K. Sridhara, and M. S. Fuhrer, "High mobility ambipolar  $\text{mos}_2$  field-effect transistors: Substrate and dielectric effects," *Applied Physics Letters*, vol. 102, no. 4, p. 042104, 2013.
- [76] J. Kang, W. Liu, and K. Banerjee, "High-performance  $\text{mos}_2$  transistors with low-resistance molybdenum contacts," *Applied Physics Letters*, vol. 104, no. 9, p. 093106, 2014.
- [77] L. Yu, Y.-H. Lee, X. Ling, E. J. Santos, Y. C. Shin, Y. Lin, M. Dubey, E. Kaxiras, J. Kong, H. Wang *et al.*, "Graphene/ $\text{mos}_2$  hybrid technology for large-scale two-dimensional electronics," *Nano letters*, vol. 14, no. 6, pp. 3055–3063, 2014.

- [78] W. Zhang, C.-P. Chuu, J.-K. Huang, C.-H. Chen, M.-L. Tsai, Y.-H. Chang, C.-T. Liang, Y.-Z. Chen, Y.-L. Chueh, J.-H. He *et al.*, “Ultra-high-gain photodetectors based on atomically thin graphene-mos<sub>2</sub> heterostructures,” *Scientific reports*, vol. 4, 2014.
- [79] K. Roy, M. Padmanabhan, S. Goswami, T. P. Sai, G. Ramalingam, S. Raghavan, and A. Ghosh, “Graphene-mos<sub>2</sub> hybrid structures for multifunctional photoresponsive memory devices,” *Nature nanotechnology*, vol. 8, no. 11, pp. 826–830, 2013.
- [80] S. Larentis, B. Fallahazad, and E. Tutuc, “Field-effect transistors and intrinsic mobility in ultra-thin mos<sub>2</sub> layers,” *Applied Physics Letters*, vol. 101, no. 22, p. 223104, 2012.
- [81] M. W. Iqbal, M. Z. Iqbal, M. F. Khan, M. A. Shehzad, Y. Seo, J. H. Park, C. Hwang, and J. Eom, “High-mobility and air-stable single-layer ws<sub>2</sub> field-effect transistors sandwiched between chemical vapor deposition-grown hexagonal bn films,” *Scientific reports*, vol. 5, 2015.
- [82] W. Liu, W. Cao, J. Kang, and K. Banerjee, “(invited) high-performance field-effect-transistors on monolayer-ws<sub>2</sub>,” *ECS Transactions*, vol. 58, no. 7, pp. 281–285, 2013.
- [83] W. Liu, J. Kang, D. Sarkar, Y. Khatami, D. Jena, and K. Banerjee, “Role of metal contacts in designing high-performance monolayer n-type ws<sub>2</sub> field effect transistors,” *Nano letters*, vol. 13, no. 5, pp. 1983–1990, 2013.
- [84] J. Chang, L. F. Register, and S. K. Banerjee, “Ballistic performance comparison of monolayer transition metal dichalcogenide mx<sub>2</sub> (m= mo, w; x= s, se, te) metal-oxide-semiconductor field effect transistors,” *Journal of Applied Physics*, vol. 115, no. 8, p. 084506, 2014.
- [85] J. C. Cuevas. Introduction to density functional theory. [Online]. Available: [https://www.uam.es/personal\\_pdi/ciencias/jc Cuevas/Talks/JC-Cuevas-DFT.pdf](https://www.uam.es/personal_pdi/ciencias/jc Cuevas/Talks/JC-Cuevas-DFT.pdf)
- [86] P. Haynes, “Linear-scaling methods in ab initio quantum-mechanical calculations,” Ph.D. dissertation, University of Cambridge, 1998.
- [87] P. Hohenberg and W. Kohn, “Inhomogeneous electron gas,” *Physical review*, vol. 136, no. 3B, p. B864, 1964.
- [88] W. Kohn and L. J. Sham, “Self-consistent equations including exchange and correlation effects,” *Physical review*, vol. 140, no. 4A, p. A1133, 1965.

- [89] L. H. Thomas, "The calculation of atomic fields," in *Mathematical Proceedings of the Cambridge Philosophical Society*, vol. 23, no. 05. Cambridge Univ Press, 1927, pp. 542–548.
- [90] E. Fermi, "Un metodo statistico per la determinazione di alcune proprieta dell'atome," *Rend. Accad. Naz. Lincei*, vol. 6, no. 602-607, p. 32, 1927.
- [91] P. P. Rushton, "Towards a non-local density functiona description of exchange and correlation," Ph.D. dissertation, Durham University, 2002.
- [92] D. L. G. Cheung, "Structures and properties of liquid crystals and related molecules from computer simulation," Ph.D. dissertation, Durham University, 2002.
- [93] D. C. Langreth and M. Mehl, "Beyond the local-density approximation in calculations of ground-state electronic properties," *Physical Review B*, vol. 28, no. 4, p. 1809, 1983.
- [94] J. P. Perdew, J. Chevary, S. Vosko, K. A. Jackson, M. R. Pederson, D. Singh, and C. Fiolhais, "Atoms, molecules, solids, and surfaces: Applications of the generalized gradient approximation for exchange and correlation," *Physical Review B*, vol. 46, no. 11, p. 6671, 1992.
- [95] D. Hamann, M. Schlüter, and C. Chiang, "Norm-conserving pseudopotentials," *Physical Review Letters*, vol. 43, no. 20, p. 1494, 1979.
- [96] P. Giannozzi, S. Baroni, N. Bonini, M. Calandra, R. Car, C. Cavazzoni, D. Ceresoli, G. L. Chiarotti, M. Cococcioni, I. Dabo *et al.*, "Quantum espresso: a modular and open-source software project for quantum simulations of materials," *Journal of physics: Condensed matter*, vol. 21, no. 39, p. 395502, 2009.
- [97] C. Hartwigsen, S. Goedecker, and J. Hutter, "Relativistic separable dual-space gaussian pseudopotentials from h to rn," *Physical Review B*, vol. 58, no. 7, p. 3641, 1998.
- [98] H. J. Monkhorst and J. D. Pack, "Special points for brillouin-zone integrations," *Physical review B*, vol. 13, no. 12, p. 5188, 1976.
- [99] L. Zeng, Z. Xin, S. Chen, G. Du, J. Kang, and X. Liu, "Remote phonon and impurity screening effect of substrate and gate dielectric on electron dynamics in single layer mos2," *Applied Physics Letters*, vol. 103, no. 11, p. 113505, 2013.
- [100] O. Kurniawan, P. Bai, and E. Li, "Ballistic calculation of nonequilibrium green's function in nanoscale devices using finite element method," *Journal of Physics D: Applied Physics*, vol. 42, no. 10, p. 105109, 2009.

- [101] R. Venugopal, “Modeling quantum transport in nanoscale transistors,” Ph.D. dissertation, Purdue University, 2003.
- [102] Y. Liu and M. Lundstrom, “Simulation of iii-v hemts for high-speed low-power logic applications,” *ECS Transactions*, vol. 19, no. 5, pp. 331–342, 2009.
- [103] Y. Liu, *III-V nanoscale MOSFETS: Physics, modeling, and design*. PURDUE UNIVERSITY, 2010.
- [104] Z. Ren, R. Venugopal, S. Goasguen, S. Datta, and M. S. Lundstrom, “nanomos 2.5: A two-dimensional simulator for quantum transport in double-gate mosfets,” *IEEE Transactions on Electron Devices*, vol. 50, no. 9, pp. 1914–1925, 2003.
- [105] J. Wang, “Device physics and simulation of silicon nanowire transistors,” Ph.D. dissertation, Citeseer, 2005.
- [106] S. Datta, *Quantum transport: atom to transistor*. Cambridge University Press, 2005.
- [107] N. Ma and D. Jena, “Interband tunneling in two-dimensional crystal semiconductors,” *Applied Physics Letters*, vol. 102, no. 13, p. 132102, 2013.
- [108] B. Biel, L. Donetti, E. R. Ortiz, A. Godoy, and F. Gámiz, “Tunability of effective masses on mos<sub>2</sub> monolayers,” *Microelectronic Engineering*, vol. 147, pp. 302–305, 2015.
- [109] J. Kang and J. Li, “Ab initio study on mos<sub>2</sub> and its family: Chemical trend, band alignment, alloying, and gap modulation,” in *MoS<sub>2</sub>*. Springer, 2014, pp. 77–101.
- [110] H. Behera and G. Mukhopadhyay, “Strain-tunable band gap in graphene/h-bn hetero-bilayer,” *Journal of Physics and Chemistry of Solids*, vol. 73, no. 7, pp. 818–821, 2012.
- [111] W. Cao, J. Kang, D. Sarkar, W. Liu, and K. Banerjee, “2d semiconductor fets—projections and design for sub-10 nm vlsi,” *IEEE Transactions on Electron Devices*, vol. 62, no. 11, pp. 3459–3469, 2015.